Probing and controlling magnetism in 2D materials

John Cenker

A dissertation

submitted in partial fulfillment of the

requirements for the degree of

Doctor of Philosophy

University of Washington

2023

Reading Committee:

Xiaodong Xu, Chair

Jiun-Haw Chu

Ting Cao

Program Authorized to Offer Degree:

Department of Physics

University of Washington

Abstract

Probing and controlling magnetism in 2D materials

John Cenker

Chair of the Supervisory Committee:
Professor Xiaodong Xu
Department of Physics

A central goal of condensed matter physics is the discovery and design of materials systems with properties and behavior that have the potential to advance technology. The rapidly expanding field of two-dimensional materials provides unprecedented opportunities for rational materials design due to both the interesting physics that emerge in pristine nanoscale crystals, and the unprecedented tunability of these systems which enables on-demand control over the emergent phenomena. In this thesis, we will explore tunable coupling between spin, charge, and lattice in the layered magnetic semiconductor CrSBr. The first half of this thesis will establish that the excitonic optical response and electronic transport in CrSBr are strongly dependent on the magnetic state, a desired behavior of magnetic semiconductor systems which have been pursued for over two decades due to their promise for energy-efficient spintronic devices. The second half will explore techniques for applying large strains to 2D materials using a piezoelectric strain cell

at cryogenic temperatures. In addition to establishing new techniques for engineering interlayer strain transfer in 2D materials generally, we found that CrSBr has excellent mechanical properties which allow for the application of extreme strains. As strain is increased along the *a* axis, the interlayer magnetic exchange coupling is continuously tuned from a negative antiferromagnetic (AFM) value all the way to a positive ferromagnetic (FM) one, resulting in a reversible strain-induced magnetic phase transition. We then harnessed this AFM to FM phase transition to realize strain-controlled magnetic tunnel junction devices. The strain tuned magnetism enables many discoveries including novel magnon modes at intermediate strains, dynamic layer-wise magnetization flipping and control of multiple stable magnetic states, and the creation of stochastic domains with a strain-tunable sigmoidal response curve. These results combined with the developed strain techniques provide a plethora of opportunities for probing and controlling 2D magnetism and a wide range of other quantum phenomena in 2D materials and heterostructures.

TABLE OF CONTENTS

List of Figures iii

Chapter 1. Introduction 10

1.1 Dissertation Outline 13

Chapter 2. Optical Probes of Magnetism in 2D Materials 16

2.1 Magnetic properties of CrSBr 17

2.2 Optical properties of CrSBr 19

2.3 Magneto-electronic coupling in CrSBr 22

2.4 Coherent Exciton Magnon Coupling in CrSBr 26

2.5 Raman spectroscopy: another optical probe of high-energy magnons in 2D magnets. 33

Chapter 3. Transport Probes of Magnetism in CrSBr 41

3.1 Magneto-transport measurements of trilayer CrSBr 42

3.2 The magnetic tunnel junction: a fundamental spintronic device 47

Chapter 4. Strain Tuning of 2D Materials 53

4.1 Strain tuning of 2D materials: Experimental Techniques 53

4.2 Calibration of strain in 2D materials and heterostructures 55

4.3 Unity Strain Transmission in CrSBr 57

4.4 Probing strain transmission in hexagonal 2D materials 59

4.5 Bi_2SeO_5: An ideal straintronic dielectric 62

4.6 Future directions 65

Chapter 5. Strain Tuned Magnetism in CrSBr 68

5.1 Strain dependent magneto-photoluminescence of CrSBr 69

5.2 Theoretical understanding of the strain-induced magnetic phase transition 73

5.3 Strain engineering of magnon dispersion and discovery of novel magnon states 76

Chapter 6. Strain-programmable Magnetic Tunnel Junctions 79

6.1 Straintronic CrSBr MTJs 80

6.2 Probing domain formation during the strain-induced AFM to FM transition 83

6.3 Understanding Field and Strain induced Magnetic Phase Transitions 86

6.4 Creation of metastable states 91

6.5 Future directions 96

Appendix I 101

Appendix II 106

Appendix III 109

Bibliography 111

LIST OF FIGURES

Figure 1.1-1 | Isolation and tuning of atomically thin materials. 10
Figure 2.1-1| Magnetic structure of atomically thin CrSBr. 17
Figure 2.1-2 | Crystal structure and exchange interactions. 18
Figure 2.1-3| Exchange interaction pathways in bilayer CrSBr....19
Figure 2.2-1 | Band structure and excitons in semiconductors. 19
Figure 2.2-2 | Excitons in atomically thin CrSBr....21
Figure 2.3-1 | Magneto-exciton coupling in atomically thin CrSBr 23
Figure 2.3-2 | Calculated band structure in AFM and FM bilayer CrSBr....24
Figure 2.3-3 | Real space calculated wave function for the lowest-energy exciton in bilayer CrSBr 25
Figure 2.4-1 | Magnons: quasiparticle excitations of the magnetic order. 26
Figure 2.4-2 | Magnon-exciton coupling in CrSBr 28
Figure 2.4-3 | Pump-probe signatures of magnon modes. 29
Figure 2.4-4 | Magnon hybridization under tilted magnetic field.. 30
Figure 2.4-5 | Tuning exciton-hybridized magnon coupling via symmetry-breaking magnetic field 31
Figure 2.4-6 | Extracted hybridized magnon-magnon interactions. 32
Figure 2.5-1 | Low-energy cross-circularly polarized Raman scattering in monolayer CrI_3 with magnetic fields of 0 T, -4 T, and +4 T applied, respectively. 34
Figure 2.5-2 | Magneto-Raman measurements of monolayer CrI_3 35
Figure 2.5-3 | Selection rules for the one-magnon Raman scattering in monolayer CrI_3 36
Figure 2.5-4 | Probing magnetism and spin-flip transitions in bilayer CrI_3 *via* magnons. 37
Figure 2.5-5| Optical magnons in bilayer CrI_3. 39
Figure 3.1-1| Design and optical image of a dual-gated CrSBr device....42
Figure 3.1-2| Low temperature transport of a dual-gated 3L CrSBr device. 43
Figure 3.1-3| Negative magnetoresistance in CrSBr devices. 44
Figure 3.1-4 | Angle-dependent magnetoresistance in atomically thin CrSBr....45
Figure 3.1-5| Gate tuned magnetoresistance in trilayer CrSBr.. 46

Figure 3.2-1 | Diagram of basic spin filter devices. 48
Figure 3.2-2 | Schematic of MTJ devices 49
Figure 3.2-3 | Bilayer CrSBr magnetic tunnel junction.. 50
Figure 3.2-4 | Angular magnetic field dependence of tunneling magnetoresistance in bilayer CrSBr. 51
Figure 4.1-1 | Strain cell and techniques.. 54
Figure 4.2-1 | Calibrating strain using Raman spectroscopy. 56
Figure 4.3-1 | Unity Strain transmission in CrSBr 58
Figure 4.4-1 | Sensing strain transmission through CrSBr and hBN. 59
Figure 4.4-2 | Crystal structures of bilayer hBN and CrSBr. 60
Figure 4.4-3 | Probing strain transmission in other orthorhombic crystals. 61
Figure 4.5-1 | Strain device fabrication using Bi_2SeO_5 dielectric substrates**.** 63
Figure 4.5-2 | Gate dependent WS_2 photoluminescence spectra 63
Figure 4.5-3 | Strain and gate tuning of monolayer WS_2 65
Figure 4.6-1 | New types of strain devices 66
Figure 5.1-1 | Properties of the unstrained thin bulk CrSBr 69
Figure 5.1-2 | Strain dependent photoluminescence measurements of a suspended thin bulk CrSBr sample 70
Figure 5.1-3 | Strain dependent magneto-PL measurements of thin bulk CrSBr 72
Figure 5.1-4 | Magneto-PL measurements along the *a* axis in the unstrained AFM and high-strain FM states. 73
Figure 5.2-1 | DFT scalar-relativistic calculations of strain effects on interlayer magnetic ordering. 74
Figure 5.2-2 | Understanding interlayer magnetic coupling in CrSBr 75
Figure 5.3-1 |Strain tuning of magnon dispersion in CrSBr 77
Figure 5.3-2 | Extracted interlayer exchange (**a**) and anisotropy difference **(b**) as a function of strain. 78
Figure 6.1-1 | Schematic and optical image of a straintronic magnetic tunnel junction 80
Figure 6.1-2 | Strain dependent tunneling magnetoresistance 81
Figure 6.1-3 | Zero field strain switching of the CrSBr MTJ 83

Figure 6.2-1 | Mapping magnetic domain formation in the CrSBr MTJ. 84
Figure 6.2-2 | Strain-dependent lateral magnetotransport in thin bulk CrSBr. 85
Figure 6.3-1 | Illustration of magnetic field induced AFM to FM transition. 86
Figure 6.3-2 | Illustration of strain-induced AFM to FM transition.....88
Figure 6.3-3 | Thickness dependence of the strain-induced magnetic phase transition probed by electron tunneling.....89
Figure 6.3-4 | Strain pulse control of multiple magnetoresistive states.. 90
Figure 6.4-1 | Types of computing bits. 91
Figure 6.4-2 | Creating and controlling metastable states 93
Figure 6.4-3 | Sampling time dependence of NIST test suite 95
Figure 6.4-4 | Dwell time histograms for the zero state and one state 95
Figure 6.4-5 | Lifetimes of the zero and one state. 96
Figure 6.5-1 | CrSBr MTJ array using the crossbar geometry 97
Figure 6.5-2 | Six layer strain-actuated magnetic tunnel junction. 98
Figure 6.5-3 | Bias polarity dependent switching and asymmetric vertical magnetic domain structure.....99
Figure AI.1 | Reflective magnetic circular dichroism measurements.....102
Figure AI.2 | Diagram of magnons in canted AFM state, when the field is applied directly along the *a* axis 103
Figure AI.3 | Raman scattering from acoustic magnons in unexfoliated bulk single crystal CrI_3 105
Figure AII.1 | Temperature dependence of operational piezo voltage range 106
Figure AII.2 | Fabrication procedure for suspended strain samples.....108
Figure AIII.1 | Complicated domain behavior during the strain-induced magnetic phase transition 109
Figure AIII.2 | Strain pulse measurements in the purely FM and AFM states.....110

ACKNOWLEDGEMENTS

The first person I want to acknowledge is Prof. Xiaodong Xu, who was an excellent advisor during my entire PhD. I had never taken an optics course, touched laboratory optics, or heard of 2D materials before joining the Xu group. Consequently, I was basically oblivious to the fact that Xiaodong had been pioneering some of the most exciting and cutting-edge fields in all condensed matter physics when he first contacted me. However, I quickly decided to join the group simply because of his contagious enthusiasm and kind personality. This turned out to be unquestionably one of the best decisions of my life. The unbelievable productivity, creativity, and support Xiaodong has shown and developed within the group is remarkable. I truly believe that the Xu group is the best place to pursue a physics PhD in the entire world.

In addition to Xiaodong, I would like to thank the other members of my committee for their support and advice: Ting Cao, Jiun-Haw Chu, David Cobden, Alejandro Garcia, Xiaosong Li, and Di Xiao. Special thanks to Ting, Jiun-Haw, and Xiaodong for serving on the reading committee. In addition to serving on these committees, the theoretical insight gained by collaboration with Ting and Di were invaluable in many projects, and the experimental input from Dave and Jiun-Haw helped polish and strengthen our understanding. In fact, it was meeting and talking with Jiun-Haw during the visiting weekend that first sparked my interest in strain experiments.

During my PhD, I made many dear friends and colleagues. The first mentor was Bevin, another person notable for both incredible scientific achievement and amazing personality. You were a fantastic mentor, and I hope I maintained your standard. The epic late-night drives to Beth's will always be some of the highlights of my PhD. The next mentor was Nathan and then Geoff, both of whom greatly helped polish my optics and physics knowledge, especially regarding

excitons and semiconductors. Afterward, I had the pleasure to work with Dmitry and absorb some of his transport expertise. Dmitry, your optimism and positivity has personally been a bright light throughout my PhD, and working with you was an amazing experience. I thank all these mentors for their patience with me, and hope we stay in contact wherever our lives take us. In addition, there are a plethora of people who were vital to my growth including: Kyle S., Colin, Qi, Ding, Pasqual, Zaiyao, Yingqi, Tiancheng, Minhao, Xi, Zhong, Yuzhou, Chaowei (Chu/Xu labs), Jiayi, Jiaqi, Eric, Yinong, Xuetao Ma (Yankowitz/Chu), Zhaoyu Liu (Chu), Josh Mutch (Chu) etc...

As I became an older student, I was given the opportunity to mentor several people. I was lucky that all of them turned out to be highly motivated, intelligent, and a joy to work with. The first two undergraduates were Aaron and Pearl, both of whom have already graduated and moved onto great things. Then, I worked with Harvey and Catherine who made large contributions to the strained magnetic tunnel junction project, a project that Eric Z. also joined over the last summer. I can only hope I was not too easy on Harvey. Last, but not least, it was a pleasure working with the disciplined Kyle J. over the past several months. Working with all of you was extremely motivating and refreshing, and I hope I provided a positive and interesting research experience.

In addition to undergraduate and high school students, working with the younger graduate students in the Xu group was among the greatest parts of my PhD. I could not have chosen a better partner to work on some strain projects over the last few years with than Jordan. It has no doubt been challenging at times, but I admire your dedication, and really hope you can have a great payoff in the end. Joon, you have become not only one of the best device makers in the world (in my opinion), but also an excellent physicist. Will, your knowledge and insight into optics and physics continually impressed me during our discussions. I hope that someday you perfect your

automated focusing procedure during temperature dependent measurements. Jack and Courtney, we did not collaborate on as many projects as I hoped (I guess there's only so much time in a PhD), but you both have very bright futures. Ren, it is sad that I have to leave right as we were starting to work together more. However, you're in great hands with Geoff, Jordan and everybody else. Last but certainly not least is Mai. The late nights making samples which often (but not always) culminated in the tragic death of "babies" were somehow rejuvenating. Perhaps it's due to the Taylor Swift you played (probably not), or the naïve hope that maybe things will work *this time*. The fact that I was able to convince someone as smart as you to follow my silly advice gives me hope. My future would augur very well if I could convince someone half as smart and motivated as you, or anyone on this list, to work with me in the chance I become a professor (knock on wood).

Outside of UW, the collaboration with Columbia University has proven to be extremely fruitful. The amazing CrSBr crystals grown first by Avalon Dismukes and then Daniel Chica in the group of Prof. Xavier Roy enabled a large majority of this thesis. In addition, conversations and collaborations with Kihong Lee and Youn Jue Bae in Prof. Xiaoyang Zhu's group were productive and useful. I hope to continue these collaborations once I start my post-doc work at Columbia! Additional crystals came from Michael McGuide (CrI_3) and Takashi Taniguchi and Kenji Watanabe (hBN) were vital to several completed projects as well.

I finally want to thank my friends and family. Jenny, thank you for the support over several great years. Terrel, your friendship and care were greatly appreciated. Wan Jin, Kyle H., Dean, and Teresa, you all made first year bearable and passable. The greatest light during some dark days was the promise of visiting home in Ohio, relaxing, and hanging out with old friends and family. Especially my sister and mom. Our family is full of character, but I love it and you.

DEDICATION

To my adorable cat, and my dad. I hope that eternity has free access to academic journals.

Chapter 1. INTRODUCTION

A central goal of condensed matter physics is the creation, control, and eventual use of quantum phenomena such as superconductivity and magnetism. These phenomena have already revolutionized daily human life, enabling technologies as small as computer hard drives and as large as Maglev trains. Still, because such quantum behaviors emerge in systems with interactions between $\sim 10^{21}$ particles, the underlying mechanisms can be challenging to understand theoretically. Moreover, the types of systems which can be physically realized are subject to nature's preferences for, e.g., symmetry and chemistry. Material platforms which offer a high degree of tunability can provide fertile ground for new discoveries with implications for both fundamental physics and technology.

One approach which has proven fruitful in recent years is to reduce the dimensionality of a bulk crystal to the atomically thin limit[1-3]. Created by the remarkably simple but elegant method of pulling apart layered van der Waals (vdW) materials with Scotch tape (Fig. 1.1-1a-b), these 2D crystals not only host exotic properties endowed from their low dimensionality and finite thickness

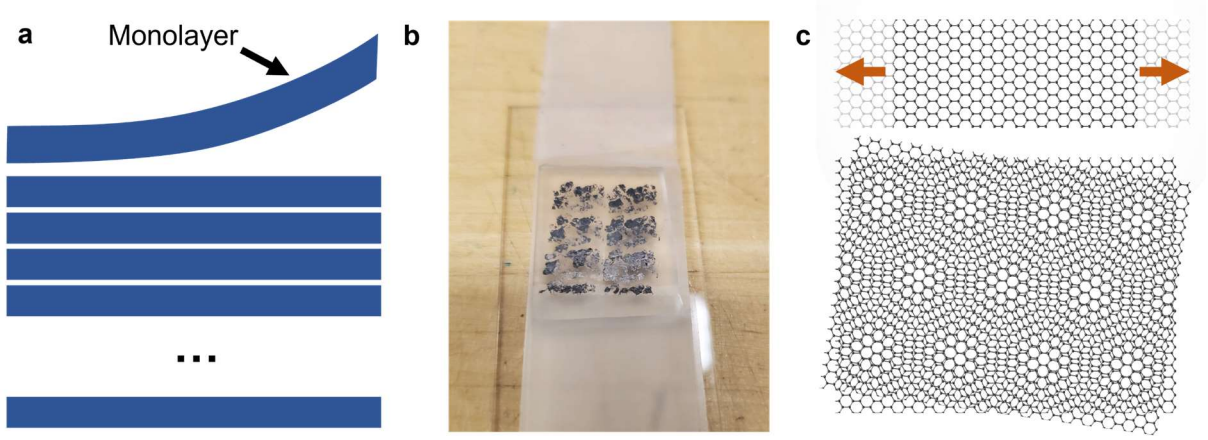

Figure 1.1-1 | Isolation and tuning of atomically thin materials. **a,** Illustration of the exfoliation process. A single, or few layer crystal is exfoliated from an effectively infinitely layered one. **b,** Optical image of Scotch tape pressed down on a substrate before exfoliation. **c,** Common tuning methods for 2D materials include stretching (top) and twisting to form moiré patterns (bottom).

but are also tunable through a variety of control knobs. The most prominent control methods include mechanical means such as tensile strain[4-6] (Fig. 1.1-1c, top) and hydrostatic pressure[7-9], electrostatic gating[1,10-12] which allows deterministic injection and removal of charge, and heterostructure engineering including proximity effects[13-15] and twisting[16-20] (Fig. 1.1-1c, bottom). Such a wide variety of techniques presents an immense phase space to search for new physics. Explorations over nearly two decades have indeed revealed an incredible number of exciting phenomena, with apparently endless possibilities still ahead. It seems we have only touched the tip of the iceberg so far.

The 2D nature of these crystals, however, can be a double-edged sword. For instance, the reduced sample volume renders certain experiments (e.g., neutron scattering) impossible, and many interesting materials, including the relatively recently discovered 2D magnets, are extremely air sensitive in the atomically thin limit. Luckily, by the time that I joined Prof. Xu's group in 2018 to study these emerging 2D magnets, significant progress had been made in addressing these issues: polar reflective magnetic circular dichroism (RMCD) and the magneto-optical Kerr effect (MOKE) were identified as effective probes of out-of-plane magnetization[21-23], and encapsulation with other atomically flat 2D materials allowed for the study of even the most air sensitive materials[23-25]. These advances enabled the field of 2D magnetism, pioneered in large part by the Xu group, to blossom[13,26-28]. Magnetic materials have been an essential part of humanity's technological development, and 2D magnets have opened the door for further exploration and exploitation of magnetism down to the atomic limit in highly tunable materials systems.

One such tuning method which should be particularly powerful for 2D materials is strain. In principle, 2D materials are exceptional material platforms for strain engineering, a proven tuning knob for quantum phenomena including topology[29,30], superconductivity[31,32], and

magnetism[33,34] in bulk crystals. Reducing the dimensionality of the system from an (effectively) infinite to a finite number of layers dramatically reduces the total number of defects, which serve as rare failure points[35], despite both crystals having the same defect density. Indeed, monolayer crystals were shown to be the strongest materials ever measured[36,37] shortly after their discovery.

There are distinct challenges facing the full exploitation of these remarkable mechanical materials, however, as the weak strain transmission between layers makes the application of large strain to many crystals, and especially vdW heterostructures, impossible. In fact, the in-situ strain tunability of high-quality vdW devices[38] at the cryogenic temperatures needed for quantum phenomena to emerge has remained below 0.5 %, which is less than even bulk crystals[29,31]. The early attempts to promote strain transmission in van der Waals heterostructures and devices focused on using evaporated metals to clamp the flakes to the substrate[38-40]. While such techniques may increase the adhesion to the substrate, they do not address the root causes of the poor strain tunability in vdW heterostructures: weak interlayer strain transmission[41,42] and a tendency towards soliton formation[43,44]. Furthermore, it is unclear how well such clamping techniques could work with air-sensitive materials and moiré heterostructures (Fig. 1.1-1c, bottom) which require complete, all-2D encapsulation with pristine, atomically smooth surfaces.

Fortunately, the evolving field of vdW materials continually offers new crystals with unique, often surprising properties and phenomena which open new possibilities at the nanoscale. For instance, many works have found that the coupling of the magnetic order with other excitations, such as phonons[45,46] and excitons[47,48], can enable sensitive probing of 2D magnets. And recently, materials with crystal structures different from the hexagonal or honeycomb lattices ubiquitous in the 2D field have received increased interest. These materials may have completely different mechanical properties than the widely studied graphite and hexagonal boron nitride

(hBN), and thus present new opportunities for strain engineering. Studying the behavior of new atomically thin crystals and inventing creative ways to use their distinct and sometimes bizarre properties has played a central role in the ever-evolving field of 2D materials.

A material which exhibits both interesting physical phenomena and mechanical properties is the layered magnetic semiconductor CrSBr, which began to be investigated shortly after I joined the Xu group. The coupling of charge and spin in magnetic semiconductors provides powerful probes of the in-plane magnetic order in addition to being desirable for potential spintronics device applications. Structurally, the buckled, anisotropic orthorhombic structure with hook-like Br atoms could promote strong strain transmission between layers. These properties indicate that CrSBr could be an ideal platform for probing and controlling 2D magnetism. More generally, studying the mechanical behavior of CrSBr and other emerging materials can identify new building blocks of vdW heterostructures which can enable their remarkable potential for mechanical tunability and control over a wide range of nanoscale quantum phenomena.

1.1 Dissertation Outline

In this thesis we will explore the coupling of spin, charge, and lattice in the layered magnetic semiconductor CrSBr. To achieve this, we will need to establish effective probes of the magnetic and electronic properties of CrSBr and develop methods for generating extreme strains in nanoscale materials at cryogenic temperatures.

In Chapter Two we will establish the optical probes of antiferromagnetism in 2D materials. Historically, probing magnetism in AFM materials has been challenging due to the net zero magnetic moment. This is especially true for in-plane magnetic ordering which cannot be probed by more conventional techniques, i.e., magneto-optical Kerr effect, in the 2D limit. In CrSBr, however, the strong coupling between excitons and the magnetic order serves as a powerful probe

of the material's magnetic properties and dynamics. Specifically, photoluminescence (PL) and pump-probe reflectivity measurements enable the readout of the magnetic state and magnon dispersion.

The coupling of spin and charge established in Chapter Two has important consequences on the transport properties of CrSBr as well. In Chapter Three, we will explore magneto-transport in conventional CrSBr Hall bar devices in addition to all-vdW magnetic tunnel junctions (MTJ). In contrast to most previous AFMs, CrSBr devices are far less insulating and can be turned on at low temperatures with gate-tunable magnetoresistance. Still, the material is insulating enough to serve as an effective tunnel barrier in MTJs, with large tunneling magnetoresistance ratios consistent with other vdW MTJs.

After establishing the probes of CrSBr, we develop the methods for applying strain to atomically thin crystals, and the strain transmission characteristics of these materials in Chapter Four. First, the strain shift rate of CrSBr Raman modes is calibrated, and then used as a sensor of strain transfer in a variety of different layered crystals. Importantly, we find that strain transmits perfectly through the orthorhombic crystal CrSBr, in stark contrast to many of the most commonly used 2D materials which have hexagonal lattices and primarily in-plane bonds. In addition, efficient strain transfer occurs in other orthorhombic crystals α-MoO_3, and Bi_2SeO_5 which can serve as building blocks of new straintronic devices. We then use the different frictional properties of 2D crystals to deterministically engineer strain gradients.

In Chapter Five, we will report strain tuned magnetism in CrSBr. With increasing tensile strain, the interlayer magnetic exchange coupling is continuously tuned from antiferromagnetic at low strain to ferromagnetic at high strain due to the changing bond geometry. We comprehensively study the strain-dependent magnetic order using photoluminescence spectroscopy and pump-probe

reflectance to probe the magnetic state and magnon dispersions, respectively. Interestingly, a dispersionless magnon state occurs at certain values of interlayer exchange which is continuously tuned by strain.

In Chapter Six, we will further study the strain-induced magnetic phase transition using CrSBr as the tunnel barrier in strained MTJs. Concurrent vertical electron tunneling, and spatial-dependent PL measurements demonstrate that vertical mixed magnetic states form during the strain-induced AFM to FM phase transition. We harness the strain-control of the layer-dependent magnetism to realize straintronic MTJs which can be switched at zero magnetic field and demonstrate unprecedented multifunctionality in comparison to standard vdW MTJs, including the control of multiple stable and stochastic magnetoresistive states.

Chapter 2. OPTICAL PROBES OF MAGNETISM IN 2D MATERIALS

A long-standing quest in the field of spintronics has been the discovery and implementation of magnetic semiconductors[49-52]. The coupling of charge, used in computer processors, and spin, the basis of magnetic memory, in these materials could enable new computing technologies. Progress towards this end first came when it was realized that nonmagnetic III-V semiconductors doped with manganese exhibited ferromagnetic ordering[52]. These compounds, known as dilute magnetic semiconductors, became the subject of intense research for spintronics applications such as spin transistors[53], and spin-polarized light-emitting diodes[54,55]. However, the synthesis of true, intrinsic gate-tunable ferromagnetism turned out to be rather challenging[56].

The emerging field of 2D materials presents new opportunities to realize tunable, nanoscale magnetic semiconductors. Promisingly, two of the most intensely studied classes of 2D materials are magnets[13,27] and semiconductors[57-59]. However, many of the earliest studied vdW magnets were either highly insulating (e.g., CrI_3) or metallic (e.g., Fe_3GeTe_2). An important advance came with the synthesis and renewed study of the layered antiferromagnetic CrSBr in 2020[60,61]. The layered magnetic order in CrSBr generates large, gate-tunable magnetoresistance down to the atomically thin limit[62]. Moreover, this chapter establishes that the excitons, quasiparticle excitations consisting of a bound electron-hole pair, in CrSBr are highly sensitive to the magnetic order. This sensitivity makes PL a powerful probe of the magnetic order in addition to enabling measurement of the spin dynamics through ultrafast pump-probe experiments. Finally, at the end of the chapter we demonstrate that Raman spectroscopy can provide an additional probe of magnetic excitations in 2D magnets, given that the energy of the acoustic magnon is sufficiently large. This is the case for the prototypical 2D magnetic insulator CrI_3, but not for CrSBr.

The section detailing the PL behavior of atomically thin CrSBr was reported in *N. Wilson, K. Lee, J. Cenker, K. Xie*, *et al.* "Interlayer Electronic Coupling on Demand", published[63] in *Nature Materials*, while the ultrafast probing of magnons was established in *G. M. Diederich, J. Cenker, Y. Ren, et al.* "Tunable interaction between excitons and hybridized magnons in a layered semiconductor" which was published[48] in *Nature Nanotechnology*. The final subsection presents results using Raman spectroscopy to detect magnons in mono- and bilayer CrI_3 reported in *J. Cenker, B. Huang, et al.* "Direct observation of two-dimensional magnons in atomically thin CrI_3, published[64] in *Nature Physics*.

2.1 Magnetic properties of CrSBr

Atomically thin CrSBr crystals can be isolated using the Scotch tape method described in Chapter 1, yielding large, anisotropic flakes (Fig. 2.1-1a). When monolayer CrSBr is cooled, in-plane ferromagnetic ordering occurs below a Curie temperature[61] of $T_C \sim 146$ K, which is quite high in comparison to other monolayer 2D magnets[13]. The magnetic easy, intermediate, and hard axes lie along the crystallographic *b, a,* and *c* crystal axes, respectively (Fig. 2.1-1b). When cooled below $T_N \sim 132$ K, multilayer CrSBr adopts an A-type antiferromagnetic order[65] with

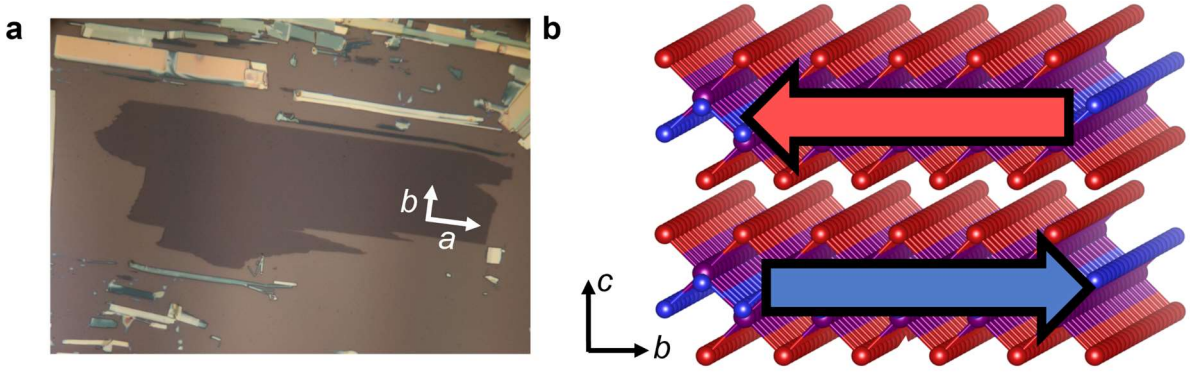

Figure 2.1-1| Magnetic structure of atomically thin CrSBr. **a,** Optical microscope image of a large (> 100 μm) trilayer CrSBr. The anisotropic structure enables easy identification of the crystal axes. **b,** A-type antiferromagnetic ordering, with alternating magnetization along the stacking direction (*c* axis). The spins are oriented along the *b* axis (short crystal axis in **a**) and are denoted by the red and blue arrows.

ferromagnetic intralayer and antiferromagnetic interlayer ordering resulting in a magnetic structure where alternating layers have opposite magnetization (Fig. 2.1-1b). This layered A-type AFM order is common to many other[23,66-68] 2D magnets which have strong anisotropy and weak interlayer exchange.

Theoretically, the ferromagnetic order of monolayer CrSBr can be understood by calculating the sign and value of the different superexchange pathways[69,70]. Figure 2.1-2a shows the crystal structure and three major magnetic exchange couplings J1, J2, J3. The sign of interlayer exchange interactions can be found using the Goodenough-Kanamori-Anderson rules[71-73] where a bond angle of 180° favors AFM order while a 90° angle favors FM order. The bond angle for J_1, which is the Cr-S-Cr superexchange along the *ab* diagonal direction in the SS-edge-sharing CrS_4Br_2 octahedra (Figure 2.1-2b), is close to 90° and therefore has an FM contribution. The same is also true for J_2 which corresponds to the nearly 90° Cr-S(Br)-Cr superexchange along the *a* axis for the SBr-edge sharing octahedra. On the other hand, the angle for J_3 is 160° yielding a competition of FM and AFM terms. The first principles calculation gives values of $J_1 = 4.11$ meV,

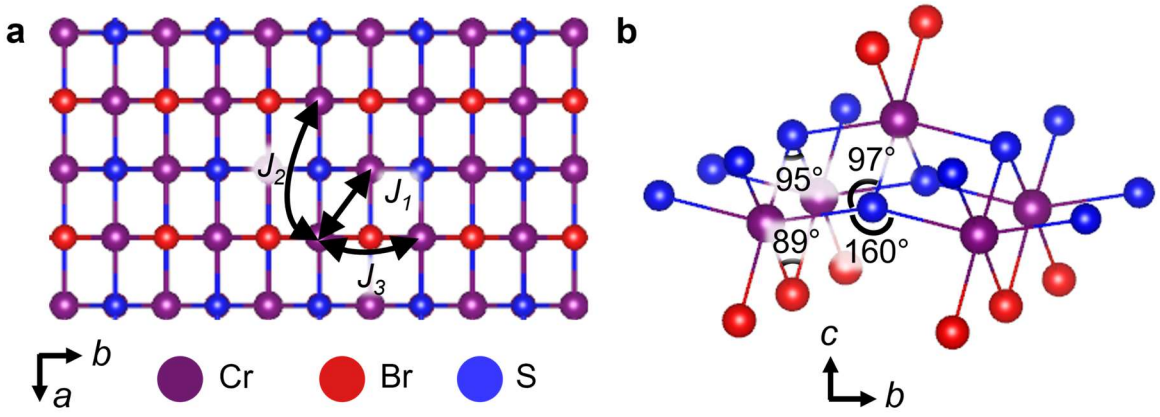

Figure 2.1-2 | Crystal structure and exchange interactions. **a,** The first three next-nearest exchange pathways *(J_{1-3})* between Cr atoms (purple spheres) in monolayer CrSBr. **b,** Distorted CrS_4Br_2 octahedra with relevant angles that are used to calculate the sign and strength of the exchange interactions.

J_2 = 3.22 meV, and J_3 = 2.78 meV, with all three prominent superexchange pathways favoring FM intralayer coupling[69].

In contrast to the intralayer exchange in monolayer CrSBr which has only strong FM interactions, calculations of the interlayer coupling is more complicated. Figure 2.1-3 shows the magnetic exchange coupling J1, J2, J3 and J4 for the 1st, 2nd, 3rd, and 4th nearest-neighbor (NN) interlayer Cr pairs. Similar to the intralayer case, the next-nearest neighbor superexchange J_1 gives a FM interaction. However, adding up all of the exchange contributions for $J_{1\text{-}4}$ obtained by first principles calculations yields a weak total AFM interlayer exchange[74]. Here, we notice the first indications that strain could be a powerful tuning knob in this system since the interlayer AFM order is fragile and originates from the bond geometry. This point will be elucidated further in Chapter 4.

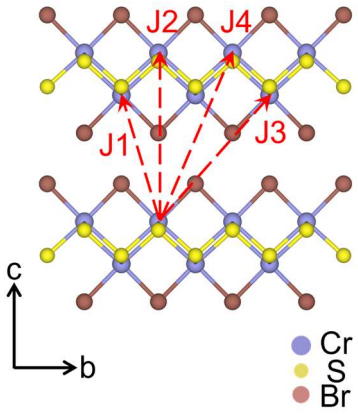

Figure 2.1-3 | Exchange interaction pathways in bilayer CrSBr, up to fourth next-nearest neighbor (J_1-J_4). Adapted from Ref. [74]

2.2 Optical properties of CrSBr

When electrons are excited from the valence band to conduction band in semiconductors, they leave behind a positively charged hole in the valence band. The Coulomb interaction between the negatively charged electron and positively charged hole can create a hydrogen-like bound quasiparticle state known as the exciton (Fig. 2.2-1). If the momentum mismatch between electron and hole is small enough, the electron can recombine with the hole and emit a photon, or

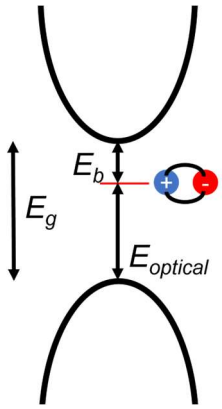

Figure 2.2-1 | Band structure and excitons in semiconductors.

photoluminescence (PL), equal to the exciton energy[75]. To first order, the exciton energy (or optical gap) is equal to the quasiparticle gap (E_g) minus the exciton binding energy (E_b).

The reduced dielectric screening and quantum confinement effects in atomically thin crystals result in an extremely large exciton binding energy, making them an excellent platform for studying exciton physics[59,76]. Moreover, the enhanced signal-to-noise ratio and sensitivity to the dielectric environment make excitons a powerful probe of various physics in 2D semiconductors. Spectacular examples can be found in moiré heterostructures formed by twisted monolayer transition metal dichalcogenides (TMDCs), where neutral and charged excitons have been used to probe correlated insulating states[19,77,78], magnetic ordering[79-81], and recently integer and fractional quantum anomalous Hall states[82,83].

Not all excitons are created equal, however. While the excitons in TMDCs are known to be Wannier-type[76,84,85] with a large Bohr radius, the excitons in many 2D magnets such as the highly insulating CrI_3 are Frenkel-type[86] which are far more localized. Consequently, they are much less sensitive to the environment and certain phenomena such as moiré effects which occur over several unit cells. CrSBr represents the first true 2D magnetic semiconductor, with strong Wannier-type excitonic resonances, as revealed by scanning tunneling microscopy (STM) and PL measurements of bulk CrSBr[60]. The STM measurement reveals a direct band gap of ~ 1.5 eV, albeit with many defect states near the conduction band edge, while the PL measurements give an optical band gap of ~ 1.25 eV at room temperature. Therefore, the binding energy of excitons in bulk CrSBr is ~ 0.25 eV, while advanced Green's function-Bethe-Salpeter equation (GW-BSE) calculations indicate an increased exciton binding energy of ~ 0.5 eV for the monolayer[63].

The calculated band structure of monolayer CrSBr indicates a direct band gap at the Γ point of the Brillouin zone (Fig. 2.2-2a). To experimentally confirm whether the direct-gap semiconducting behavior persists down to the 2D limit, we performed optical spectroscopy on atomically thin CrSBr flakes. Linear polarization-resolved differential reflectance (ΔR/R) and PL measurements of bilayer CrSBr are shown as the red and blue curves in Figure 2.2-2b, respectively. The excellent agreement of the exciton energies obtained from PL and ΔR/R indicates a direct band gap transition. The other observation which immediately stands out is the strong optical anisotropy: exciton is only visible in both ΔR/R and PL spectra when the incident light is polarized along the *b* axis, with no detectable exciton peak when excited along the *a* axis. The unity linear polarization is observed for all thicknesses of CrSBr flakes, regardless of magnetic order. Instead, it originates from symmetry considerations, which constrain the allowed polarization of optical transitions[63].

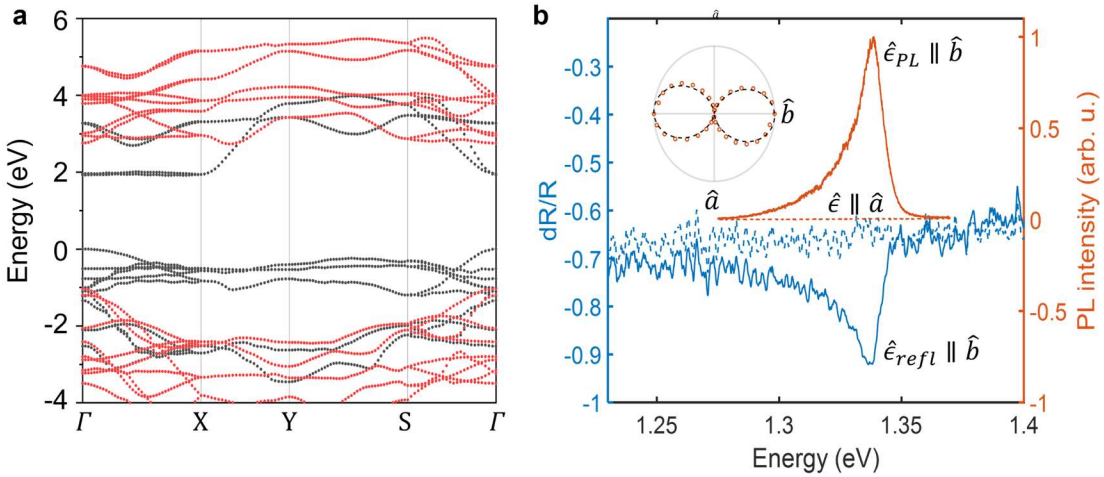

Figure 2.2-2 | Excitons in atomically thin CrSBr. **a,** Calculated spin-resolved band structure of monolayer CrSBr. The majority and minority spins are in black and red, respectively. **b,** Polarization resolved differential reflectance (blue) and PL spectra (orange) of the lowest energy exciton feature. The solid (dashed) lines represent polarization along the *b* (*a*) axis. Reproduced from Ref. [63]

2.3 MAGNETO-ELECTRONIC COUPLING IN CRSBR

The robust semiconducting and excitonic behavior in CrSBr could enable new magneto-electronic coupling effects which are absent in the more insulating 2D magnets. Figure 2.3-1a shows the color map of normalized PL intensity as a function of magnetic field applied along the easy *b* axis for monolayer CrSBr. No detectable energy shift is observed as the spins are aligned by the external field. However, a completely different behavior is observed for bilayer CrSBr, where a sharp redshift in PL energy is observed when the field exceeds ~ 0.15 T along the *b* axis (Fig. 2.3-1b). When the field is applied along the intermediate *a* and hard *c* axes (Fig. 2.3-1c-d), gradual redshifts are observed until saturating fields of ~ 0.9 and ~ 1.6 T, respectively, beyond which the PL is invariant to further increase in magnetic field. Extracting the PL energy reveals a quadratic energy shift with field when it is applied along the *a* and hard *c* axes (Fig. 2.3-1f). To confirm that the complete absence of magneto-excitonic coupling in monolayer CrSBr does not originate from a loss of magnetic ordering in the 2D limit, we performed polar reflective magnetic circular dichroism (RMCD) measurements. RMCD is an essential tool in the 2D magnet toolbox, and is sensitive to the out-of-plane magnetic moment (see Appendix AI.1). The gradual increase in RMCD of both mono- and bilayer CrSBr shown in Figure 2.3-1e confirm reveal a similar spin canting behavior, despite the lack of magneto-excitonic coupling in the monolayer.

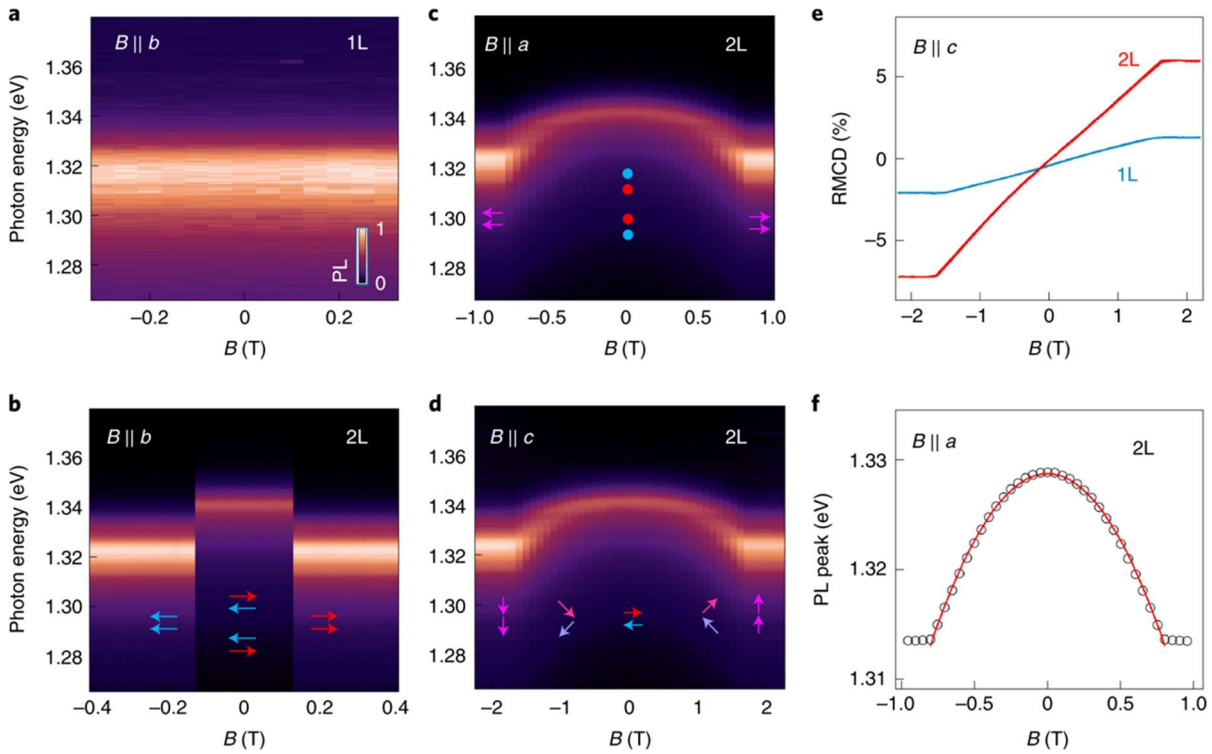

Figure 2.3-1 | Magneto-exciton coupling in atomically thin CrSBr. **a,** Magnetic field dependent photoluminescence measurements of monolayer CrSBr with the field applied along the *b* (easy) axis. **b-d,** Magneto-PL measurements of bilayer CrSBr with the field applied along the *b* (easy), *a* (intermediate), and *c* (hard) axes, respectively. The possible spin alignments of the different magnetic configurations are depicted by the inset arrows. **e**, RMCD measurements of monolayer (blue) and bilayer (red) CrSBr. **f**, Extracted energy shift of the exciton PL peak as a function of magnetic field applied along the *a* axis of bilayer CrSBr. Reproduced from Ref. [63]

These results suggest that the observed tuning of excitonic properties arises from the control of interlayer magnetic order. When the field is applied along the easy axis, the abrupt redshift in the PL spectra of the bilayer corresponds to a spin flip transition (that is, transition from AFM to FM order), which drives a sudden change of the electronic band structure and excitonic transitions. When the field is along the intermediate or hard axes, on the other hand, spin canting leads to continuous changes to the interlayer magnetic order and thus the electronic structure and the PL spectra.

To understand the magneto-electronic coupling in CrSBr, we used first-principles GW-BSE, which provide significantly more accuracy than standard density functional theory (DFT)

calculations. The calculated band structure of bilayer CrSBr in the AFM and FM configurations are shown in (Fig. 2.3-2a-b). Similar to other A-type 2D AFMs, the magnetic ordering of bilayer CrSBr breaks both inversion and time reversal symmetry, but the product of these symmetries is maintained[87]. Such inversion symmetry breaking can enable new magneto-optical effects such as the observed giant SHG and activated Raman modes in bilayer CrI_3[45,87]. Here, it makes the band structure of AFM bilayer CrSBr degenerate in spins, with spin-up and spin-down electrons in each Bloch band localized within specific layers according to the layer's magnetization.

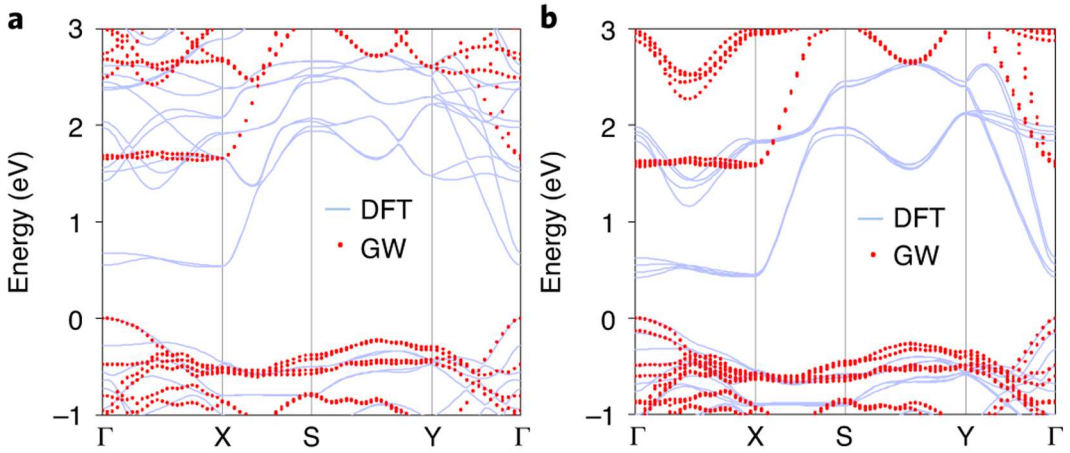

Figure 2.3-2 | Calculated band structure in AFM (**a**) and FM (**b**) bilayer CrSBr. Blue and red dots are the Kohn–Sham band energies computed by the DFT-Perdew–Burke–Ernzerhof method and quasiparticle band energies calculated with the GW method, respectively. In the AFM state, the bands are degenerate in spin, while only majority spins are shown for the FM bilayer since bands with minority spins have much larger gaps. Adapted from Ref. [63]

Calculating the exciton wavefunction in the different magnetic states highlights the magneto-electric coupling of the system. Figure 2.3-3a shows the top view of the real space exciton wave function in AFM bilayer CrSBr. From the top, the wavefunction of the FM and AFM states is very similar, consisting of an anisotropic Wannier type exciton extending over several unit cells. From the side, however, it is apparent that the wavefunctions of the excitons in the AFM and FM bilayer vary dramatically. Fixing the hole in one layer and plotting the wavefunction of the electron

reveals highly layer-localized and delocalized excitons in AFM and FM bilayer CrSBr, respectively. (Figure 2.3-3b-c). The difference in localization can be characterized by using the GW-BSE equations to calculate the ratio of the probability density of the electron wavefunction residing in the top or bottom layers, when the hole is fixed in the bottom layer:

$$\eta^S = \frac{\int_{\boldsymbol{r}_e \epsilon T} \rho^S(\boldsymbol{r}_e) d\boldsymbol{r}_e}{\int_{\boldsymbol{r}_e \epsilon B} \rho^S(\boldsymbol{r}_e) d\boldsymbol{r}_e}$$

where $\mathbf{r}_e$ is the electron coordinate running over the top (T) and bottom (B) layers, respectively, and $\rho^s(\mathbf{r}_e)$ is the integral of the wavefunction module square (i.e., probability density). The result gives $\eta^S < 0.5$ % for the AFM and $\eta^S > 50$ % for the FM states. That is, the probability density for the bound electron to reside in the layer other than the hole is >50 times greater in the FM state.

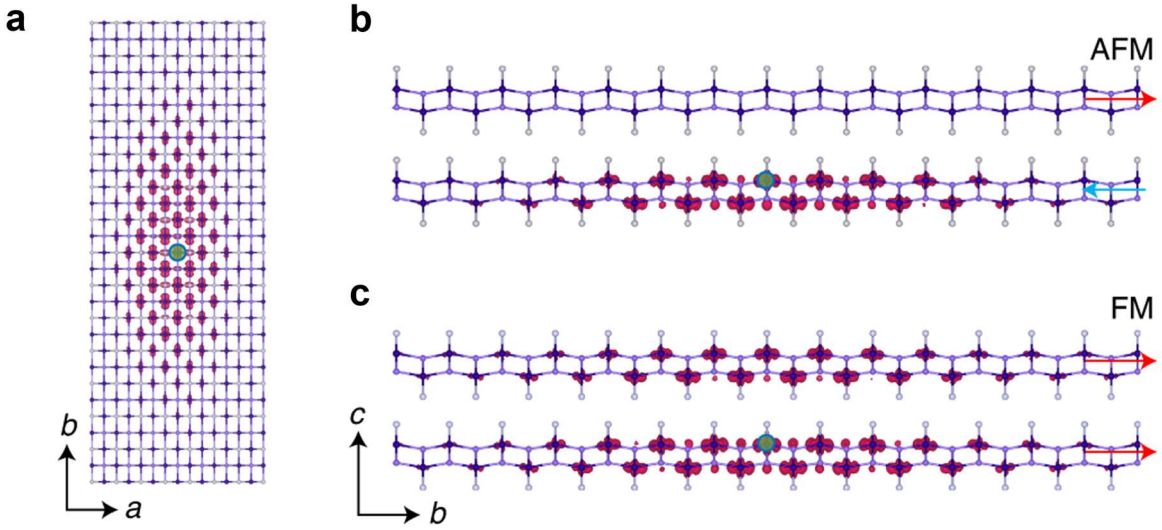

Figure 2.3-3 | Real space calculated wave function for the lowest-energy exciton in bilayer CrSBr. The spatial extent of the wavefunction is shown by $|\varphi_e|^2$ for the electron with the bound hole fixed near a Cr atom (green circle) in the bottom layer. The magenta iso-surfaces show $|\varphi_e|^2$ set at 1% of its maximum. **a,** Top view in the AFM state. **b,c,** Side view of the exciton wavefunction in the AFM and FM states, respectively. The exciton is effectively layer-polarized in the AFM case and delocalized in the FM one. Adapted from Ref. [63]

2.4 Coherent Exciton Magnon Coupling in CrSBr

A common pedagogical concept in quantum mechanics is that of wave-particle duality[88]. We often first learn this concept in the context of photons and light waves, perhaps in high school. While many find this notion bizarre at first, it turns out to be useful in understanding a variety of condensed matter phenomena where the elementary excitations of Hamiltonians can be cast as waves carrying quantized amounts of energy with corresponding quantized quasiparticles. For instance, sound or vibrational waves in crystals come as quantized excitations known as phonons[89,90]. In magnetic systems, the excitations are spin waves[91-93]. To gain a basic physical picture, we start by considering a ferromagnetic chain shown in Figure 2.4-1a. The excited state of the system has a single spin with reversed magnetization (Fig. 2.4-1b). Semi-classical considerations intuitively tell us that the flipped spin will apply a torque to the other spins, thereby tilting them. Those tilted spins will then apply torque on the neighboring spins, and so on and so forth. The result is a propagating spin wave (Fig. 2.4-1c). In quantum mechanical terms, the

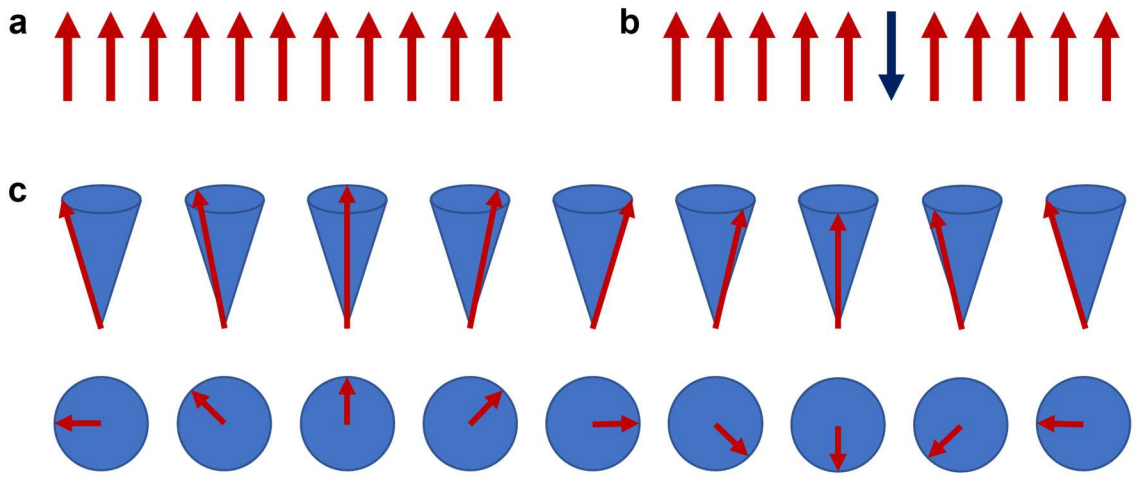

Figure 2.4-1 | Magnons: quasiparticle excitations of the magnetic order. **a,** Illustration of simple ferromagnetic spin chain. **b,** The low-energy excitation corresponds to the flipping of a single spin due to, e.g., thermal energy. **c,** The true nature of the magnetic excitation is a propagating spin wave (top: side view, bottom: top view), with a corresponding quantized quasiparticle known as a magnon.

corresponding quasiparticle is known as the magnon, with the quantized energy corresponding to that required for a single spin-flip excitation.

Magnons have been the subject of intense research for many decades as potential alternative information carriers to standard electrical currents. These magnonic devices can perform novel wave-based computing schemes without suffering from Ohmic dissipation found in electronic circuits[94-97]. In contrast to well-established magnon platforms such as YIG[98], 2D materials could open new possibilities for studying and controlling novel magnon physics due to their remarkable tunability, ability to form vdW heterostructures, and emergence of new physics in the atomically thin limit[99,100]. However, probing magnons in such atomically thin materials poses experimental challenges for conventional methods like neutron scattering[101,102] and microwave resonance[103,104]. Still, effective optical and transport probes such as RMCD[23], Raman spectroscopy[46,64] (see Section 2.5) and electronic tunneling[105-107] enabled effective measurement of spin waves in 2D materials.

The strong exciton transitions in CrSBr could open new possibilities for the coherent detection and control of magnon and their dynamics to the atomically thin limit. In the previous section, we learned that the exciton energy is dependent on the angle between spins in adjacent layers. Therefore, propagating propagating oscillations of the spin structure, i.e., magnons may intuitively couple to the excitons. Here, we consider the magnon modes for CrSBr when a field is applied along the *a*-axis, canting the spins within each layer and lowering the exciton energy (Figure 2.4-2a). In this condition, there are two modes: the acoustic magnon where the spins in each layer oscillate in-phase, and the optical magnon with out-of-phase procession between the layers (Figure 2.4-2b). Since the angle between layer macrospins (see arrows in Figure 2.4-2c) does not change for the acoustic magnon, the energy of the exciton is not modulated (blue line).

On the other hand, the changing spin alignment of the optical magnon mode coherently modulates the exciton energy (red line). The corresponding shift over the precession period is shown in Figure 2.4-2c. Since the in-phase mode does not directly couple to the exciton, we label it as the "dark" mode (|D>). Correspondingly, we label the out-of-phase magnon as the "bright" mode (|B>).

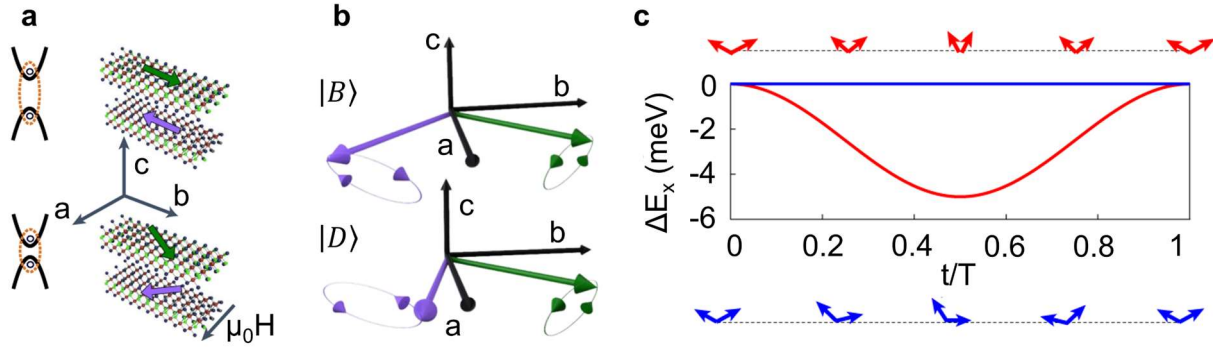

Figure 2.4-2 | Magnon-exciton coupling in CrSBr. **a,** Diagram of the field and spin (purple and green arrows) alignment. The spin canting lowers the exciton energy (left). **b,** Depiction of the two different magnon branches present when the field is applied purely along the *a* axis, corresponding to out-of-phase (top) and in-phase (bottom) spin precession. **c,** Calculated modulation of the exciton energy over the magnon period for the dark (blue) and bright (red) modes. The arrows on top and bottom indicate the spin alignment. Adapted from Ref. [48]

The coherent exciton-magnon coupling enables ultrafast probing of magnon dynamics through pump-probe reflectance measurements. In this experiment, an above-band (normally ~ 405 nm) pump beam puts energy into the system, generating magnons that shift the exciton energy in and out of resonance with the probe beam (normally ~ 910 nm). This consequently modulates the amount of light absorbed by CrSBr, as seen in the strong oscillations of the pump probe signal (Figure 2.4-3a). By taking the Fourier transform of the time dependent data, we obtain the magnon frequency. Applying an external magnetic field perfectly along the *a* axis results in a continuous energy shift of the bright magnon (2.4-3b). Theoretically, the field-shift of the magnon can be treated using the standard Landau-Lifshiftz-Gilbert (LLG) equation to obtain a set of differential

equations modelling the spin dynamics (see Appendix AI.2). The calculated magnon dispersion of both the bright and dark magnon modes are labelled and shown by the grey dashed line.

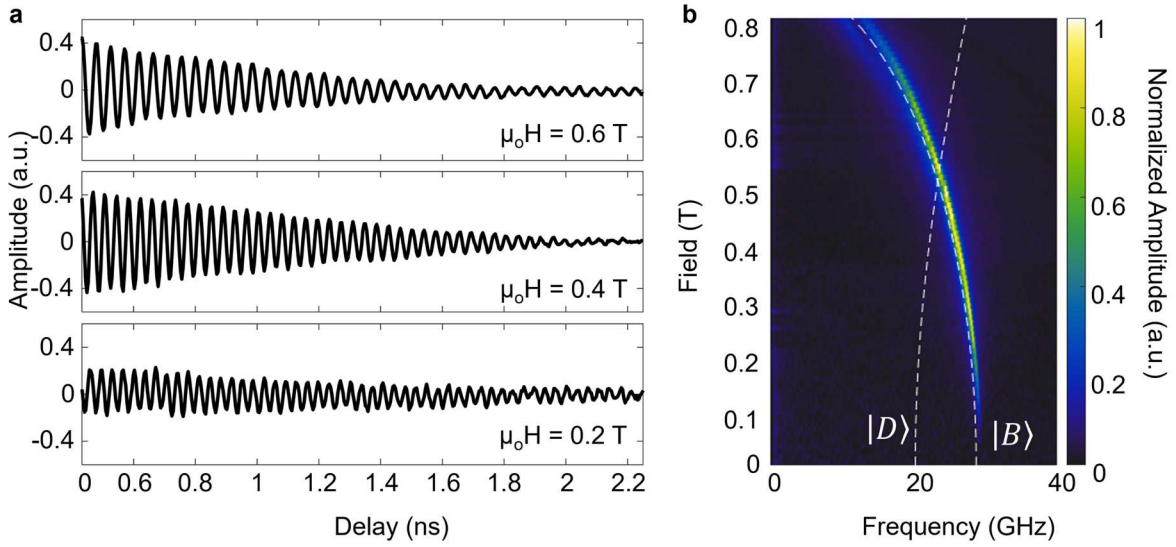

Figure 2.4-3 | Pump-probe signatures of magnon modes. **a,** Transient reflectivity as a function of pump–probe delay with select magnetic field ($\mu_0 H$) values applied along the *a* axis. **b**, Fourier transform of the entire pump-probe data set. The white dashed lines are the calculated magnon frequencies for the bright (|B⟩) and dark (|D⟩) modes. Adapted from Ref. [48]

In addition to tuning the energy of the magnon mode, we also observed changes to the intensity of the oscillations. Since the spin-dependent portion of the exciton energy $E \propto \cos(\theta_0 + \delta\theta(t))$, the magnon modulates the exciton by $\frac{dE}{\theta_0} \propto \sin(\theta_0)$ where θ is the angle between spins in the two layers. This explains why the coupling strength, which dictates the magnitude of the pump-probe oscillation, vanishes in both the collinear AFM state ($\theta_0 = \pi$) and spin-polarized state ($\theta_0 = 0$). We also notice that the dark mode is truly optically dark in this condition, which is a result of the perfect alignment of the applied magnetic field to the crystal *a* axis. In the case of perfect field alignment, the two-fold rotational symmetry of the crystal is maintained. This symmetry enables us to decouple the LLG into two sets, which correspond to modes which are even and odd when C_2 (i.e. rotation by π) is applied, i.e., the dark and bright modes.

Rotating the orientation of the magnetic field with respect to the sample changes the situation dramatically. Figure 2.4-4a shows the field-dependence of the magnon when a field is applied at an angle of roughly ~ 2° with respect to the *a* axis. The magnon spectrum under tilted field features a prominent avoided crossing at intermediate magnetic fields, which demonstrates the coherent hybridization of the bright and dark magnon modes. Taking linecuts at specific magnetic fields, we observe strong beating between the dark (|D>) and bright (|B>) magnon modes (Figure 2.4-4b). We can express the contributions of the bright and dark magnon modes as $\alpha|D\rangle \pm \beta|B\rangle$ with the coefficients α and β being controlled by the magnetic field. When off-resonance, the magnon has character which is primarily from one mode or the other. However, at the avoided crossing ($\mu_0 H = 0.53$ T), the two distinct magnon modes become coherently hybridized with nearly

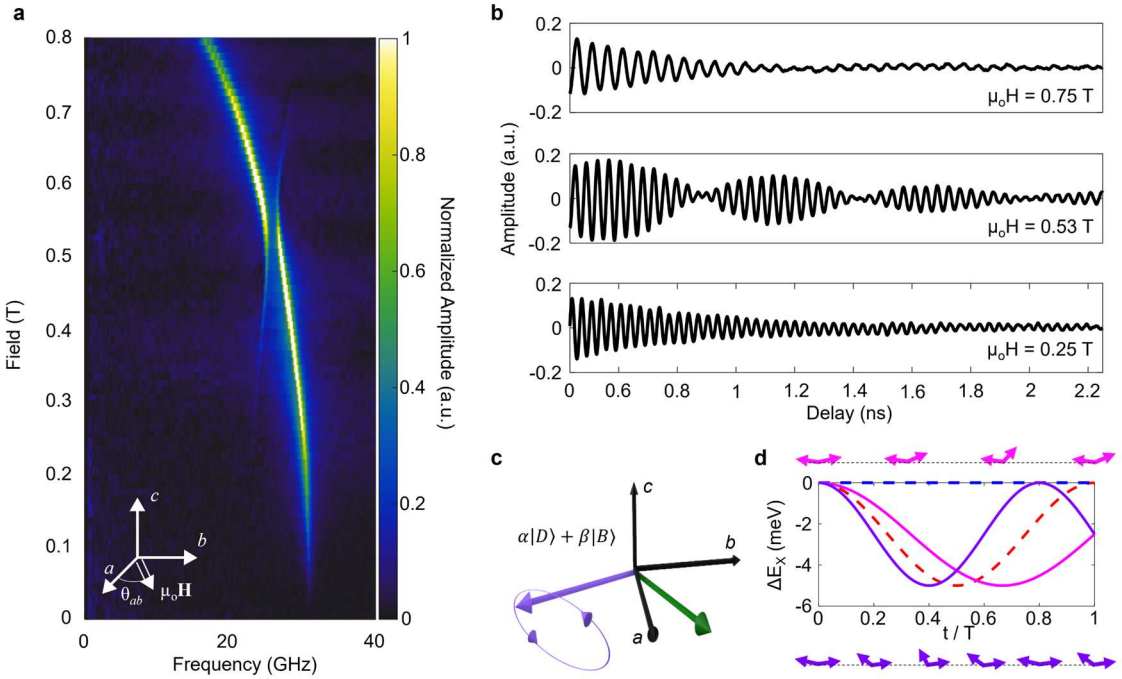

Figure 2.4-4 | Magnon hybridization under tilted magnetic field. **a,** Magnon dispersion with the magnetic field applied at an angle $\theta_{ab} = 2°$ from the *a* axis (see inset). **b**, Transient optical reflectivity taken at select magnetic field values. The strong beating pattern at 0.53 T is attributed to the magnon hybridization. **c**, Diagram of one of the fully hybridized magnon modes. **d**, Calculated exciton resonant energy shift during the precession of the hybridized magnon modes, shown in magenta and purple. The dashed lines correspond to the uncoupled magnon modes, studied in Figure 2.4-3. The arrows show the time-dependent relative angle between spins during the period of the precession. Reproduced from Ref. [48]

equal contributions. This is allowed because the magnetic field breaks the symmetry of the system, allowing for new normal modes with mixed character (see Fig. 2.4-4c for the magnon motion). In contrast to the field-aligned case, both hybridized modes vary the relative angle between spins, thus producing a time-dependent modulation of the exciton energy as shown in Figure 2.4-4d. It is further worth noting that the magnon lifetime increases at the avoided crossing, where the linewidth narrowed by a factor of three with respect to the purely |B> magnon. The tunability in lifetime may be exploited in spintronic applications that require long lifetimes and spin transport lengths.

The frequency splitting, Δ, at the avoid crossing gives the coupling strength of the two modes. This coupling strength can be tuned by rotating the angle of field with respect to the *a* axis, θ_{ab}. Figure 2.4-5a shows the magnon dispersion curves at varying θ_{ab}. We find that increasing θ_{ab} increased Δ, i.e. the coupling between the acoustic and optical magnons. As a result, the brightness

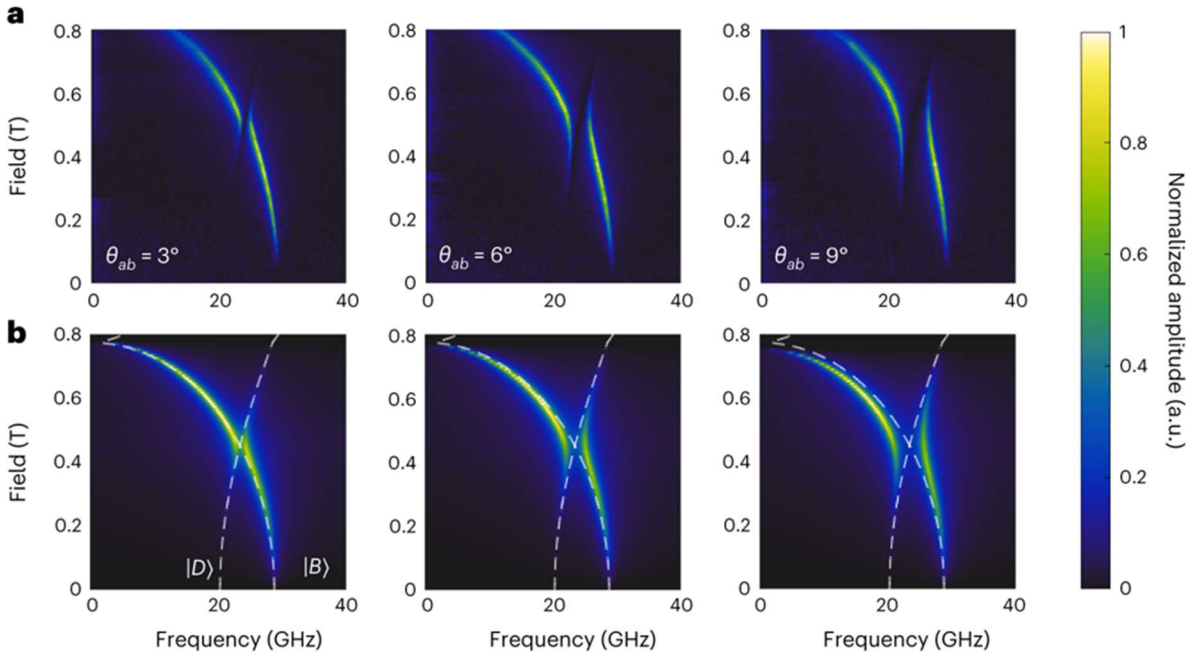

Figure 2.4-5 | Tuning exciton-hybridized magnon coupling via symmetry-breaking magnetic field. **a,b,** Experimental (**a**) and theoretically modelled (**b**) magnon dispersion curves for varying θ_{ab}. Reproduced from Ref. [48]

of the |D> mode also increases. This brightening is evident at the tails extending beyond the avoided crossing which have a dispersion matching the dark mode.

Figure 2.4.5b shows that our theoretical models capture the behavior of the observed data excellently, enabling the analysis of the magnetic properties, e.g., anisotropy and interlayer exchange, of the system. Extracting the coupling strength and amplitude of the dark mode reveals a linear dependence on θ_{ab} (Figure 2.4.6a-b). The former observation is clearly demonstrated by the dramatic tuning of the beating pattern as the fixed field of $\mu_0 H = 0.55$ T is tilted (Fig. 2.4.6c).

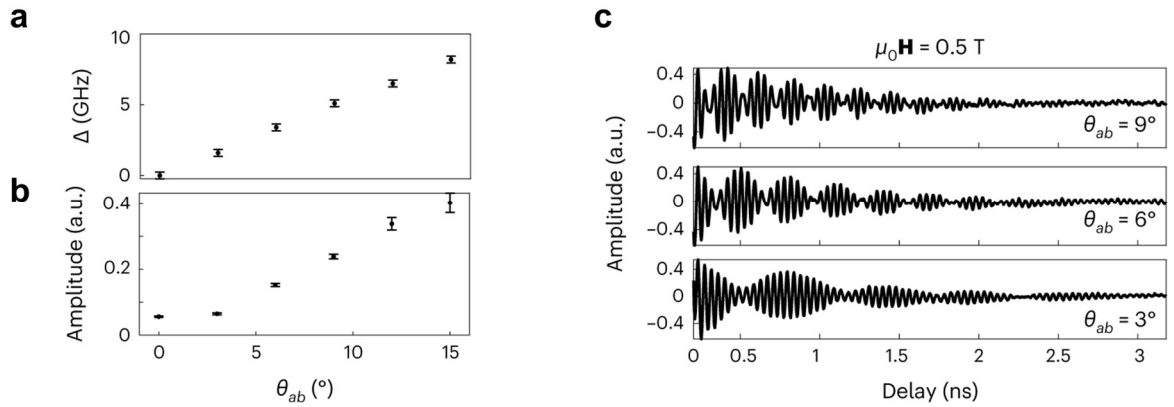

Figure 2.4-6 | Extracted values of hybridized magnon-magnon interactions. **a-b,** Energy splitting (**a**) and amplitude (**b**) of the hybridized modes at fixed magnetic field as a function of the field angle The field is set to $\mu_0\mathbf{H} = 0.55$ T for **a** and 0.3 T for **b**. **c,** Time traces with a fixed magnetic field of 0.5 T applied at selected angles. Adapted from Ref. [48]

In this section, we have demonstrated that the coupling of magnetic and electronic properties in CrSBr enables tunable coherent interactions between excitons and magnons. By applying fields of appropriate strength and direction, we found that the exciton coupling to the dark mode can be completely turned on/off, and that the hybridization strength between acoustic and optical magnon modes can be tuned from zero to strong coupling. These results additionally demonstrate that the properties and dynamics of the system can be well modelled using the LLG, a fact which will prove useful when we study strain-dependent magnetism in Chapter 5. More broadly, the interaction between gigahertz magnons and near-IR excitons provides new

opportunities for hybrid quantum information systems[47]. For instance, CrSBr could provide a highly tunable system for quantum transduction, which is the transfer of information between different quantum nodes such as microwave-driven qubits and optical excitations.

2.5 RAMAN SPECTROSCOPY: ANOTHER OPTICAL PROBE OF HIGH-ENERGY MAGNONS IN 2D MAGNETS

In the previous section, we found that the exciton-magnon coupling in CrSBr enables coherent detection of the magnon excitations. However, as mentioned in the introduction, many 2D magnets are too insulating with Frenkel-type excitons that do not couple strongly to magnons in the 2D limit. An alternative technique which has been successfully used in a variety of systems is Raman spectroscopy. Raman spectroscopy is most commonly used as a sensitive probe of the phonon modes in the crystal, but it can also probe zone-center (k = 0) magnon modes as long as the frequency is large enough to be separated from the laser line[92,108,109]. By using state-of-the art filters with sharp cut-off edges, we can probe energies down to ~ 3 cm^{-1}, equivalent to ~ 90 GHz. The CrSBr magnons (~20-30 GHz) studied in the previous section are thus too low energy to be studied using Raman, though similar techniques which can resolve lower frequencies, such as Brillouin Light scattering, could be possibly employed.

While the low energy magnons in CrSBr cannot effectively be probed through Raman spectroscopy, we found that the prototypical 2D magnet CrI_3 features sufficiently high energy acoustic magnons. In the monolayer, CrI_3 has ferromagnetic ordering with the spins pointing out of plane below a T_C ~ 42 K, as shown by the square-shape RMCD hysteresis loop (Appendix AI.1b). Figure 2.5-1a shows the low-energy cross-polarized Raman spectra of monolayer CrI_3 under circularly polarized excitation. At zero field, the spectra are featureless besides strong Rayleigh scattering centered at 0 cm^{-1}. However, when a strong magnetic field along the out-of-

plane direction is applied, a low-frequency peak appears. This mode appears on both Stokes (positive) and anti-Stokes (negative) sides of the spectra, which are labelled as AM and AM*, respectively. AM and AM* have opposite optical selection rules. For example, when the magnetization points down (Fig. 2.5-1b), a σ+ photon can only generate the AM mode which has nearly perfect σ− polarization (σ+/σ−), while the AM* mode is excited by σ− polarized light and

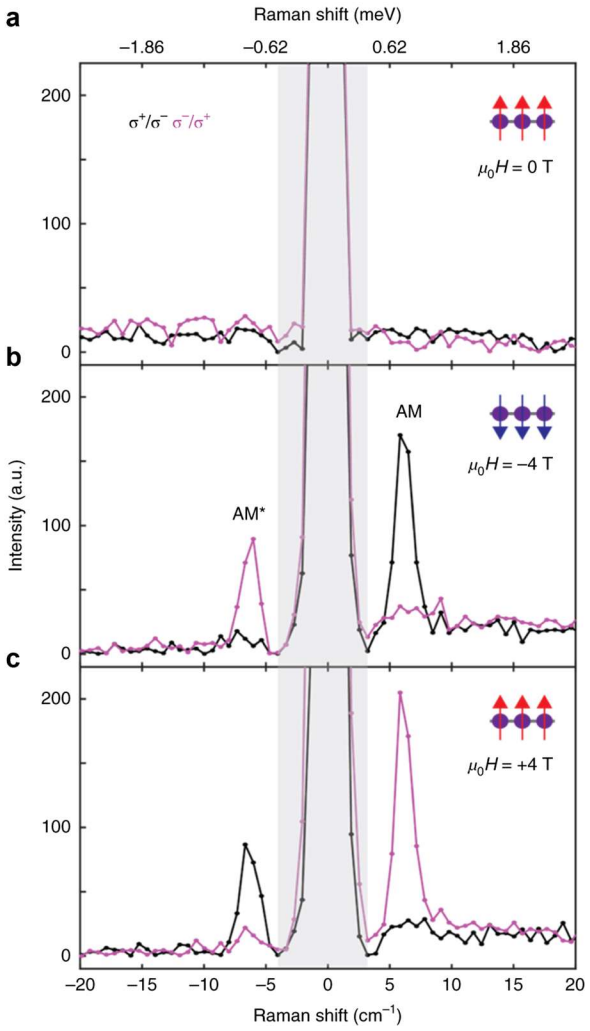

Figure 2.5-1 | Low-energy cross-circularly polarized Raman scattering in monolayer CrI_3 with magnetic fields of 0 T (**a**), -4 T (**b**), and +4 T (**c**) applied, respectively. The inset diagram denotes the spin orientation. Traces in pink (black) correspond to σ^- (σ^+) excitation, with the collection channel being the opposite. The grey line denotes the cutoff of the Bragg filters used to achieve low energy sensitivity. Adapted from Ref. [64]

appears in the σ+ channel (σ−/σ+). When the direction of the field is reversed, the selection rules are as well (Fig. 2.5-1c).

Since the magnetic field lies along the magnetization direction, the magnon energy will increase with increasing field due to the Zeeman effect. We should expect that this will increase the magnon energy with a slope of 0.94 $cm^{-1}T^{-1}$ (0.12 $meVT^{-1}$), the Zeeman energy shift expected[100,109] for a spin S = 1 quasiparticle with a magnetic moment of 2 μ_B. Figure 2.5-2a shows the intensity plot of AM and AM* as a function of Raman shift and magnetic field. The extracted peak positions at each field are plotted in Figure 2.5-2b, showing an excellent agreement between the energy shift of AM and AM* and the expected Zeeman energy shift. The zero-field intercept gives the spin-wave gap, which we find to be ~ 2.4 cm^{-1} (or ~0.3 meV) for monolayer CrI_3. We note that this spin-wave gap is rather large for a ferromagnet owing to the strong magnetic anisotropy and is in good agreement with the theoretical predictions in Ref.[110,111].

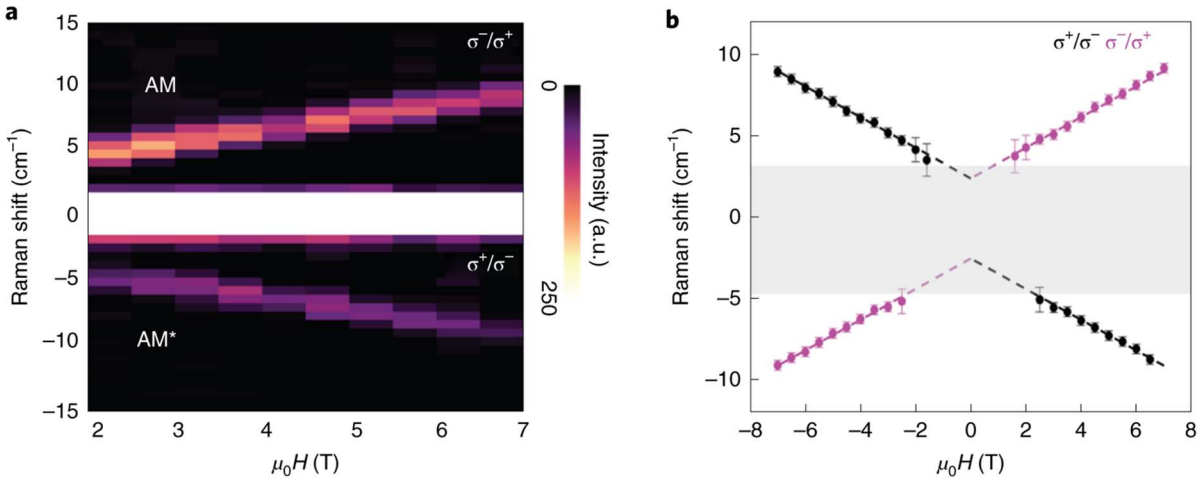

Figure 2.5-2 | Magneto-Raman measurements on monolayer CrI_3. **a,** Intensity plot of the low-energy Raman features as a function of applied magnetic field in the range from 2 to 7 T. Data higher than 0 cm^{-1} are from the σ^-/σ^+ channel while the data lower than 0 cm^{-1} are taken in the σ^+/σ^- channel. **b,** Magnon energies obtained by Lorentzian fits over the entire field range. The dashed line shows the Zeeman energy shift for a quasiparticle with zero-field energy of 2.4 cm^{-1} and spin S=1. The error bars represent the uncertainty of the fit, while the grey region is inaccessible to our experiment due to the optical filters. Adapted from Ref. [64]

In contrast to the C_2 rotational symmetry of CrSBr, CrI_3 has C_3 rotational symmetry (Fig. 2.5.3) which dictates the distinct optical selection rules. We can derive these rules by considering the change in angular momentum of the incident and outgoing photons, J_p, and magnon, J_m, in the honeycomb lattice (Fig. 2.5.3). Taking the case when the magnetization points up, the overall change of the photon's angular momentum is $\Delta J_p = \pm 2\,\hbar$ since the helicities between incident and scattered light are opposite, where + (−) corresponds to AM* (AM). In addition, the magnon angular momentum changes by $\Delta J_m = \pm\hbar$. The total change of angular momentum is then $\Delta J_p + \Delta J_m = \pm 3\,\hbar$. In an analogue to the Umklapp process[112,113], the three-fold (C_3) symmetry of the honeycomb lattice allows for discrete angular momentum conservation modulo $3\hbar$: $|\Delta J_p + \Delta J_m|/\hbar = 0 \pmod 3$. The observed cross-circularly polarized optical selection rule corresponds to such a $3\hbar$ process and is therefore allowed. It is interesting to note that the selection rules seem to be relaxed in the bulk crystal, where a significant signal is detected in the co-circularly polarized channel (See Appendix AI3 for comparison). That may be due to the presence of stacking faults and other defects which relax the symmetry constraints in comparison to the pristine monolayer.

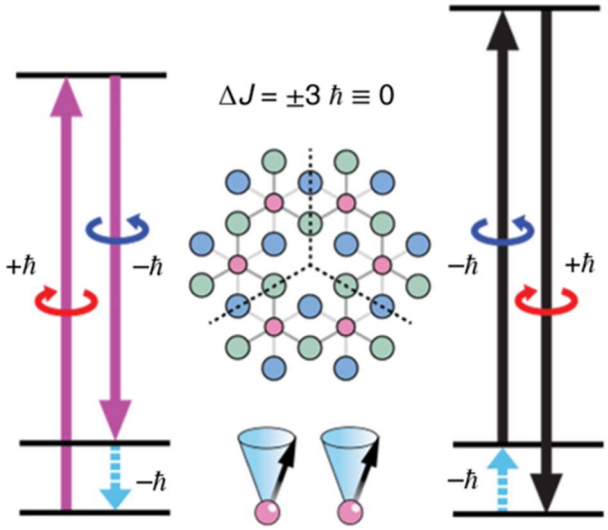

Figure 2.5-3 | Optical selection rules for the one-magnon Raman scattering process in monolayer CrI_3. The left (right) energy diagram corresponds to Stokes (anti-Stokes) processes in the spin-up state. Due to the C_3 rotational symmetry in the honeycomb CrI_3 lattice shown in the middle, the total change in angular momentum of $\pm 3\,\hbar$ is equivalent to 0. Pink, green and blue circles represent Cr^{3+}, top I^- and bottom I^- ions respectively. Adapted from Ref. [64]

When monolayers of CrI_3 are stacked on top of each other, the A-type AFM order modifies the magnon energies and breaks the inversion symmetry of the system. The zero-field magnon energy of AFM bilayer CrI_3 is theoretically equal to $\sqrt{(2J_{inter} + K)K}$ where K is the magnetic anisotropy, and J_{inter} is the AFM interlayer exchange interaction[114]. As in the case of the monolayer, the anisotropy can be found by fitting the high-field FM linear shift and taking the zero-field intercept. Figure 2.5-4 shows the field-dependent magnon energy obtained by Lorentzian fits of the spectra. The green and yellow lines represent the two acoustic AFM magnon branches (see inset and previous discussion on magnons in CrSBr), while the blue line is the high-field FM mode. Based on the fits, we extract $K \sim 0.27$ meV, and $J_{inter} \sim 0.11$ meV. These numbers confirm that CrI_3 is in the weak-exchange limit, as further evidenced by the sharp spin-flip transition seen at the dashed line in Fig. 2.5-4 and in multiple prior investigations of bilayer CrI_3[23].

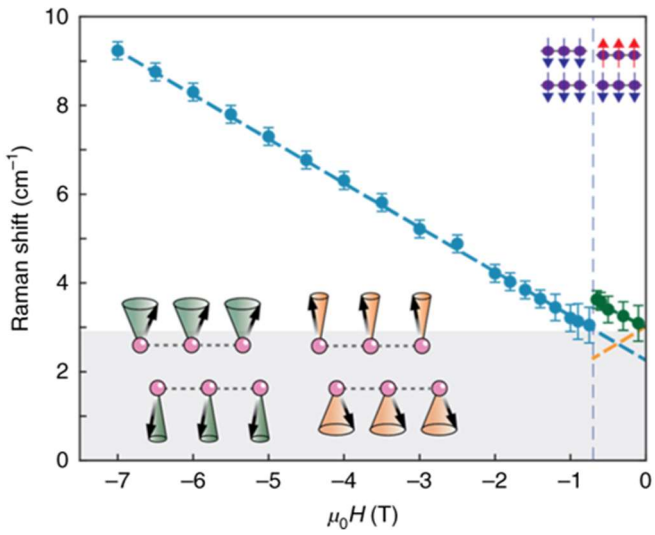

Figure 2.5-4 | Probing magnetism and spin-flip transitions in bilayer CrI_3 *via* magnons[3]. A linear fit of the acoustic magnon energy at high fields (depicted as the dashed blue line) demonstrates a Zeeman shift characterized by a g factor of approximately 2.1 and an intercept of 2.2 cm^{-1} (equivalent to 0.27 meV). At the spin-flip transition (grey line), the bilayer switches to the layered AFM state, expected to harbor two distinct magnon modes with opposite field-dependence. These two modes are visually represented in the inset at the bottom left corner. Adapted from Ref. [64]

In addition to modifying the magnon energy, we observed an additional, higher energy mode at ~ 140 cm^{-1} that appears only in bilayer and thicker CrI_3. This weaker feature has the same cross-polarized selection rule as the monolayer (Fig. 2.5-5a) and distinctive linear magnon Zeeman

shift with applied field (Fig. 2.5-5b). Based on these properties and previously reported neutron scattering results[101], we identify the high energy peak as the optical magnon (OM) corresponding to out-of-phase intralayer spin precession. To understand the emergence of this mode in multilayer flakes, we can consider how the weak interlayer coupling modifies the phonons of the system. In a previous study[45], we treated bilayer CrI_3 as a coupled spring system and found that the weak vdW interactions between layers split each phonon into two, a phenomenon known as Davydov splitting. Since the lattice of CrI_3 has inversion symmetry, the two modes correspond to even and odd-parity modes, the Raman activity of which is determined by the magnetic state. The same treatment can be applied to the magnons. In inversion symmetric monolayer CrI_3, the high-energy OM, corresponding to out-of-phase intralayer spin procession, is Raman silent because it is odd under parity (Fig. 2.5-5c). In bilayer, however, the modes are split, and the parity-even OM becomes Raman active (Fig. 2.5-5d-e). The energy of the optical mode is given by $E = K + 6J_{intra}$, where J_{intra} is the intralayer exchange. Therefore, we obtain a value of ~ 2.83 meV for J_{intra}.

Antiferromagnetic materials exhibiting easy axis anisotropy, such as the bilayer CrI_3 under consideration, generally accommodate two magnon modes for each branch which are initially degenerate in energy when no magnetic field is applied, but which possess opposing angular momenta. The presence of the layered AFM order breaks inversion symmetry, thus relaxing the parity-based selection rules. As a result, both optical branch magnon (OM) modes become Raman-active (Fig. 2.5-5f). When a magnetic field is applied, these two modes have opposite Zeeman energy shifts—specifically, one mode undergoes a blueshift while the other experiences a redshift. This picture explains the Raman activity of OM modes in both cross-circular channels and the contrasting energy shifts of the two modes, as depicted in Fig. 2.5-5h.

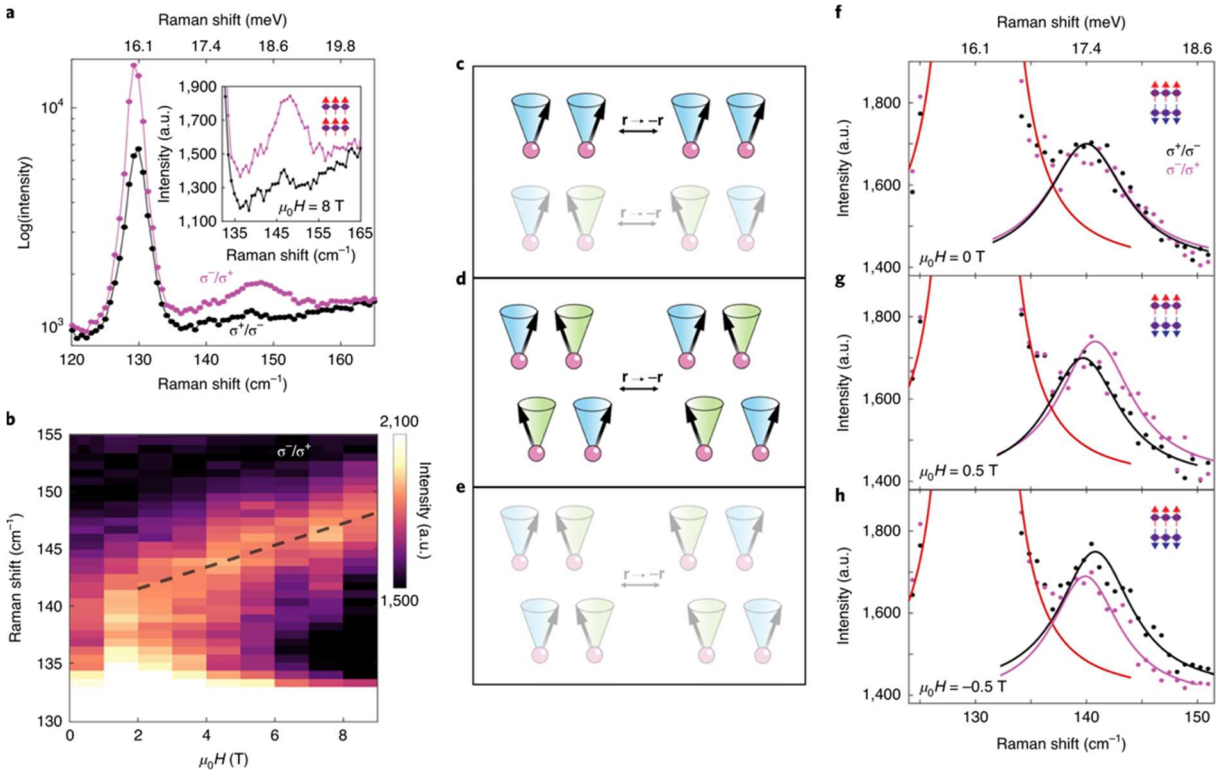

Figure 2.5-5 | Optical magnons in bilayer CrI_3. **a,** Raman spectra obtained from bilayer CrI_3 under an applied magnetic field of 8 T, with the intensity plotted logarithmically. Inset: A zoomed-in plot of the cross-circularly polarized feature centered around ~148 cm^{-1} (corresponding to 4.4 THz or 18.4 meV). **b,** Intensity plot of the optical magnon (OM) as a function of applied magnetic field. The observed shift is consistent with the expected g factor of ~ 2 (illustrated by the dashed black line), confirming its nature as a magnon. **c,** Depiction of acoustic and optical magnons within the CrI_3 monolayer unit cell. Following the application of the inversion operator, r→-r, the acoustic magnon remains unchanged, while the OM accumulates a π phase shift in its spin precession. Given the centrosymmetry of the monolayer, the parity-even acoustic magnon is Raman-active, whereas the parity-odd OM is Raman-inactive (faded in the illustration). **d, e,** Schematics illustrating the optical magnons (OMs) within a ferromagnetic CrI_3 bilayer. The Davydov-like splitting of the OM mode in the monolayers gives rise to a parity-even, Raman-active mode (**d**) and a parity-odd, Raman-silent mode (**e**). **f,** Raman spectra of bilayer CrI_3 at zero magnetic field. The solid lines, presented as visual aids, represent Lorentzian functions outlining the Raman scattering originating from the OM modes (black and pink) as well as the neighboring A_{1g} phonon mode (red). Unlike the pronounced selection rule for a single scattering channel observed in the ferromagnetic-like state (e.g., σ−/σ+ for panel **a**), the OM in the antiferromagnetic state at zero field has a near-equal presence in both cross-circular channels. **g**, With the application of a magnetic field, a separation in energy between the two OM modes becomes apparent, corresponding to a blueshift in the σ−/σ+ mode and a redshift in the σ+/σ− mode. **h,** Reversal of the direction of the applied magnetic field results in a corresponding reversal of the energy shift exhibited by the modes. Reproduced from Ref. [64]

In this chapter, we explored the signatures of magnetic ordering in 2D materials via optical measurements. We demonstrated that measurements of PL and pump probe in CrSBr and Raman in CrI_3 provide remarkably sensitive probes of magnetic order when combined with accurate theoretical modeling and understanding. The enhanced signal to noise due to the exciton resonance and ability to directly measure the magnon dispersion and dynamics make CrSBr an exceptional platform for optically investigating magnetism on the nanoscale. For realizing practical electrical devices, however, it is desirable for the material to have a coupling between the charge transport and magnetic order. We will establish this in the next Chapter.

Chapter 3. TRANSPORT PROBES OF MAGNETISM IN CRSBR

In the previous chapter, we established that the excitonic and optical properties of CrSBr are directly connected to its magnetic order. Considering excitons consist of electrons and holes, i.e. charge carriers, we may naively expect the electronic transport should also be sensitive to magnetic ordering. Such coupling of charge transport to magnetic ordering is required for many of the spintronics device schemes[115] proposed over the past several decades such as spin valves[49,116-120] and spin logic devices[121,122]. The emerging vdW magnets offer a new platform to explore such spintronics devices down to the atomically thin limit.

A challenge, however, is that many of the magnetic "semiconductors" discovered early on, e.g., CrI_3, are extremely insulating and electrical contacts cannot be turned on even when a large gate voltage is applied. To overcome this challenge, several groups including the Xu group, developed all-vdW magnetic tunnel junction (MTJ) devices which utilize the 2D magnet as an insulating tunnel barrier[100,105,106,123,124]. The intrinsic A-type AFM order effectively produces atomically sharp spin-filters which generate record high tunneling magnetoresistance. In this Chapter, we will explore both standard lateral magneto transport in a dual gated trilayer CrSBr device, and vertical electron tunneling in a bilayer CrSBr MTJ.

The results presented in this section are mostly unpublished, though similar results were published by our collaborators at Columbia in their Nature Materials paper[62]. In addition, further details on the vdW MTJs are ubiquitous[100,105,106,123,124] in the literature.

3.1 MAGNETO-TRANSPORT MEASUREMENTS OF TRILAYER CRSBR

A fundamental challenge facing the study of 2D semiconductors like CrSBr is the ability to form good electrical contacts at low temperatures[125-127]. The most important consideration is the choice of metal used to make contact, since a Schottky barrier can be formed depending on the band alignment of the semiconductor and metal. Suitable metals can be chosen by comparing the work function of the metal with the electron affinity of the semiconductor. While thorough characterization of the latter has not been established in CrSBr, it has been established that palladium (Pd) can be used to contact atomically thin CrSBr at cryogenic temperatures[62]. Figure 3.1-1a-b shows the diagram and optical image of a dual-gated 3L CrSBr, respectively. A standard Hall bar geometry is used to measure the longitudinal and transverse (Hall) voltages. The top and bottom graphite gates enable the independent control of vertical electric field and carrier density, both of which can be powerful control knobs for 2D systems. In fact, injecting carriers through gating is an absolute requirement for turning the contacts on at low temperatures where all thermally excited carriers are frozen out.

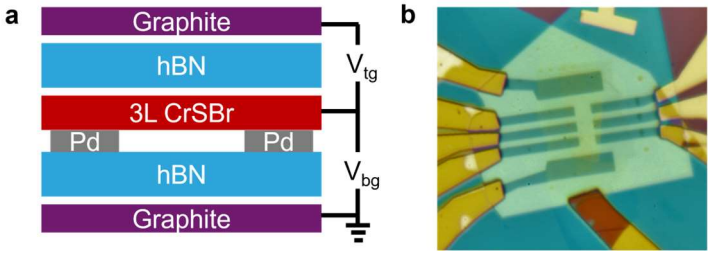

Figure 3.1-1 | Design and optical image of a dual-gated CrSBr device. Applying voltages to the symmetric gates with respect to ground allows independent control over both carrier density and vertical electric field.

The resistance of the device as a function of top and bottom gate voltage at a temperature of 60 K is shown in Fig. 3.1-2a. Since hBN flakes with symmetric thickness were chosen as the gate dielectrics, it is straightforward to convert the gate map to carrier density and displacement field by using a simple parallel plate capacitor model. Applying this procedure, we obtain the color map shown in Fig. 3.1-2b. Notably, the resistance becomes much smaller at higher carrier

density. This is important because at temperatures below ~ 40 K, the resistance starts to dramatically increase and the phase of the lock-in becomes very large, indicating that the AC measurement scheme is no longer valid at zero gate voltage. Applying the symmetric voltage ($V_{tg} = V_{bg}$) to inject carriers, we are able accurately measure resistance down to ~ 10 K at the highest possible gate voltage (Fig. 3.1.2c). However, since we could only measure using a very limited gate range at that temperature, and due to the reports of a secondary, defect-ordered magnetic phase which appears below ~30-40 K[62,128], we will primarily report data taken at a temperature of ~ 60 K for the rest of this subsection, unless otherwise noted.

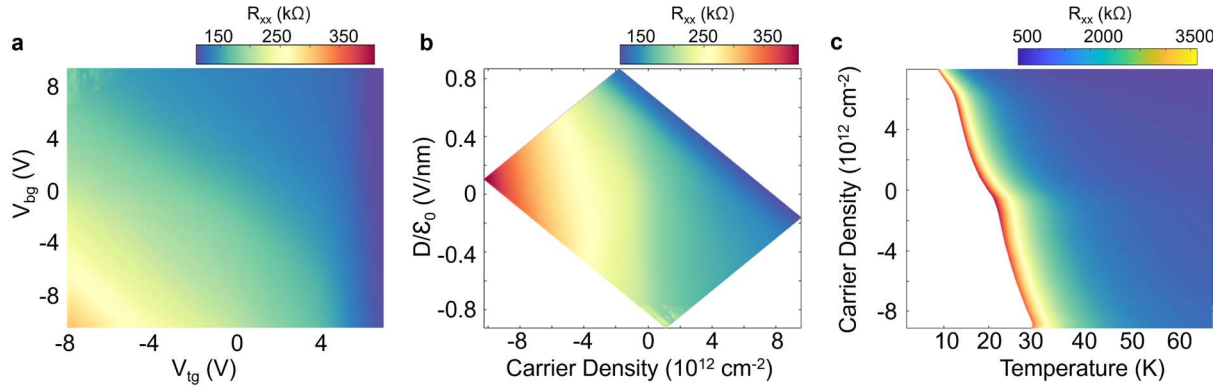

Figure 3.1-2 | Low temperature transport characteristics of a dual-gated trilayer CrSBr device. **a,** Longitudinal resistance taken as a function of top and bottom gate voltage at a temperature of 60 K. **b,** The data from **a** converted to vertical displacement field and carrier density using the parallel plate capacitor model. **c,** Longitudinal resistance as a function of carrier density and temperature. The injected electrons enable AC resistance measurements down to ~ 10 K despite the semiconducting nature of CrSBr.

Figure 3.1-3a shows the longitudinal resistance, R_{xx}, as a function of magnetic field swept up and down along the *b* axis. When the field exceeds the spin-flip field of ~ 0.15 T, the resistance of the sample abruptly decreases. Following the standard procedure, we define the magnetoresistance ratio (MRR) as:

$$MRR = \frac{R(B) - R(B = 0)}{R(B = 0)}$$

Converting the raw resistance to MRR reveals that trilayer CrSBr has a negative magnetoresistance of ~ -7 % between the high and low field states at 60 K and V_g= 0V (Fig. 3.1-3a). The origin of the negative magnetoresistance is illustrated in Fig. 3.1-3b. In the AFM states, electronic scattering processes which would scatter electrons between layers are forbidden due to the contrasting spin-polarization of the layers. On the other hand, when the layers are spin aligned, the electrons can scatter between layers. Considering CrSBr is a rather disordered semiconductor with conduction dominated by variable range hopping[129,130], the AFM state where interlayer hopping is forbidden has significantly larger resistance than the FM state, where it is allowed[60,62].

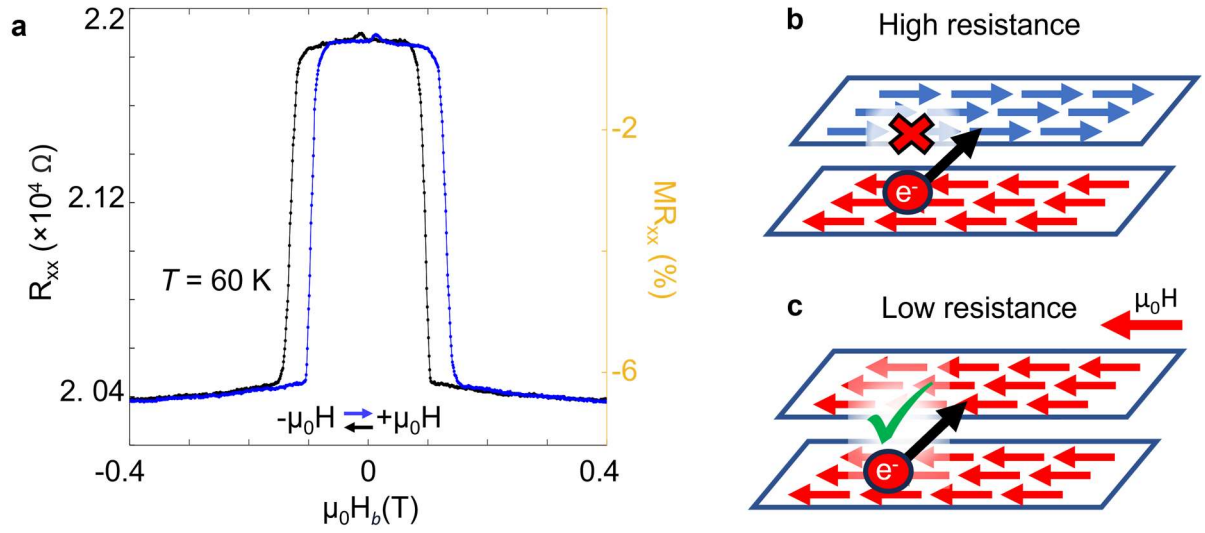

Figure 3.1-3 | Observation and origin of negative magnetoresistance in few-layer CrSBr devices. **a,** Magnetoresistance measurements of the trilayer CrSBr device at V_g = 0 V and T = 60 K. The blue curve represents data where the magnetic field is swept form positive to negative, and the black curve is the opposite sweep direction. The raw data is then converted to the magnetoresistance ratio (right axis) using the equation in the main text. **b,** The suppression of interlayer electronic scattering in the AFM state (top) gives a high resistance in comparison to the field-aligned FM state where such processes are allowed (bottom).

We can use the horizontal sample mount rotator in the PPMS cryostat to study the full in-plane magnetic phase diagram with ease. Figure 3.1-4a shows the MRR as a function of the rotator angle and applied magnetic field. The strong angular dependence of the critical field and saturated

magnetoresistance reflects the anisotropic in-plane magnetic order: as the magnetic field is swept along the *b* axis, i.e., at angles close to 90°, the system undergoes a sudden spin flip transition. At angles close to 0°, however, the MRR evolves continuously with a saturating field of field of ~ 0.7 T (Figure 3.1-4b).

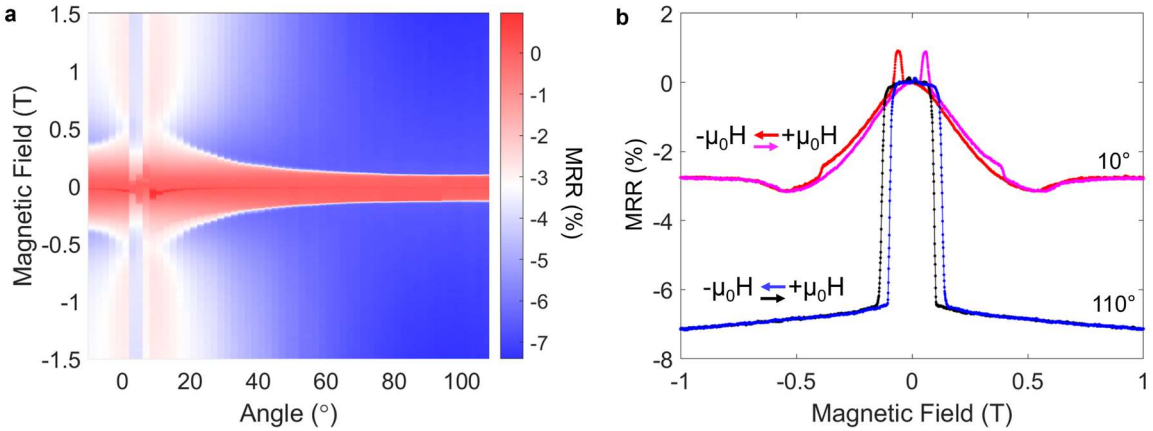

Figure 3.1-4 | Angle-dependent magnetoresistance in atomically thin CrSBr. **a,** Magnetoresistance ratio measurements of the trilayer CrSBr device at various rotator angles. The gates are set to $V_g = 0$ V. **b,** Magnetoresistance sweeps at a fixed rotator angle of 10° and 110°, corresponding to the intermediate and easy magnetic axes, respectively.

These measurements demonstrate that magnetic-state-dependent interlayer electronic coupling can significantly affect the in-plane electronic transport in CrSBr. An interesting question is whether this coupling can work in reverse: can gating the system be used to tune the magnetic order, as in CrI_3[131,132]? This question was thoroughly investigated by Telford, et al. who found that the magnitude and even sign of magnetoresistance in monolayer CrSBr can be controlled by gating[62]. According to their results, the low-temperature (i.e., below ~ 40 K) magnetic structure features ordering of both the intrinsic, dominant Cr lattice and a sublattice of defect spins as seen in similar bulk magnetic semiconductor systems[133-137]. In this picture, the MRR originating from the coupling between magnetic defects and charge carriers strongly depends upon the carrier density. However, it is important to note that there are many mechanisms which generate

magnetoresistance in magnetic semiconductor systems[138-142], and the exact origin of the different types of MRR in CrSBr are not conclusively established yet. In addition, its dependence on crystal quality and thickness has not been explored yet.

In our device, we also found that the MRR can be strongly tuned by gate. Figure 3.1-5a shows MRR sweeps along the intermediate magnetic axis as a function of gate voltage ($V_{tg} = V_{bg}$) at a temperature of 60 K. At a gate voltage of ~ + 6 V, the sign of the high-field MRR rapidly changes from negative to positive. As shown in the linecuts, the strong negative MRR dome completely changes to weak positive MRR under high electron doping (Figure 3.1-5b), while the saturating field remains relatively unchanged. Similar behavior is observed when the field is applied along the easy axis (Figure 3.1-5c). However, in this case, the sign of MRR does not switch from negative to positive, it just becomes a smaller negative value in this gate range.

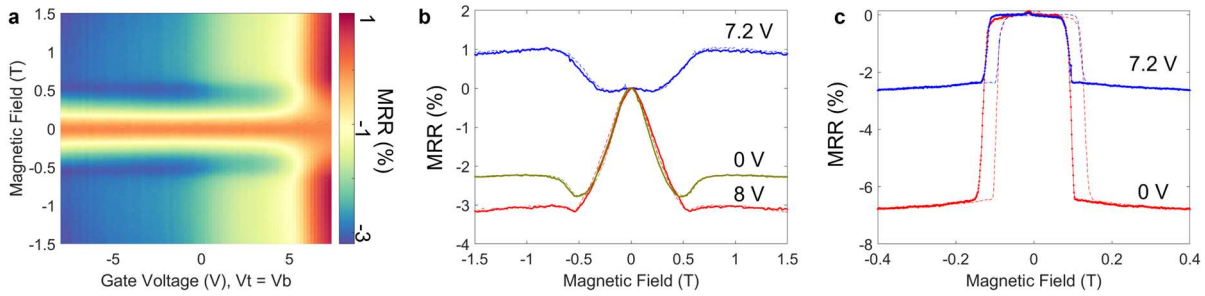

Figure 3.1-5 | Gate tuned magnetoresistance in trilayer CrSBr. **a,** Doping dependent ($V_{tg} = V_{bg}$) magnetoresistance ratio measurements of the trilayer CrSBr device at 60 K. This color map plots data where the magnetic field is swept down along the *a* axis (i.e., from positive to negative values). **b,** MRR from select gate voltages taken from panel **a. c,** Measured MRR curves at 0 V (red) and 7.2 V (blue) with the field swept along the easy *b* axis. The solid and dashed curves in **b,c** correspond to the field being swept down and up, respectively.

The above gate dependence is generally in agreement with that observed by Telford, et al., where they observed a sign change in the MRR of monolayer CrSBr. However, we may expect that the layered AFM order would give rise to a dominant negative MRR which is absent in the monolayer. Therefore, it is somewhat surprising that we are able to tune the MRR all the way from

negative to positive. For instance, in Telford, *et al.*, they observe decreasing negative MRR with electron doping in bilayer CrSBr, but are never able to change the sign to positive. This could be due to a few reasons: the hBN gates used in our study have better gate performance than the silicon gates used by Telford which may enable higher doping, the behavior of trilayer CrSBr may be quite different from the bilayer due to the presence of a net magnetization from an uncompensated layer, the field is applied along the *c* axis in their bilayer data and along the *a* axis in our trilayer data, and finally our sample was fabricated entirely in the glovebox while the one in Ref.[62] was fabricated in air. A more comprehensive study on the origin of gate-tuned magnetoresistance in few-layer CrSBr using various layer thicknesses and full angle and temperature dependent measurements is left for future works.

Upon first consideration, it is somewhat surprising that the magnetoresistance would be so strongly dependent on the magnetic state in lateral transport measurements since spin-polarized electrons could just move within each layer. A more intuitive idea is to perhaps apply the current *perpendicular* to the sample so that the electrons are forced to move through the oppositely polarized layers. This type of device is known as a magnetic tunnel junction (MTJ), and it is a tremendously useful technology.

3.2 THE MAGNETIC TUNNEL JUNCTION: A FUNDAMENTAL SPINTRONIC DEVICE

Many research works and articles describe the field of spintronics as a potential path for next-generation information processing. However, the spintronics device known as a MTJ is in fact already in ubiquitous use in modern computing technology. A rare example of a physics breakthrough which immediately made a technological and commercial impact, the development of hard-disk read heads quickly followed the first discovery of giant tunneling magnetoresistance (TMR) in the 1980s[120,143]. In recent years, these devices have been utilized in a variety of new

applications such as probabilistic and neuromorphic computing[144,145]. MTJs have been and continue to be a fundamental building block of new and useful technologies. In the context of this thesis, we will find that they also provide a powerful platform for probing the basic magnetic properties of 2D magnetic insulators and semiconductors.

The operating principle for a magnetic tunnel junction is the spin-filtering effect[49,118,119,146-148]. Basic quantum mechanics tell us that the spin of an electron is conserved during tunneling. Consequently, electrons with a specific spin will have an easier time tunneling into a magnetic material with the same spin alignment. By the same argument, electrons with opposite spin will have a much lower tunneling rate. Therefore, the tunneling current in the parallel case will be much larger than the tunneling current in the anti-parallel case. This effect is known as giant TMR, and the two distinct magneto-resistive states are the "0"s and "1"s in standard binary magnetic memory (Fig. 3.2-1).

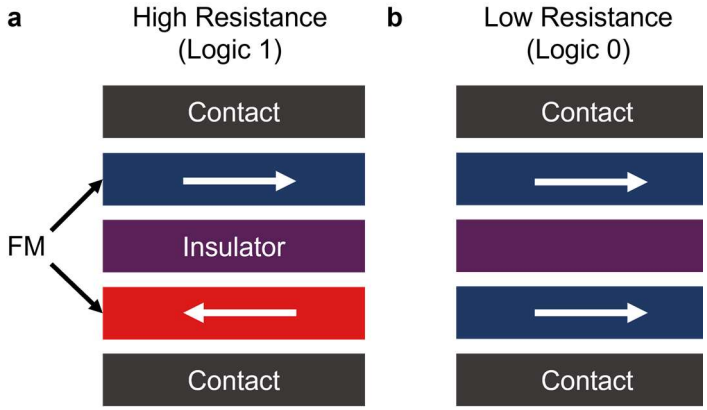

Figure 3.2-1 | Diagram of basic spin filter devices. When a voltage is applied between the contacts, the electrons will tunnel through the insulating barrier with some probability depending on the orientation of the magnetic layers. The tunneling resistance in the antiparallel state (**a**) will be much higher than the parallel one (**b**). These two distinct states form the basis for standard binary magnetic memory

The standard stack which is utilized in conventional MTJ devices requires the careful growth of many magnetic and insulating layers (Fig. 3.2-2a). Looking at the magnetic structure of the MTJ, however, we immediately notice similarities with the A-type antiferromagnetic order established in Chapter 2. Essentially, each AFM interface in the A-type AFMs can serve as an atomically sharp spin-filter, with the entire bilayer constituting a "spin valve" (Fig. 2.1-1b). We

can further leverage the capability to stack 2D materials in vdW heterostructures to create clean devices without any consideration for lattice matching. In standard all-vdW MTJs, the 2D magnet is typically sandwiched between graphite contacts which simply serve as metal contacts (Fig. 3.2-2b). Alternatively, the graphite contacts can be replaced with superconductors such as $NbSe_2$ to form magnetic Josephson junctions, and other novel devices which are still being explored.

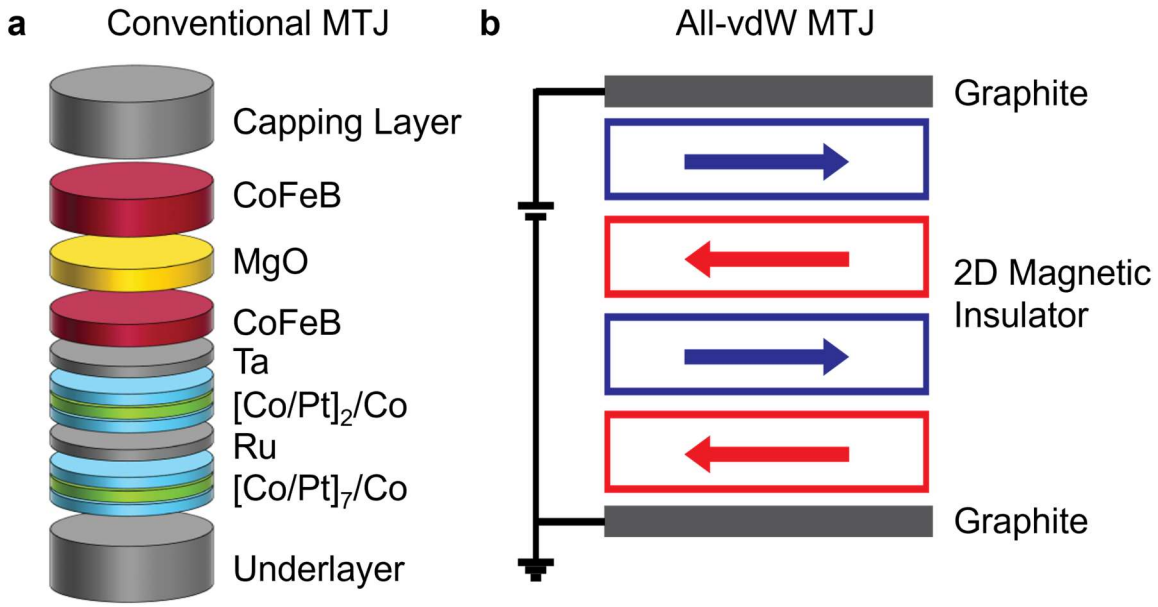

Figure 3.2-2 | Schematic of MTJ devices. **a,** Conventional MTJ device used in magnetic random access memory (MRAM) applications. These devices consist of several different layers with precise growth thickness and composition. **b,** Diagram of all-vdW MTJ devices. In such MTJs, the A-type AFM order in the 2D magnetic insulator or semiconductor is utilized as atomically sharp spin filters, and metallic graphite contacts are used to apply the voltage to the device. Panel **a** is adapted from Ref. [144]

Figure 3.2-3a shows the optical image of a completed bilayer CrSBr MTJ device. Narrow graphite contacts are selected so that they overlap less than ~ 1 μm^2 to limit domain effects. When a voltage is applied to the MTJ, electrons will tunnel from one graphite to the other with a characteristic nonlinear dependence on the bias voltage. Fig. 3.2-3b plots the bias dependent tunneling current at 0 T (blue) and a polarizing 1T (orange) applied along the easy *b* axis at a sample temperature of 2 K. The clear enhancement in electron tunneling is a result of the alignment

of the spins in both layers of the spin valve. As expected, the full magnetic field dependence of the tunneling current reveals a sharp spin-flip transition occurs when the field is swept along the *b* axis (Fig. 3.2-3c) with a TMR of ~ 63 %. It is worth noting that this value is significantly smaller[100,106] than that observed in bilayer CrI_3, with one potential cause being that semiconducting CrSBr is far less insulating.

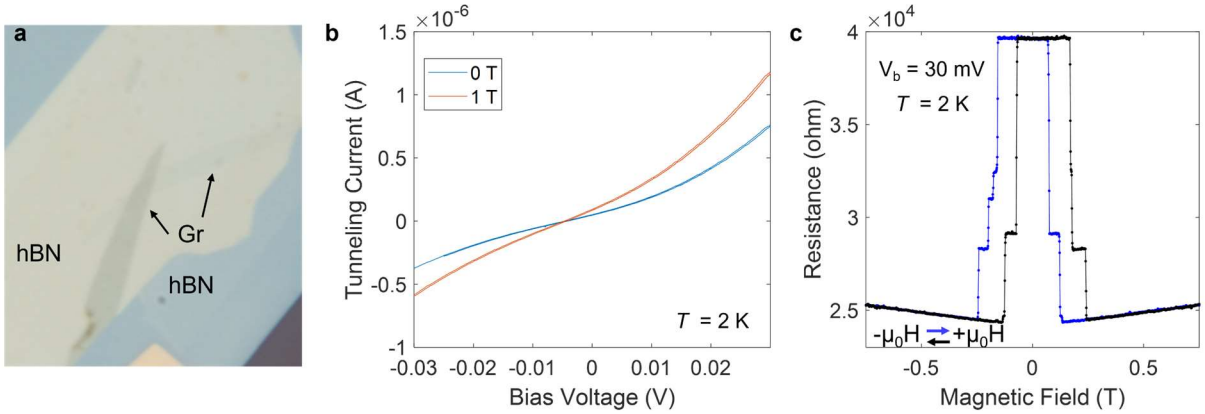

Figure 3.2-3 | Bilayer CrSBr magnetic tunnel junction. **a,** Optical image of the MTJ device. A bilayer CrSBr is sandwiched between graphite contacts to form the MTJ. Then, the MTJ is further encapsulated in hBN to protect it from the atmosphere and improve the surrounding dielectric environment of the device. **b,** Bias dependence of the tunneling current at 0 T (blue) and at a saturating field of 1 T (orange) applied along the *b* axis. **c**, Magnetic field dependent TMR with the magnetic field applied along the easy axis at a base temperature of 2 K and DC bias voltage of 30 mV.

Rotating the sample using the horizontal rotator again allows us to study the full angular dependence of the in-plane magnetic phase diagram. Figure 3.2-4a shows the color plot of the tunneling current versus magnetic field and rotator angle. The minimum critical field, which corresponds to a sharp spin flip transition, occurs at around ~55°. When the angle is deviated from this value, the transition becomes more gradual with and the spin-polarizing field (i.e., the point where the tunneling current ceases to evolve) becomes larger until the angle reaches ~145°. Figure 3.2-4b shows linecuts at these two angles demonstrating the gradual spin canting process when the

field is applied along the *a* axis (i.e., ~145°) in comparison to the sharp spin-flip transition when the field is along *b* (i.e., 55°).

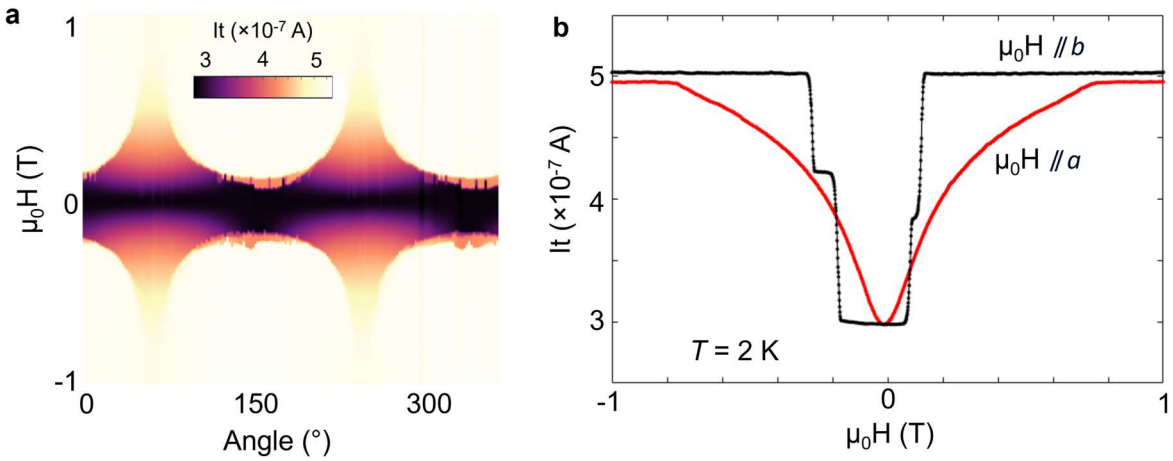

Figure 3.2-4 | Angular magnetic field dependence of tunneling magnetoresistance in bilayer CrSBr **a,** Full angular dependent TMR sweeps of the MTJ device. **b,** Line cuts at selected angles demonstrating sharp spin-flip behavior when the field is aligned with easy *b* axis (black, 145°) and continuous spin canting when the field is along the intermediate *a* axis (red, 55°). These data were taken at a base temperature of ~ 2 K and an AC bias of 20 mV.

Another feature which stands out in the above field dependence is the additional jump in the tunneling magnetoresistance observed when the field is applied along the *b* axis (Figure 3.2-4b). This behavior begins at temperatures below ~ 45 K and could be due to magnetic domain effects arising from a spatially inhomogeneous sample. However, it is worth noting that the secondary magnetic phase transition corresponding to the ordering of defect spins has been reported to onset at ~ 40 K[62,128]. Further exploration and additional devices are required to confidently determine the origin of this two-jump magnetic domain behavior.

In the wider context of vdW MTJs, CrSBr has the major advantages of being relatively air-stable in multilayers, and operating to higher temperatures than many other 2D AFMs, e.g., CrI_3, which requires temperatures below ~ 45 K. On the other hand, bilayer CrSBr MTJs have much lower TMR than bilayer CrI_3. The weak TMR can be significantly enhanced by using more layers of CrSBr (i.e., thicker flakes) in the MTJ since each additional AFM interface acts as a

spin filter. We will see in Chapter 6 that MTJs which utilize thin bulk (~ 11 nm) CrSBr result in dramatically larger TMR ratios of several thousand percent, and that these individual spin filters can actually be controlled through strain.

The results of this chapter and the previous one has demonstrated that the coupling of spin and charge dominates a wide range of electronic properties in CrSBr, from the exciton wavefunction to the magnetoresistance. Therefore, any control knob which tunes the magnetic order will also provide control over the electronic properties as well. Fortunately, the layered nature of CrSBr enables us to open the wide toolbox of tuning methods which have been developed by the field. For the rest of this thesis, we will focus on the specific control knob of tensile strain. Remarkably, we found that CrSBr is an ideal material for strain experiments in comparison to other traditional vdW materials due to its crystal structure. Moreover, strain dramatically modifies the interlayer magnetic exchange and magnetic order, which leaves unambiguous signatures in the optical and electronic properties of the system. Consequently, the spin-charge-lattice coupling in this material provides a fruitful platform for studying tunable 2D magnetism for fundamental physics and device applications alike.

Chapter 4. STRAIN TUNING OF 2D MATERIALS

In this chapter, we will describe techniques used to apply large strains to atomically thin materials. By adapting a piezoelectric strain cell typically used for bulk crystals[149], we were able to successfully apply strains exceeding 1.5 % at cryogenic temperatures to both suspended and supported 2D crystals. Many of the results of this chapter come from manuscripts which are currently in preparation. However, the development of the strain cell and suspended and polyimide techniques can be found in *J. Cenker et al.* "Reversible strain-induced magnetic phase transition in a vdW magnet" and *G. M. Diederich, J. Cenker, Y. Ren, et al.* "Tunable interaction between excitons and hybridized magnons in a layered semiconductor", both of which were published[48,74] in *Nature Nanotechnology*.

4.1 STRAIN TUNING OF 2D MATERIALS: EXPERIMENTAL TECHNIQUES

Mechanical deformation, i.e., strain, is a powerful method for tuning the properties of quantum materials. Examples include the strain control of superconducting[32,150], nematic[151], and topological[29] phases. When stretched, crystals tend to break at dislocations and defects in the crystal lattice, which tends to limit the maximum sustainable tensile strain to < 1 % in bulk crystals. Shortly after the discovery of monolayer graphene, it was realized that the pristine, single-atom thick carbon sheets have exceptionally small defect density and are capable of surviving ~ 10 % strain, making it the strongest material ever discovered[36]. However, the atomically thin nature of these materials and devices poses significant practical challenges towards utilizing them in conventional strain cells, especially at cryogenic temperatures where many quantum phenomena can emerge.

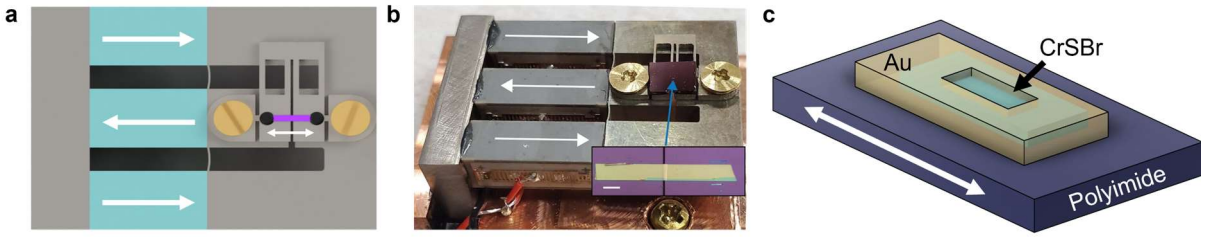

Figure 4.1-1 | Strain cell and techniques. **a,** Schematic of the symmetric piezoelectric strain cell. Applying a positive voltage to the cell causes the piezo stacks to move according to the direction of the white arrows: the outer ones expand, while the inner one contracts. The result is an increasing size of the gap (white arrow below purple rectangle) and application of tensile strain to the sample. The grey flexure plate which is screwed onto the cell enables convenient sample fabrication and mounting. **b,** Optical image of the strain cell with a thin bulk 2D material mounted across a thin silicon gap. Scale bar: 30 μm. **c**, Depiction of a polyimide mounted sample. Here, the CrSBr is deposited onto the polyimide substrate and a gold fastener is evaporated on top. The choice of whether to use the gold or not depends on the experiment (see Chapters 4, 6). Panel **b** adapted from Ref.[74]

To perform in-situ strain measurements, we adapted a piezoelectric strain cell design (Fig. 4.1a) which has been extensively used to study bulk quantum materials[149]. When a voltage is applied to the strain cell, the outer piezos will extend, and the inner one will contract, opening the gap and applying a tensile strain to anything glued across it. Because 2D crystals are too small and hard to handle using conventional means, they cannot be attached directly to the rough titanium strain cell. To overcome this challenge, we devised a way to make small (5 μm) gaps in silicon substrates. This small gap is formed by first gluing a thin silicon substrate to the strain cell, and then fracturing it with a diamond scribe. The resulting fracture tends to be ~ 5 μm in size, quite height uniform, smooth, and residue-free (Fig. 4.1-1b and Appendix II). The main advantage of this technique is that the small gap is potentially capable of generating exceptionally large strain, defined as $\varepsilon = \frac{\Delta L}{L}$, since the displacement of the piezos (ΔL) is comparable to the gap size (ΔL). However, the suspended technique comes with some disadvantages: the strain can be inhomogeneous, and there are significant fabrication challenges for monolayers and devices.

The need for more universal and robust strain device fabrication led us to utilize strain transfer from a flexible substrate (Fig. 4.1-1c) as the main platform for strain devices. We utilized thin silicon and polyimide substrates as the foundation for the heterostructures, with the latter allowing for exceptionally large strains even at cryogenic temperatures[152]. Fortunately, the fabrication of these samples can be achieved through relatively straightforward modifications of standard, silicon-based devices (Appendix II). Although flexible substrate-based strain devices have been used to strain 2D materials for many years[39,153-155], the maximum in-situ strain tuning range achieved in vdW heterostructures[38] and devices has struggled to exceed 0.5%. To understand and overcome this challenge, we investigated strain transmission in a wide range of vdW materials, starting with the layered magnetic semiconductor CrSBr.

4.2 Calibration of strain in 2D materials and heterostructures

The standard probes of strain in 2D materials include Raman spectroscopy and photoluminescence measurements which measure the phonon energy and band structure, respectively. However, the accurate measurement and calibration of strain is a general challenge common to many in-situ strain tuning experiments. For instance, the reported PL energy shift as a function of strain in monolayer semiconductors varies widely throughout the literature[156-159]. To ensure accurate calibration of the strain applied to the CrSBr sample, we systematically characterized the strain response of its phonon modes using Raman spectroscopy.

First, we assembled a strain gauge heterostructure consisting of a hBN flake stacked on top of both graphene and thin bulk CrSBr deposited on a thin silicon substrate (Fig. 4.2-1a). To apply strain to the sample, the effective spring constant of the material glued across the gap must be less than the stiffness of the piezostacks themselves (otherwise the gap will not open when a voltage is applied). This effective spring constant can be calculated by:

$$k_{eff} = \frac{Y * A}{L}$$

where Y is the Young's Modulus, A is the cross-sectional area, and L is the length of the glued substrate. Considering the large Youngs modulus of silicon[160], the thin silicon substrate must be cut extremely narrow, normally 200 to 300 μm and glued with a gap of a few hundred μm. Finite element simulations shown in Figure 4.2-1b demonstrate that when a piezo voltage is applied with these parameters, the strain over the gap region is highly uniform on the length scale of the 2D materials and especially the beam spot (~ 1 μm). Figure 2.4-1b shows the Raman spectra of the CrSBr in the strain gauge heterostructure, consisting of three prominent peaks. The Raman peak

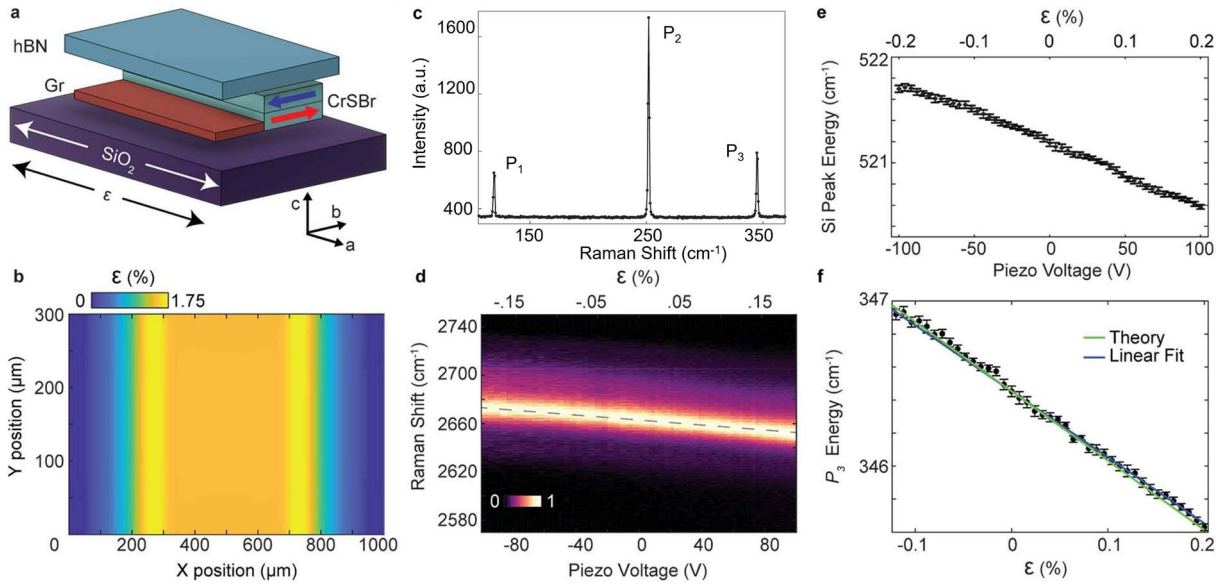

Figure 4.2-1 | Calibrating strain using Raman spectroscopy. **a,** Schematic of a strain gauge heterostructure. Hexagonal boron nitride is used to pick up graphene and CrSBr and is then deposited on a thin silicon substrate. The strain is applied along the CrSBr *a* axis. **b,** Finite element analysis of the strain profile across the narrow thin silicon substrate. **c,** Raman spectra of bulk CrSBr at zero strain. The spectrum consists of three dominant peaks. **d,** Measurement of the graphene 2D mode as a function of piezo voltage, showing a linear redshift with increasing tensile strain. The strain values on the top of the axes are then calculated using a previously reported shift rate. **e,** Measured strain as a function of piezo voltage obtained by applying the same methodology as **d**, but to the silicon Raman peak centered at ~ 520 cm^{-1}. **f,** Energy of P_3 as a function of strain plotted alongside linear fits to the data (blue line) and the Raman shift rate obtained from the first-principles calculation (green line, shifted vertically to ~ 346 cm^{-1} at $\varepsilon = 0$). The error bars in **e-f** represent the uncertainty of the Lorentzian fits used to extract the peak center. Reproduced from Ref. [74]

which shifts most with strain is centered around ~ 346 cm^{-1} at 0 % strain and is hereafter labeled as P_3. When a voltage is applied to the strain cell, the 2D mode in graphene (Fig. 4.2-1d) and phonon mode in silicon (Fig. 4.2-1e) begin to red-shift. Comparing the measured shift rate with the literature strain-shift rates for the 2D mode in graphene[38,161] and the silicon peak[162] enables us to accurately determine the strain applied to the sample. Based on this calibration, we find that P_3 shifts at a rate of ~ 4.2 cm^{-1}/% (Fig. 4.2-1f). This value is close to the value of 4.4 cm^{-1}/% predicted by first principles calculations (green line in Figure 4.2-1f).

It is important to note that the most sensitive and appropriate method of measuring strain depends highly on the material system of interest. For instance, the monolayer semiconducting TMDCs and other semiconducting systems such as InSe have exceptionally large changes to the band gap under strain[155,158], and certain metals can have large elastoresistance[151]. However, we found that Raman works best in the case of CrSBr due to the relatively large strain shift of the P_3 phonon mode, and the very small change in band gap (until the magnetic phase transition detailed in Chapter 5). Regardless of the method chosen, care must be taken to calibrate the strain during the experiment since the amount of *transmitted* strain can be much smaller than the expected value applied by the strain cell. The strain gauge heterostructure reported above provides a versatile platform for universally calibrating the strain response of a variety of systems. Moreover, the silicon substrate can provide a much cleaner environment for sensitive devices than the polyimide substrates we will utilize for the rest of this thesis, at the drawback of a very limited strain range (less than ~ 0.5 % total).

4.3 Unity Strain Transmission in CrSBr

The careful determination of the strain applied to the sample enables us to study the strain transmission properties in CrSBr. An interesting observation in Fig. 4.2-1f is that the strain shift

matches the theoretical prediction for monolayers despite the sample being multi-layered. This behavior is distinct from that of graphite where the strain-dependent Raman shift quickly drops to zero in thin bulk samples[41].

To test the limits of the strain transmission, we studied flakes up to the thick bulk limit (> 100 nm, Fig. 4.3-1a) on polyimide substrates which permit the application of exceptionally large strains. Figure 4.3-1b shows the colormap of Raman intensity as a function of piezo voltage for bulk CrSBr transferred onto polyimide. Converting the measured Raman shift to strain reveals a continuous shift up to ~ 1.6%. Notably, the full width at half maximum of the peak is constant during the strain sweep, demonstrating that the strain is rather homogeneous through the sample. Remarkably, the CrSBr flakes exhibit robust strain tuning up to ~3.4 % at a temperature of 40 K (Fig. 4.3.1-c). The observation of such extreme strains in a vdW material at cryogenic temperatures

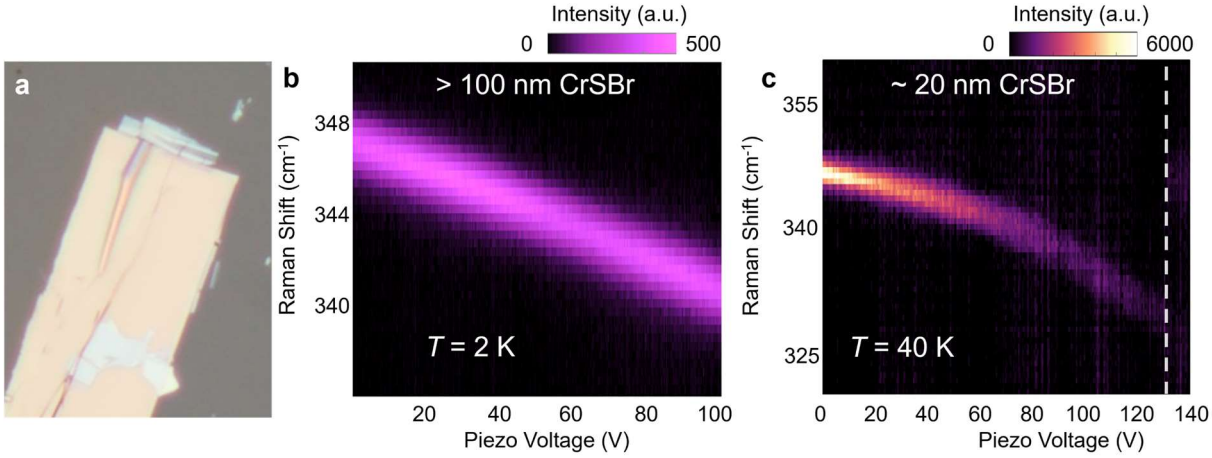

Figure 4.3-1 | Unity Strain transmission in CrSBr. **a,** Optical image of a bulk (> 100 nm) CrSBr flake deposited on the flexible polyimide substrate. **b,** Intensity plot of P_3 as a function of piezo voltage for the unclamped thick bulk flake shown in **a** at a base temperature of ~ 2 K. **c,** Raman color map as a function of piezo voltage for a thin bulk (~ 20 nm) CrSBr flake at a temperature of ~ 40 K. At this temperature, the strain cell can generate substantially more strain due to the temperature-dependent efficiency of the piezostacks. The sample shows robust strain behavior up to a strain of ~ 3.4 %, at which point the sample slips (grey line).

opens new doors for in-situ control of material properties through direct modification of lattice constants, bond geometries, symmetries, etc.

4.4 PROBING STRAIN TRANSMISSION IN HEXAGONAL 2D MATERIALS

In addition to enabling the exploration of extreme strain effects in a magnetic semiconductor, the unity strain transmission in CrSBr has the additional practical advantage of serving as a convenient strain sensor. That is, placing CrSBr flakes of arbitrary thickness on other materials enables accurate measurement of strain on the surface of those materials, loosening the strict mono- or few-layer limit needed to sense strain using materials like graphene. In this chapter, we will utilize this tool to characterize strain transmission through vdW crystals and heterostructures.

Figure 4.4-1a shows an optical image of a strain device with both CrSBr deposited directly on polyimide, and with CrSBr stacked on top of hBN on top of polyimide. Since the samples are close to each other and on the same polyimide substrate, they should experience very similar

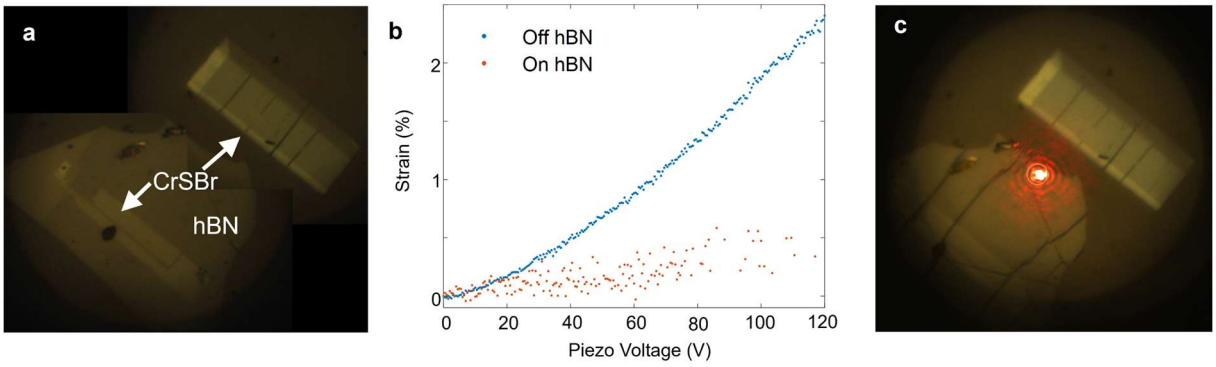

Figure 4.4-1 | Sensing strain transmission through CrSBr and hBN. **a,** Optical image of the sample consisting of two thin bulk CrSBrs, with one stacked on top of thin bulk hBN (bottom left) and one directly on polyimide (upper right). The close proximity of the flakes ensures that they should have similar strain environments. **b,** Strain on (orange) and off (blue) the hBN determined using the Raman strain calibration procedure. **c,** Optical images of the flakes with the piezos swept down to 0 V after the application of 120 V. The hBN develops severe new wrinkles, while the CrSBr flake remains unchanged, demonstrating the differential strain transmission between the two materials.

strain when the load is applied. However, using the calibrated response of the P_3 Raman peak on both samples reveals dramatically different strain response: at high piezo voltage, the directly deposited CrSBr experiences ~ 4-5x higher strain than the flake stacked on hBN (Fig. 4.4-1b). The inefficient strain transfer is further confirmed by the optical images: the hBN flake shows a large number of newly developed wrinkles, while the CrSBr shows no new wrinkles beyond the ones which occurred during fabrication (Fig. 4.4-1c). These observations strongly suggest that CrSBr and hBN have exceptionally strong and weak strain transmission, respectively.

To understand the dramatic difference in performance between these materials, we must first understand the failure and slipping mechanism in 2D materials. Examining the crystal structure of these materials (Fig. 4.4-2) already provides an intuitive picture: taking hBN as an example, the bonds between carbon and nitrogen atoms are entirely within each layer without much protrusion along the *c* axis. Moreover, there exist two possible stacking orientations which are close in energy. These two properties result in extremely weak interlayer strain transmission, and a tendency for soliton, i.e., atomically sharp wrinkles due to interlayer slipping, formation[43,44].

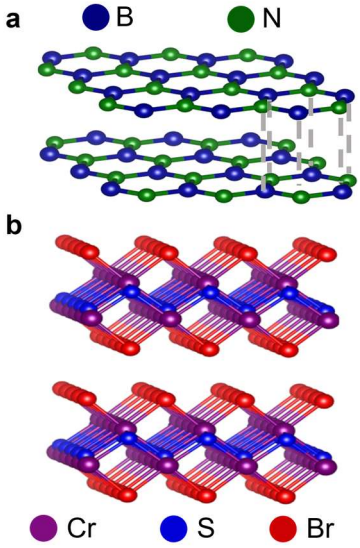

Figure 4.4-2 | Crystal structures of bilayer hBN (**a**) and CrSBr (**b**).

In contrast to graphite and hBN, CrSBr has hook-like bromine bonds which protrude along the *c* axis (Fig. 4.4-2b) and has an orthorhombic crystal structure with only a single stable stacking configuration. Consequently, the interlayer strain transmission and maximum sustainable strain in multilayers is apparently remarkably high. To test whether the robust strain performance is maintained in crystals with structural similarity to CrSBr, we measured the strain transmission in

materials with orthorhombic crystal structures, specifically α-MoO_3, which has a very similar anisotropic structure to CrSBr, and Bi_2SeO_5 (See Fig. 4.4-3a for crystal structures). We confirmed efficient interlayer strain transmission in these crystals by measuring the strain-dependent Raman shift of a thin bulk CrSBr stacked on top of thin bulk (>20 nm) α-MoO_3 and Bi_2SeO_5 flakes (Fig. 4.4-3b).

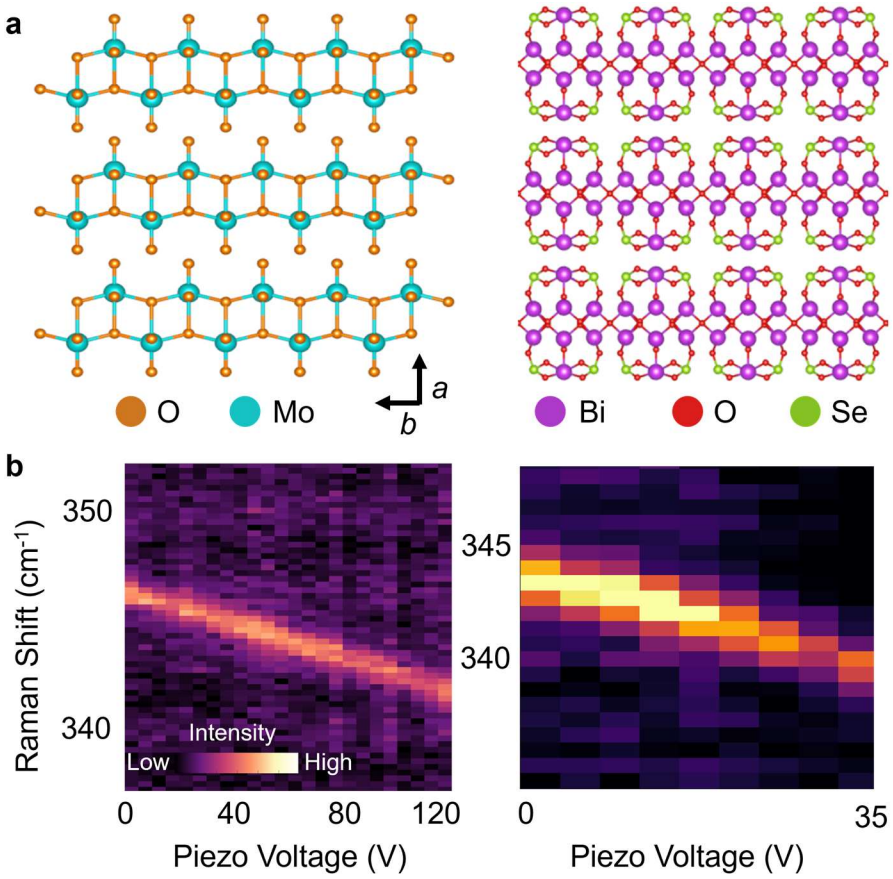

Figure 4.4-3 | Probing strain transmission in other orthorhombic crystals. **a,b,** Crystal structures of α-MoO_3 (left) and Bi_2SeO_5 (right) as viewed from the side. **b,** Intensity plot of P_3 as a function of piezo voltage for a CrSBr strain sensor stacked on top of thin bulk α-MoO_3 (left) and Bi_2SeO_5 (right). The continuous and large linear shift indicate efficient strain transmission through the substrate (i.e., α-MoO_3 and Bi_2SeO_5 layers). Both measurements were taken at a nominal sample temperature of ~ 5 K.

It is important to note that strain is transmitted well through various orthorhombic layered crystals. The wide variety of materials recently discovered in this category including magnets[61,68]

and dielectrics[163,164] can serve as the building blocks in strain-tuned vdW heterostructures and devices.

4.5 Bi_2SeO_5: AN IDEAL STRAINTRONIC DIELECTRIC

The substrate upon which an atomically thin material is placed plays a vital role in the sample quality since the flake will conform to the surface. For instance, the electrical properties of graphene can be greatly enhanced by placing it on atomically smooth hBN substrates which screen out the surface charges and roughness present on standard silicon substrates[165]. In recent years, hBN usage has become even more important and ubiquitous, especially in fragile moiré metamaterials formed by stacking monolayers with a twist or lattice mismatch, and air-sensitive materials where hBN encapsulation protects the embedded flake from the environment. Consequently, the dismal strain transmission explored in the previous section poses significant challenges to the study of strain effects in a variety of systems.

The recently synthesized[164] layered dielectric material Bi_2SeO_5 studied in the previous section may provide a promising path forward. To explore whether this material can serve as a substrate for high-quality strain-controlled devices, we used standard device fabrication procedures to construct a top-gated WS_2 device (Fig. 4.5-1a). Specifically, we transferred ~ 30-50 nm thick Bi_2SeO_5 flakes onto the polyimide substrate, evaporated platinum contacts, and then cleaned the platinum and nearby area using contact mode on an atomic force microscope (AFM), a technique known as AFM cleaning[166]. This technique can clean even extremely dirty substrates, providing a pristine and atomically flat surface to build the device on (see Fig. 4.5-1b,c for example on dirty Hall bar contacts). Then, a hBN top gate was used to pick up a monolayer WS_2 flake and the entire stack was deposited onto the Bi_2SeO_5 substrate (See Fig. 4.5-1d for completed device image).

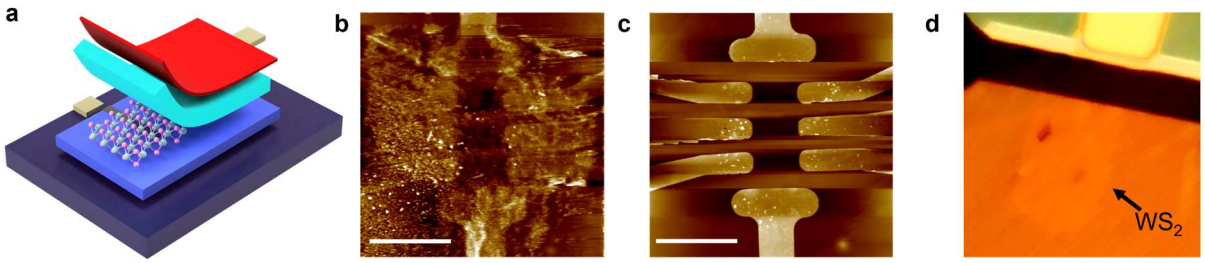

Figure 4.5-1 | High quality strain device fabrication using Bi_2SeO_5 dielectric substrates**. a,** Schematic of the high quality top gated TMDC device. For these samples, thin bulk Bi_2SeO_5 is used as the bottom dielectric substrate, with a platinum contact evaporated on top. Then, a top gate consisting of graphite (red) and hBN (cyan) are used to pick up and stack a monolayer onto the Bi_2SeO_5 to form the heterostructure. **b, c,** Contact mode AFM scans before (**b**) and after (**c**) several rounds of AFM cleaning. Scale bar: 5 µm. **d,** Optical image of the finished gated monolayer WS_2 device.

Figure 4.5.2 shows the spectra of the WS_2 monolayer at large negative and positive gate voltages. Based on previous reports[167], we identify the different excitonic species at a large negative gate voltage, which is closest to charge neutrality, as the neutral exciton (X_0) , biexciton (XX), and trion (X^-). When electrons are doped into the system, the second charged state of the trion, X^{--}, dominates the spectrum (7.3 V, black line in Fig. 4.5.2). The gate tunability of the exciton species indicates negligible charge transfer and defect states from the Bi_2SeO_5 substrate, while the narrow linewidth indicates the high quality of the device. The observed linewidth is slightly broader

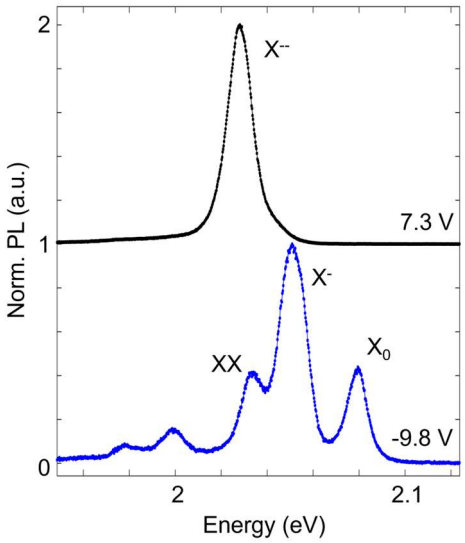

Figure 4.5-2 | Gate dependent photoluminescence spectra of monolayer WS_2. The piezo voltage is 0 V, and the temperature is nominally 5 K.

than comparable hBN devices[167,168], though it is worth noting that the sample temperature may have a significant offset[169] and therefore be higher than the nominal temperature of ~ 5 K.

The most important figure of merit for Bi_2SeO_5 as a building block for strain devices is the maximum transferrable strain. Figure 4.5-3a -b show the strain-dependence of the exciton species at negative and positive gate voltages, respectively, showing large and continuous strain tuning. In addition, the peak energy shift is highly reversible with strain, indicating robust strain transmission and negligible slippage. This is illustrated by extracting the energy shift of X^- with a Gaussian fit and plotting it as a function of piezo voltage which is swept up and down (Fig. 4.5-3c). In addition to tuning the exciton energy, strain can break the C_3 symmetry of the crystal lattice (see inset of Fig. 4.5-3d), which can have consequences on valley polarization. Indeed, the degree of circular polarization, defined as $\mathrm{DOCP} = \frac{\sigma^+ - \sigma^-}{\sigma^+ + \sigma^-}$ with σ^+ (σ^+) corresponding to right (left) circularly polarized light, respectively, decreases with increasing strain (see Fig. 4.5-3d for X^-). This quantity is related to the valley polarization, but it is worth noting that several effects of strain can be responsible for the decrease in DOCP, such as decreasing the energy between K and Γ valleys and the relaxation of selection rules due to the large uniaxial strain, and disentangling such effects[170,171] is left for future efforts. For both X^- and X^0, we observed a redshift of ~ 80 meV between the lowest and largest strains. By using the previous literature reports[156] of ~ 43 meV/% for the X^0 strain shift rate in monolayer WS2, we find that a large strain approaching ~ 1.8 % is applied to the sample. We again note that there are a wide range of reported shift rates, which is the largest uncertainty in the measurement. However, regardless of small differences in the calibration, this device demonstrated an order of magnitude greater strain range than previous gated strain samples at cryogenic temperature, proving that Bi_2SeO_5 is a promising substrate for these experiments in comparison to hBN.

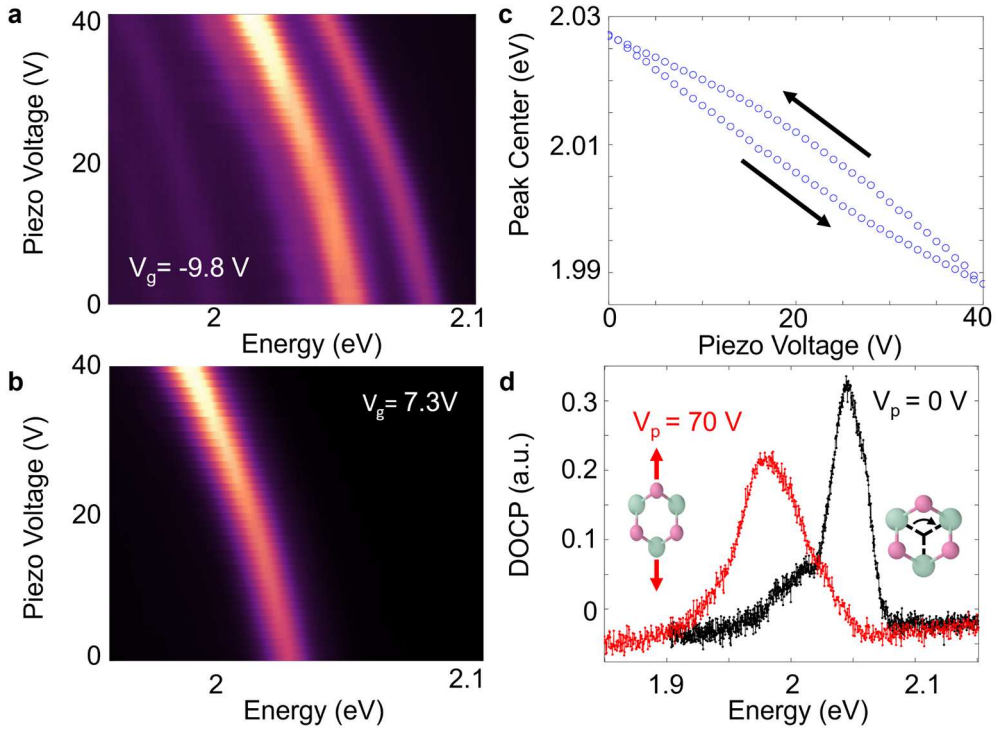

Figure 4.5-3 | Strain and gate tuning of monolayer WS_2. **a,b,** Intensity plot of photoluminescence as a function of piezo voltage when the sample is at large negative (**a**) and positive (**b**) gate voltages. Both conditions show a large and continuous tuning when the piezo voltage is increased, and strain is applied to the sample. **c,** Fitted X^{-} (i.e., the peak in **b**) peak center as the piezo voltage is increased and then decreased. The peak energy returns to exactly the same value indicating no slippage. The observed hysteresis is typical for the piezoelectric strain cell. **d,** Degree of circular polarization of X^{-} at a piezo voltage of 0 V (black) and 70 V (red). The breaking of the C_3 rotational symmetry which is present in pristine monolayer WS_2 is depicted in the inset.

4.6 Future Directions

This chapter has demonstrated the possibility of applying large strains to atomically thin materials and heterostructures in conditions sufficient for quantum phenomena to emerge. Spurred by the surprising discovery of remarkably efficient strain transfer in unclamped CrSBr samples, we examined the strain transmission in a variety of materials. Notably, we established Bi_2SeO_5 as a promising dielectric platform for high-quality devices. These results will enable the application of strain to a variety of new systems such as moiré heterostructures[16] and air-sensitive

superconductors[25,172] and magnets[169]. Indeed, our preliminary results indicate that Bi_2SeO_5 devices can serve as suitable substrates for moiré samples. Figure 4.6-1a shows the piezo-force microscopy (PFM) of a nearly aligned WSe_2/WS_2 heterostructure. A clear moiré pattern existing over > 200 nm of the sample is observed.

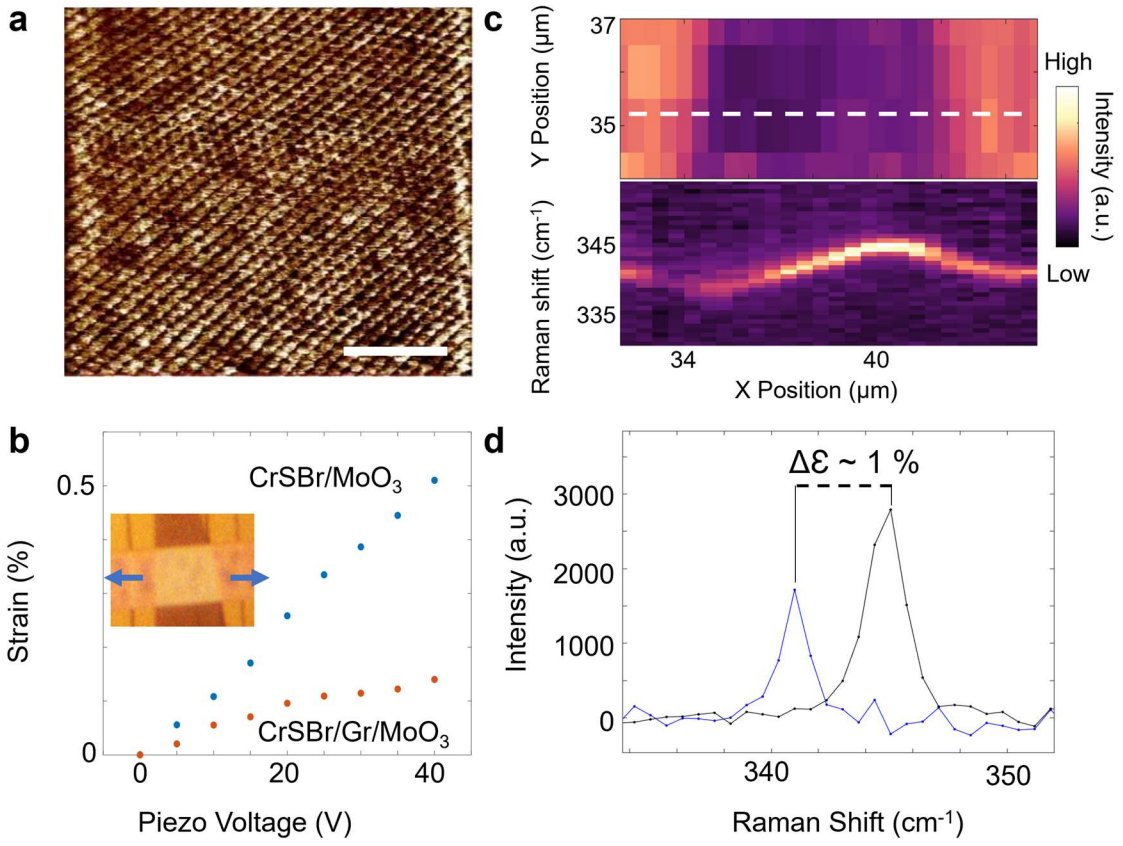

Figure 4.6-1 | New types of strain devices. **a,** Piezo-force microscopy image of a moiré pattern formed in a WSe_2/WS_2 heterostructure. The moiré period is ~ 8 nm, indicating a near-0° sample. Scale bar**:** 50 nm. **b,** Strain measured using the CrSBr Raman response on and off a graphite flake. An optical image of the sample is shown inset. **c,** Spatial map of the intensity of the Raman spectra across the sample (top). The low intensity region corresponds to the graphite flake. A linecut across the grey line is shown in the bottom panel, showing a continuously varying P_3 energy. **d,** Raman spectra comparing the highest and lowest strains shows a strain gradient of ~ 1 % across a distance of ~ 5 μm.

In addition to the application of large, homogeneous strains in high-quality devices, the results of this chapter may be applied to engineer spatially varying strain profiles, i.e., strain gradients, using the strain screening from materials such as hBN and graphite. Figure 4.6-1b inset

shows the optical image of one such strain gradient heterostructure, consisting of CrSBr stacked on top of a graphite strip and a large bottom α-MoO_3. Using the P_3 Raman peak as a strain sensor, we find that the region of CrSBr that is stacked on top of graphite strains significantly less than the part which is only on top of α-MoO_3 (Figure 4.6-1b). To understand the strain profile across the sample, we performed spatial mapping of the Raman spectra. Figure 4.6.1c top shows a mapping of the Raman spectra intensity across the sample. The regions where the CrSBr overlaps with graphite have lower intensity due to the strong absorption of light by the graphite, among other potential effects such as charge transfer. Taking a linecut of the Raman spectra across the graphite reveals a smoothly varying peak energy (Figure 4.6.1c bottom) across the heterostructure. Plotting the individual spectra with high and low strains reveals a strain gradient approaching ~ 1 % over ~ 5 μm. Such strain gradients can be used to generate pseudomagnetic fields[173,174], exciton funneling effects[175], and perhaps spin textures due to the varying coercive field or magnetic state (see Chapter 5).

The goal is then to find interesting systems which are highly tunable with strain. Fortunately, we found that CrSBr, which has the best strain transmission and highest strain tolerance of any crystal we tested, is one such system. In addition to its remarkable mechanical properties, the sensitivity of the fragile AFM order to the bond geometry and the diversity optical and electrical probes makes CrSBr a particularly enticing material to strain.

Chapter 5. STRAIN TUNED MAGNETISM IN CRSBR

In Chapter 2, we established that the geometry of the bond angles is directly responsible for the magnetic order in CrSBr. Moreover, we learned that the dominant next nearest neighbor intralayer exchange terms were all FM, while the interlayer AFM order appears to be a delicate balance of FM and AFM contributions. Such systems could be highly sensitive to strain given the geometric origin of the interlayer exchange and the small energy difference between the AFM and FM states. Combined with the excellent strain transmission we found in Chapter 4, these properties make CrSBr an excellent platform for studying spin-charge-lattice coupling in a highly tunable magnetic semiconductor.

In this chapter, we will explore the effects of strain on magnetism in CrSBr using the exciton sensing probes developed in Chapter 2. These results were reported in the following works: *J. Cenker, et al.* "Reversible Strain-induced magnetic phase transition in a van der Waals magnet", *G. M. Diederich, J. Cenker, Y. Ren, et al.* "Tunable interaction between excitons and hybridized magnons in a layered semiconductor", and *J. Cenker, et al.* "Probing and controlling magnetism in 2D magnetic semiconductor CrSBr", published[48,74,176] in *Nature Nano, Nature Nano*, and *Proceedings of SPIE Spintronics*, respectively.

5.1 STRAIN DEPENDENT MAGNETO-PHOTOLUMINESCENCE OF CRSBR

The magnetic field-dependence of pristine bilayer CrSBr photoluminescence was established in Chapter 2. When the thickness of the sample is increased, additional exciton lines appear, as shown for the ~20 nm flake in Fig 5.1-1a. It is worth noting that the origin of these peaks is not yet established. This is perhaps a consequence of the recency of the discovery of atomically thin CrSBr. In fact, the accurate assignment of exciton peaks in other 2D semiconductors is still a topic of active debate and research despite over a decade of study[177,178]. Some origin of exciton species in those systems include defect-bound excitons, trion species, phonon relicas, exciton-polaritons, etc. The accurate identification of every exciton peak is not the center of the focus in this thesis. The important observation for our purposes is that all the exciton peaks within the spectral window exhibit the magneto-exciton coupling we established in the bilayer. For instance, when the magnetic field is applied along the easy *b* axis, all the peaks have sharp spin flip transitions at a critical field of ~ 0.22 T (Fig 5.1-1b).

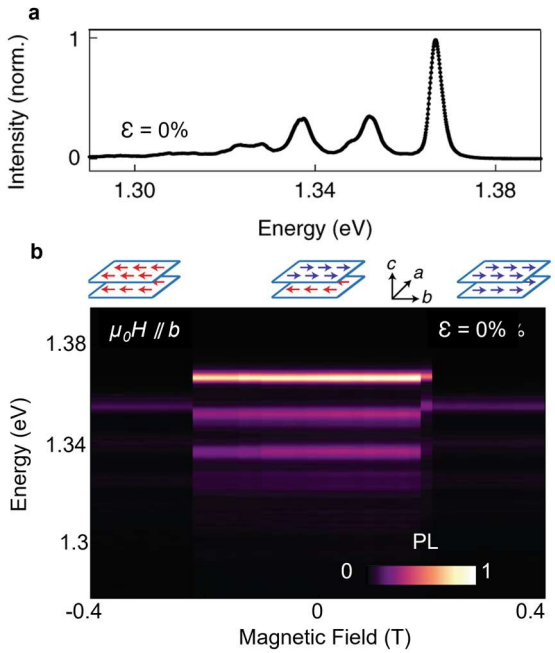

Figure 5.1-1 | Properties of the unstrained thin bulk CrSBr. **a,** Photoluminescence spectra of ~ 20 nm CrSBr have several additional features in comparison to the few layer limit. **b,** Magnetic field dependent measurements demonstrate that all peaks show the same magneto-exciton coupling as established in the bilayer. Adapted from Ref. [74]

To explore strain effects on CrSBr, we investigated both suspended and polyimide supported flakes, with consistent results regardless of strain technique. Figure 5.1-2a shows the PL

spectra of a suspended CrSBr sample as a strain is applied to the crystal's *a* axis. The strain is calibrated by comparing the Raman spectra taken on the strained region to the unstrained area far away from the gap. The main exciton peaks are essentially unchanged as the strain ramps from 0.7% to about 1.1%. Remarkably, as the strain increases past a critical point around ~ 1.3%, the entire spectrum suddenly changes. Past this point, the spectra again remained relatively unchanged with increasing strain. Figure 5.1-2b shows the PL spectra taken as the piezo voltage is swept up and down. Comparing the spectra at 0.7% and 1.5%, which correspond to before and after the abrupt change, respectively, reveals an similar PL pattern, but with a ~12 meV redshift between the low- and high-strain spectra. This shift is reversible, i.e., sweeping the strain back down to 0.7 % returns the spectra to its original state (Fig. 5.1-2d). Aside from the abrupt redshift, the minimal change in PL energy agrees with the first-principles calculation[74] which predict continuous, < 5

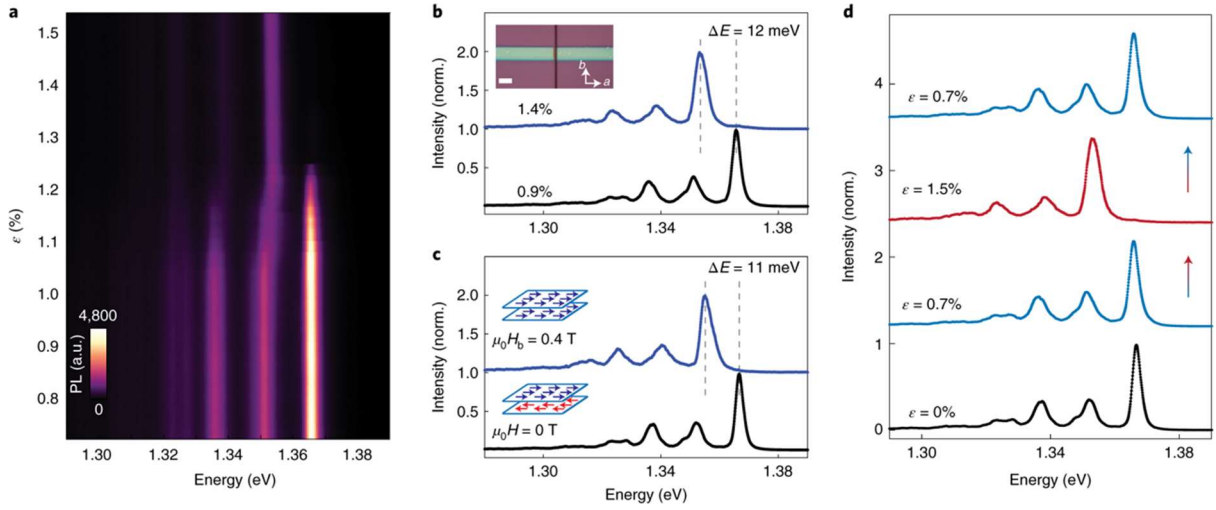

Figure 5.1-2 | Strain dependent photoluminescence measurements of a suspended thin bulk CrSBr sample. **a,** Plot showing the variation in photoluminescence intensity of the 20 nm CrSBr flake as strain is applied along the a axis, starting from approximately 0.7% strain. **b,** PL spectra at select strains of 0.9% (black) and 1.4% (blue). Inset displays an optical micrograph of the sample, with a scale bar of 30 μm. **c,** PL spectra at zero magnetic field (black) and with a 0.4 T field (red) applied along the *b* (easy) axis. Insets illustrate the A-type antiferromagnetic state at zero field, and the ferromagnetic state at high field. **d,** Sequential PL spectra as the strain is swept. The arrows indicate the strain progression: ramping up from 0.7% (bottom) to 1.5% (middle), then returning to 0.7% (top). All PL spectra are normalized and offset for clarity. Reproduced from Ref. [74]

meV change in band gap energy under this strain range, in stark contrast to other 2D semiconductors like the TMDCs[154]. The question is then what drives the large redshift between the low- and high- strain states.

The first hint that the strain-induced PL shift originates from a change to the magnetic order comes by comparing the effects of strain with that of an applied magnetic field. Figure 5.1-2c shows the PL spectra with magnetic fields of 0 T (black) and 0.4 T (blue) applied along the *b* (easy) axis. Since the applied field is larger than the spin-flip field, all of the spins are polarized, and the energy of the exciton is redshifted by ~ 11 meV due to the magneto-exciton coupling. Remarkably similar changes to the spectra, i.e., a red shift of ~ 12 meV is shown in the strain dependent data (Figure 5.1-2b). The slight discrepancy of ~ 1 meV between the strain and field-dependent exciton energy shifts could arise from the small modification of the bandgap from the large strain applied to the sample.

We further explored the strain-induced changes to the magnetic order by taking strain dependent magneto-PL measurements. Figure 5.1-3a,b shows magneto-PL measurements taken on a thin CrSBr flake deposited on polyimide with 0 V and 60 V applied to the strain cell, respectively. As with the previous measurement, the strain is applied along the crystal *a* axis, while the magnetic field is applied along the *b* axis and swept down from a positive value. The most obvious effect of strain in this range is to tune the critical field required for the spin-flip transition, with tensile strain serving to reduce the spin-flip field. Repeating the measurement at various piezo voltages reveals a linear dependence on strain, with an x intercept (i.e. piezo voltage) of ~ 91 V (Fig. 5.13c). The magneto-PL taken at strains higher than this value exhibit drastically different behavior, as shown in Figure 5.1-3d which was taken with 110 V applied to the strain cell. In this condition, the spectra remain invariant until a bright blip at a *negative* field spin-flip field, i.e., the

feature is now hysteretic with applied field. The observed hysteresis and characteristic energy shift observed above strongly suggests that a strain-induced AFM-to-FM phase transition occurs at high strain in CrSBr.

Additional confirmation of the strain-induced AFM to FM phase transition is found by

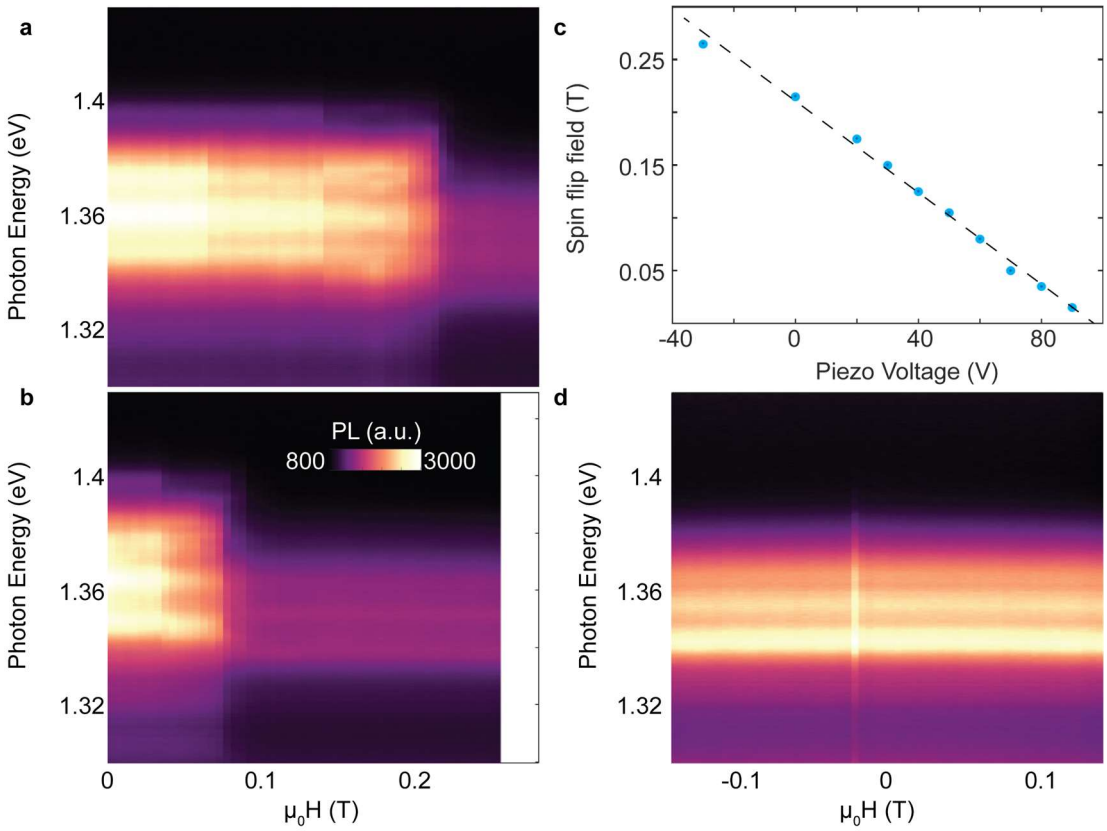

Figure 5.1-3 | Strain dependent magneto-PL measurements of thin bulk CrSBr. **a-b**, Magnetic field dependent photoluminescence taken with the magnetic field applied along the easy axis, with piezo voltages of 0 V **(a)** and 60 V (**b**). **c**, Spin flip field plotted as a function of piezo voltage. A linear fit of the data yields an x-intercept of ~ 91 V. **d**, Magneto-PL measurement taken at a large piezo voltage of 110 V. Sharp hysteresis is evident at the coercive field of the ferromagnetic (FM) state. The field is ramped from positive to negative. Adapted from Ref. [176]

taking magneto-PL measurements along the other axes. Figure 5.1-4 shows magneto-PL measurements of the suspended thin bulk CrSBr sample with the field applied along the intermediate *a* axis at strains of 0 %and 1.7 %, respectively. The unstrained spectra show the characteristic continuous spin-canting behavior. The high-strain state, however, has a completely

different field dependence, with no detectable energy shift with field. This is because the spins are always aligned regardless of the spin canting (see spin diagrams above the color maps) in the strain-induced FM phase. We should therefore expect no field-dependence in exciton energy at all. In this scenario, the only field dependence should occur near the coercive field along the easy axis, where magnetic domains containing layers with antiparallel orientations may form. This explains the hysteresis observed along the easy axis and the absence of field-dependence observed along the intermediate axis.

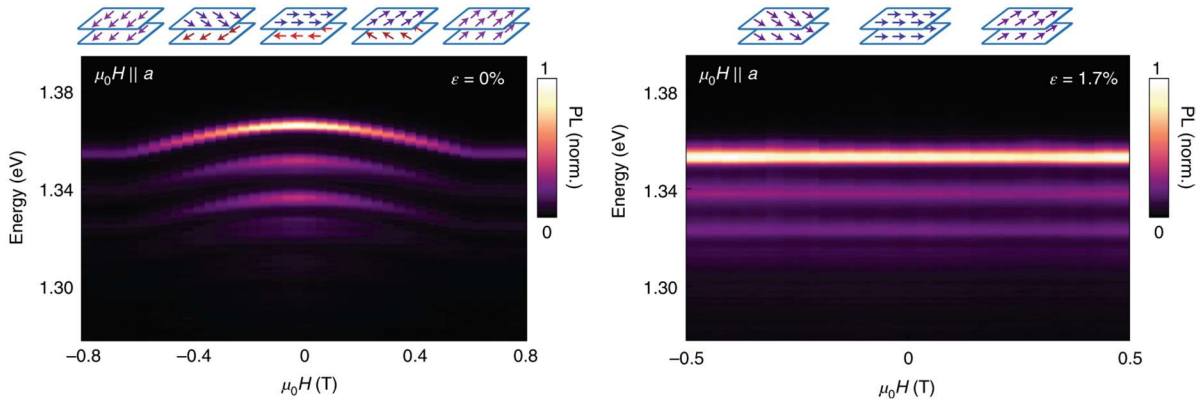

Figure 5.1-4 | Magneto-PL measurements along the *a* axis in the unstrained AFM (left) and high-strain FM (right) states. Adapted from Ref. [74]

5.2 THEORETICAL UNDERSTANDING OF THE STRAIN-INDUCED MAGNETIC PHASE TRANSITION

The experimental evidence for the magnetic phase transition is further supported by density functional theory (DFT) calculations which predict a strain-induced AFM to FM phase transition (see Fig. 5.2-1a). In addition to predicting the AFM to FM phase transition, these calculations help elucidate its origin. For instance, we observe little difference in the theoretically predicted critical strain when the other lattice parameters, i.e., *b* and *c* are either held constant or free to relax due to the Poisson effect. This indicates that changes to the interlayer spacing are not likely to play a role

in the changing magnetism. In addition, we find that there is only a single stable stacking order in CrSBr (see Fig. 5.2-1b). Therefore, we can rule out structural phase transitions which have been demonstrated[179,180] to drive an AFM to FM phase transition in pressurized atomically thin CrI_3. Rather, we find that the origin of the changing interlayer exchange in CrSBr comes from changes to the bond geometry due to the in-plane strain.

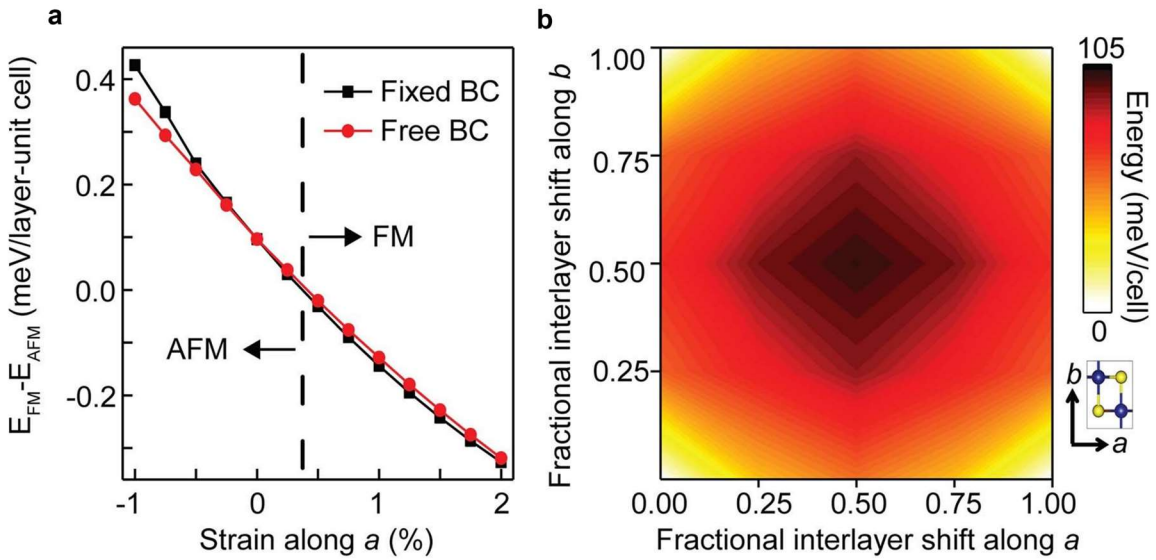

Figure 5.2-1 | DFT scalar-relativistic calculations of strain effects on interlayer magnetic ordering. **a,** DFT-LSDA calculated energy difference Δ between FM and AFM interlayer coupling as a function of uniaxial strain applied along the *a* axis. The switching from positive to negative with increased strain corresponds to a strain-induced AFM to FM transition, denoted by the dashed black line. We considered two cases, fixed- and free-boundary conditions, corresponding to whether the *b* and *c* lattice constants are either kept constant (black) or are allowed to relax (red). **b,** Stacking-dependent energy of AFM bilayer CrSBr calculated using a 4×4 grid to sample real-space shift vectors between layers. The results show that there is only a single stable interlayer stacking configuration at (0, 0). Adapted from Ref. [74]

According to the calculations, the largest change due to increasing the *a* lattice constant is a significant strengthening of exchange between the 1st nearest-neighbor interlayer Cr pairs. The two relevant interlayer exchange pathways are shown in Figure 5.2-2a. Since the Br p orbitals in the super-super exchange pathway of P1 are nearly orthogonal, they mediate a weak on-site interaction due to due to Hund's rule (Fig. 5.2-2b). On the other hand, the second pathway (P2)

allows for direct hopping in one of the Br (Fig. 5.2-2c). Consequently, P2 dominates the interlayer magnetic coupling between nearest-neighbor Cr-Cr interlayer pairs.

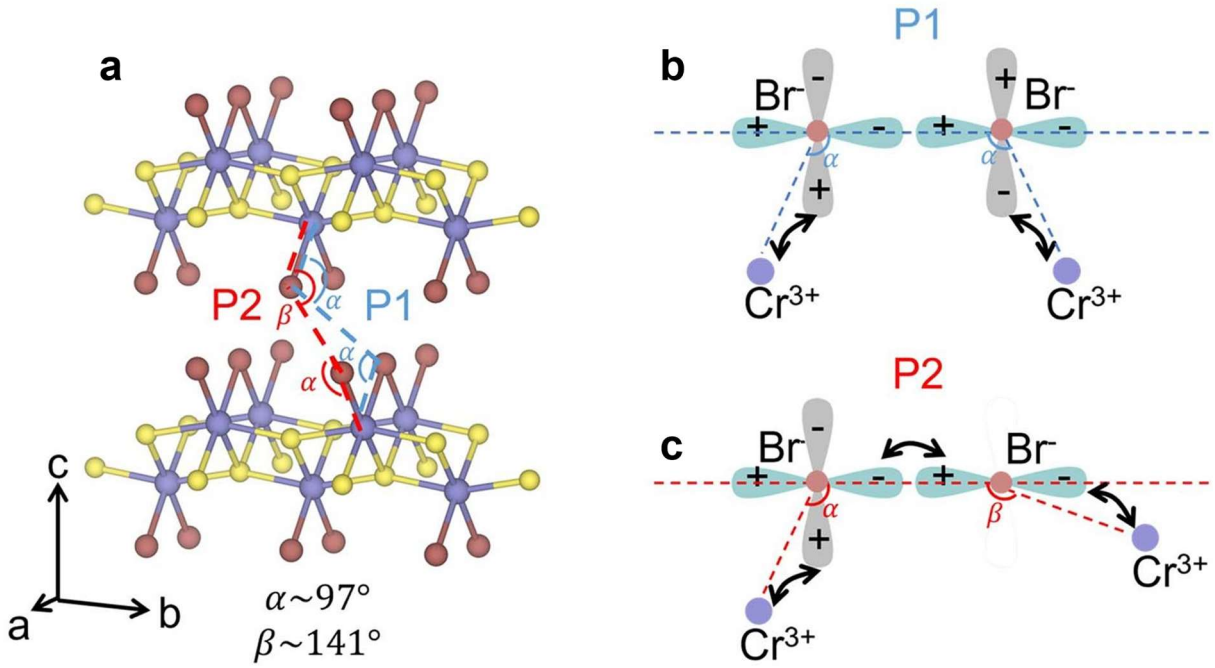

Figure 5.2-2 | Understanding interlayer magnetic coupling in CrSBr. **a**, Two interlayer exchange pathways (P1 and P2) between nearest Cr-Cr interlayer pairs viewed from the side. **b,** Diagram of the P1 exchange pathway, which gives weak interlayer exchange due to the nearly orthogonal Br p orbitals in the super-super exchange pathway. **c**, Depiction of the second exchange pathway (P2). This pathway dominates the interlayer magnetic coupling since it allows for direct hopping in one of the Br. The figures are adapted from Ref. [74]

As we learned before, the sign and magnitude of superexchange can be found using the Goodenough-Kanamori-Anderson rules, with angles of 90° and 180° favoring AFM and FM coupling, respectively. According to the calculation, tensile strain along the *a* axis causes the angle α (responsible for the FM interactions) to become closer to 90°, while the angle (responsible for the AFM contribution) remains relatively unchanged. The overall consequence is that the FM contribution continuously grows, thereby weakening the overall AFM interlayer exchange, until a critical strain where the interlayer exchange becomes overall ferromagnetic and the sample undergoes a strain-induced magnetic phase transition.

5.3 STRAIN ENGINEERING OF MAGNON DISPERSION AND DISCOVERY OF NOVEL MAGNON STATES

In Chapter 2, we demonstrated that the coherent exciton-magnon coupling in CrSBr enables direct measurement of the spin dynamics. In addition to enabling quantum transduction, a key component for new hybrid quantum technologies, fitting of the magnon dispersion with magnetic field enables the extraction of key magnetic parameters, i.e. interlayer exchange and anisotropy. Therefore, in contrast to the photoluminescence, which is only sensitive to the angle between spins, pump probe measurements can provide additional insight into the strain-induced changes to the magnetic order. In addition, these measurements will reveal the effects of strain on the magnon physics, an area which has not been thoroughly studied yet.

Figure 5.3-1a (left) shows the magnetic field dependent pump probe measurements at 0 V of a polyimide-supported sample. Based on the Raman measurements, we estimate a built-in thermal strain of ~ 0.5 %, though with a relatively large uncertainty due to the lack of unstrained reference (i.e., a part of the flake far from the gap). The field is applied at an angle $\theta \sim 9°$ with respect to the *a* axis, resulting in a strong hybridization between the magnon modes. Increasing the strain further leads to dramatic changes in the magnon dispersion as shown in Figure 5.3-1a. Notably, the saturating field shrinks as expected, and the shape of the curve itself changes as well. This point is accentuated by directly comparing the low and high strain data (Fig. 5.3-1a left and right). The tail of the higher energy hybridized magnon mode clearly changes the sign of its curvature (see the white arrow). This provides a clear indication that the physics of the hybridized magnon modes are strongly modified by the strain.

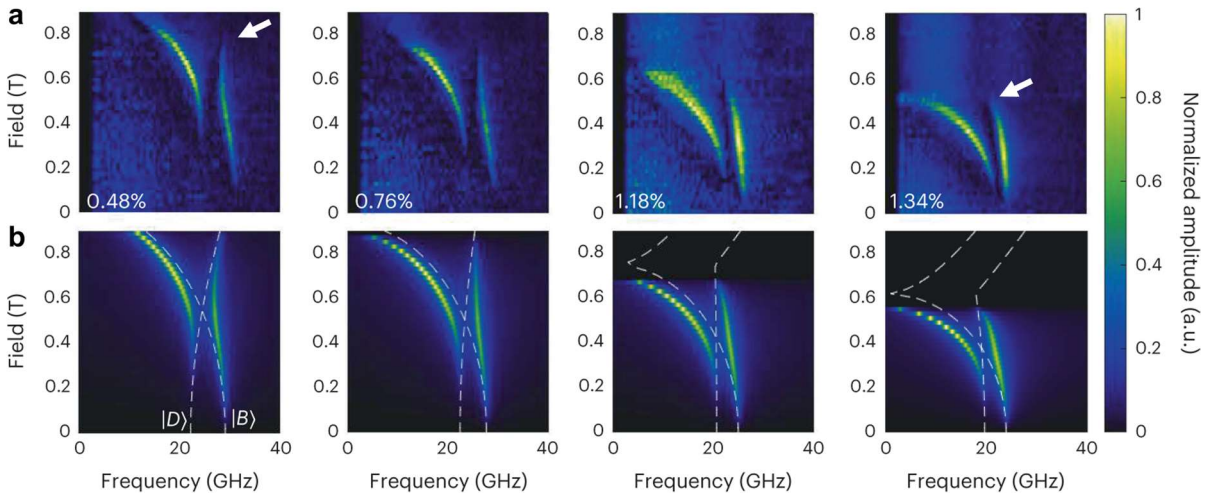

Figure 5.3-1 | Strain tuning of magnon dispersion in CrSBr. **a,** Experimental magnon dispersions observed through transient reflectivity as strain is increased along the *a* axis. The magnetic field is applied at an angle $\theta_{ab} = 9°$. The white arrow indicates the tail of the hybridized |D⟩ mode, which changes curvature with increasing strains. **b,** Corresponding simulations based on the data in **a**. Adapted from Ref. [48]

The excellent agreement between the theoretically modelled magnon dispersion curves and the experimentally measured ones enables further insight into the observed strain effects. Figure 5.3-1b shows the calculated magnon dispersions which match the curvature and brightness of the observed modes. The grey lines and labels denote the two magnon branches, i.e., the dark and bright modes. As in the experiment, the dispersion of the high-field hybridized dark mode changes curvature at high strain. Remarkably, the calculation also shows that the dispersion of the dark mode with applied magnetic field significantly flattens as its curvature changes sign. In fact, the calculation shows that the dark magnon becomes essentially dispersionless with field for the experimentally measured data set taken at a strain of ~ 1.18 %. As far as we know, this is the first time that magnons with this dispersion behavior have been observed. While our understanding of the significance of this new dispersionless magnon state is unclear, one potential use could be in magnonics devices where the insensitivity of the state to magnetic field could be desirable.

In addition to enabling the discovery of novel magnon states, the theoretical modeling of the pump-probe data provides incisive information on the magnetic properties of the sample through the LLG fittings. Figure 5.32a shows the extracted interlayer exchange (J_2) as a function of strain. Clearly, J_2 decreases until it reaches the critical strain, at which point the interlayer coupling switches from AFM to FM and the magnon-exciton coupling is completely turned off, prohibiting further experimental measurement or theoretical modeling of the magnons. On the other hand, the anisotropy (Fig. 5.3-2b) remains unchanged within the experimental error throughout the entire strain range.

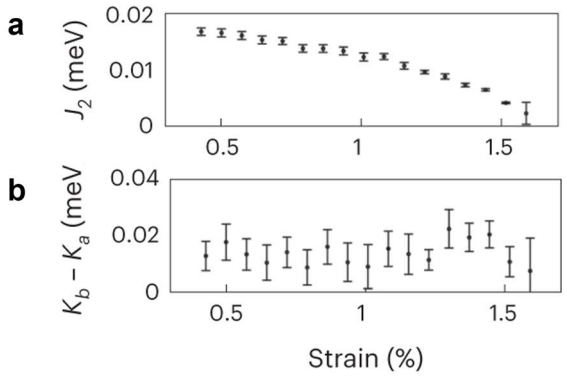

Figure 5.3-2 | Extracted interlayer exchange (**a**) and anisotropy difference **(b**) as a function of strain. Adapted from Ref. [48]

In conclusion, we have utilized the exciton resonance as a sensitive probe of the strain-tuned magnetic order in CrSBr. Tensile strain changes the bond geometry of the material, continuously decreasing the antiferromagnetic interlayer magnetic exchange until it changes sign at a critical strain. The observed hysteresis along the easy axis and lack of response along the intermediate axis in magneto-PL measurements provide unambiguous evidence of ferromagnetism in this high strain state. In addition, the coherent exciton magnon coupling allowed us to study strain-dependent magnon dispersions, resulting in the discovery of novel, dispersionless (with applied magnetic field) magnon modes for the first time. These results highlight CrSBr as a remarkably tunable system, where we can use in-situ tensile strain and magnetic fields to control the magnetic exchange properties to realize designer magnetic states. In the next chapter we will utilize this discovery in functional devices.

Chapter 6. STRAIN-PROGRAMMABLE MAGNETIC TUNNEL JUNCTION

Since charge and spin are coupled in magnetic semiconductors such as CrSBr, control over the magnetic structure through strain enables control over the electronic properties as well. The ability to tune magnetism through strain may therefore provide new opportunities for novel strain-actuated devices. This would overcome one of the challenges of current 2D magnetic tunneling devices, e.g.., MTJs and magnetic Josephson Junctions, which is the requirement of either an external magnetic field or large current pulse[181] to operate. Moreover, the strain-induced magnetic phase transition may obey different physics than the field-induced one. In this regard, the MTJ can also serve as a probe of the magnetic order, with the advantage of extraordinary sensitivity to the vertical magnetic domain structure in the overlap region, typically ~ 500 nm^2.

In this chapter, we will explore the properties of straintronic CrSBr MTJs. Utilizing electron tunneling in combination with standard magneto-transport and photoluminescence measurements will enable us to probe the vertical and lateral domain formation during the magnetic phase transition. In these samples, we find that the strain-induced magnetic phase transition allows for unprecedented control over the layer-dependent magnetism due to vertical strain gradients which form mixed magnetic states during the phase transition. Moreover, by carefully adjusting the strain applied to the sample, we can finely tune the energy difference between parallel and anti-parallel magnetic states. When this difference is sufficiently small, the MTJ starts to switch stochastically, with a strain-tunable response function. These results follow those in our arXiv preprint[182]: https://arxiv.org/ftp/arxiv/papers/2301/2301.03759.pdf.

6.1 STRAINTRONIC CRSBR MTJS

The basic design and optical image of the strain-controlled vdW MTJ is shown in Figure 6.1-1. The heterostructure is essentially the same as the standard silicon based one we studied in Chapter 3. A CrSBr flake approximately ~ 11 nm thick is used as the tunnel barrier to maximize the TMR ratio. Due to the relative air stability of multilayer CrSBr and the poor strain transmission of hBN, we removed the hexagonal boron nitride encapsulating layers, and placed the entire device on a flexible polyimide substrate. In addition, we have added a gold clamping window which covers the entire sample, except for the graphite contacts and a ~ 5 μm window around the junction. We included this window because we initially thought it was necessary for maximizing strain transmission based on the previous literature, a hypothesis which is seemingly contradicted by our later results presented in Chapter 5. However, the gold may indeed play an important role in inducing a strain gradient vertically through the sample. We will find later that this strain gradient likely determines how the magnetic order evolves during the magnetic phase transition.

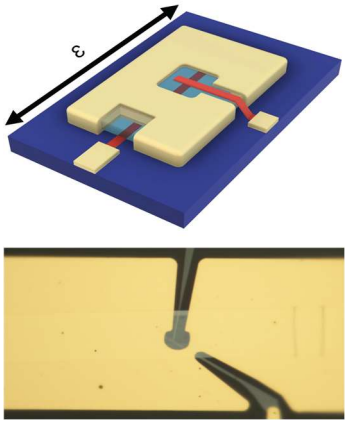

Figure 6.1-1 | Schematic (top) and optical image (bottom) of a straintronic magnetic tunnel junction

An important benchmark for MTJs is the tunneling magnetoresistance ratio, i.e., which is equal to the difference in the resistance of the parallel and anti-parallel alignments divided by the resistance of the parallel configuration. Figure 6.1-2a shows the piezo voltage dependence of the junction's resistance as a function of magnetic field applied along the hard *c* axis at a temperature of 60 K. At -5 V, the system is in the layered AFM state and clearly generates a large TMR ratio of ~ 3100 %, on par with other 2D A-type AFM tunnel junctions, but at higher temperatures. It is worth noting that the device already has a rather large built-in strain of ~ 0.9 %, which lowers the

saturating field along the hard axis substantially. When strain is further increased, the TMR evolves dramatically. The first noticeable change is the large reduction in TMR of ~ 2600 %, on par with the field-induced behavior. In addition, closer inspection reveals the formation of complicated magnetic domain behavior as the magnetic phase transition occurs (see Fig. AIII.1).

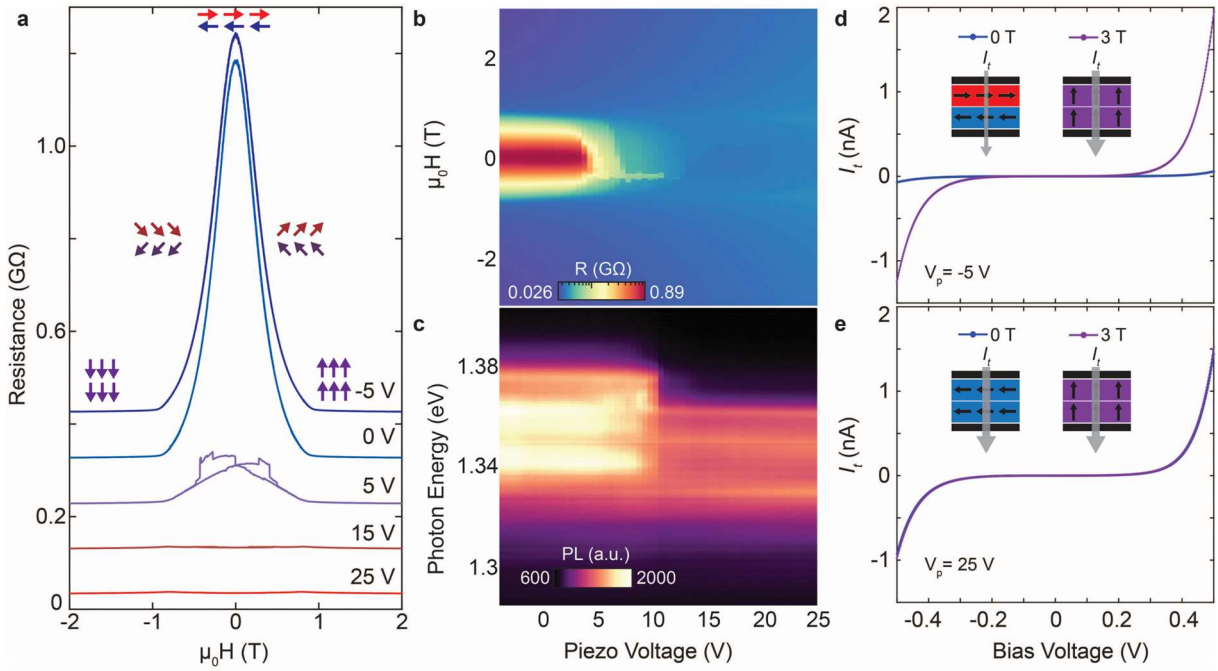

Figure 6.1-2 | Strain dependent tunneling magnetoresistance. **a**, Tunneling magnetoresistance sweeps at select piezo voltages. The inset spin diagrams indicate the changing interlayer spin alignment as the field is swept along the hard (*c*) axis in the low strain (-5 V) state which has AFM interlayer coupling. A bias voltage V_b = 0.5 V is used. **b,** Colormap of the full strain dependent TMR measurements. **c**, Magneto-photoluminescence measurements taken at the junction region as a function of piezo voltage. The close agreement between **b** and **c** indicate the strain-induced phase transition is the origin of the dramatic changes in TMR. **d-e** Bias dependent tunneling current with magnetic fields of 0 T (blue) and 3 T (purple) applied in the low strain (**d**) and high strain (**e**) states. The inset diagrams illustrate the spin configurations. All panels are adapted from Ref. [182]

To investigate the origin of the dramatic changes to TMR and rule out trivial causes such as contact failure, we took concurrent magneto-PL measurements on the junction. Figure 6.1-2b,c show the full strain-dependent TMR and magneto-PL sweeps, respectively. The changes to the TMR correspond well with those observed in magneto-PL, unambiguously proving that the strain-induced AFM to FM phase transition is the cause of the large tunneling magnetoresistance

switching. Further evidence comes from the bias-dependent tunneling characteristics in the low and high magnetic and strain states. The low strain A-type AFM structure serves as a tunnel barrier composed of spin filters with alternating layer magnetization. Therefore, applying a saturating magnetic field in the AFM state strongly enhances the tunneling current with respect to the AFM state (Fig. 6.1-2d). When the strain is increased and CrSBr becomes FM, however, the tunnel barriers are uniform, i.e., all spin filters are aligned. Consequently, we observe little difference between the zero- and high magnetic field bias dependence, similar to what has been reported for other FM tunnel barriers[183] (Fig. 6.1-2e).

Having established the presence of the AFM to FM transition in the device, we proceed to study the zero-field strain-induced behavior. Fig. 6.1-3a shows piezo voltage dependent tunneling measurements with no applied magnetic field. A large and reversible TMR switching is observed. This straintronic switching is very robust, with no visible signs of wrinkling or slipping over the entire measurement (> 100 cycles). In addition, the operation of the MTJ can work at much higher temperature than other 2D MTJs due to the high ordering temperature of CrSBr. Figure 6.1-3b shows strain switching cycles at select temperatures. A large TMR difference between low-strain and high strain states is maintained, although the strain-induced magnetic phase transition gets broader at higher temperatures. Fig. 6.1-3c shows that the zero-field strain-induced TMR exceeds 10,000 % at 30 K, and remains above 100 % up to ≈ 140 K, above the unstrained CrSBr Neel temperature of ~ 132 K. Interestingly, a dome-shaped positive magnetoresistance as a function of field appears when a large piezo voltage is applied at 155 K (Fig. 6.1-3d), which looks similar to the positive magnetoresistance shown in the high strain state (Fig. AIII.1d). The induced positive MRR likely arises from the enhancement of interlayer FM exchange which may result in the previously reported[61] intermediate FM (iFM) phase consisting of individual ferromagnetic

monolayers with paramagnetic interlayer coupling, becoming a long-range FM ordered phase. The study of this iFM to FM magnetic phase transition, and the exploration of even higher temperatures and strains is left for future studies.

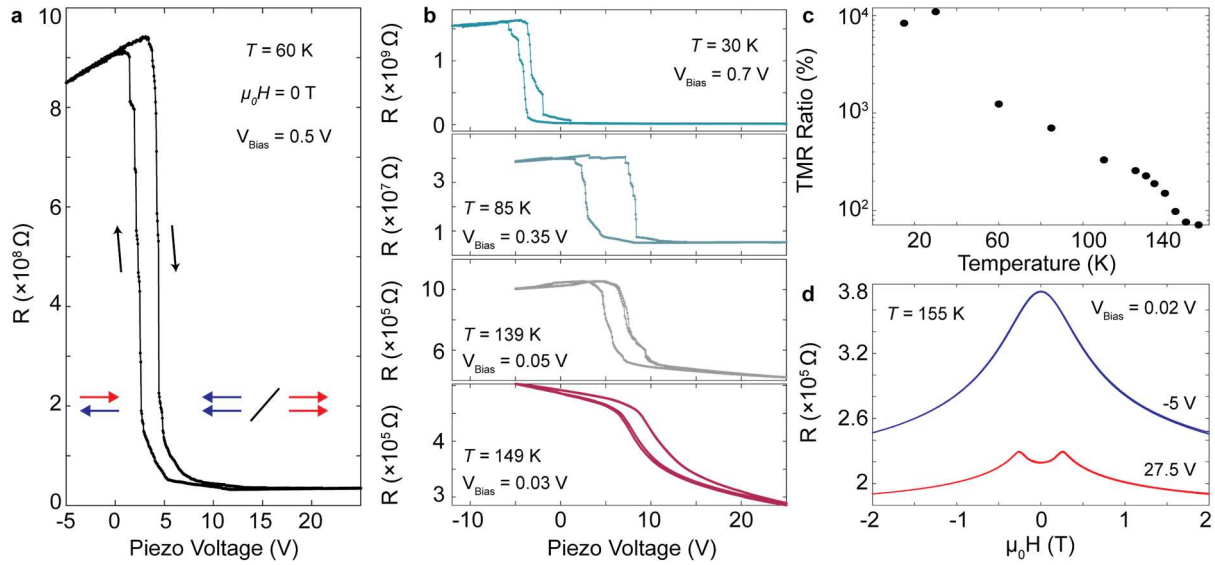

Figure 6.1-3 | Zero field strain switching of the CrSBr MTJ. **a**, Resistance of the device as a function of piezo voltage taken at zero field and a temperature of 60 K. The black and colored arrows indicate the sweep direction and interlayer magnetic coupling, respectively. **b,** Strain switching sweeps at select temperatures. At elevated temperatures, the switching becomes broader, but a large TMR ratio is maintained. **c,** Strain-induced TMR ratio as a function of temperature. **d**, Magnetic field dependence of the junction resistance at an elevated temperature $T = 155$ K, above the Neel temperature of CrSBr. With strain, the TMR switches from a broad, paramagnetic-like negative magnetoresistance behavior to a dome of positive magnetoresistance. Reproduced from Ref. [182]

6.2 Probing Domain Formation During the Strain-Induced AFM to FM Transition

Closer inspection of the strain-switching curves reveals several steps in TMR, indicating the presence of complex magnetic domains. Considering the observed hysteresis in the AFM to FM phase transition as a function of strain (see Figure 5.1-2d), we expect a first order magnetic phase transition with a mixed phase in between the AFM and FM phase. But how do domains nucleate during the magnetic phase transition? Considering the rarity of strain-induced magnetic phase

transitions in the literature, it is not immediately clear what the microscopic magnetic structure of the sample should look like. Fortunately, we can use the coupling of spin and charge in this material to probe the physics and magnetic structure during the phase transition.

While the MTJ is only sensitive to the domain formation within the ~ 500 nm^2 device overlap region, we can use magneto-PL to map the domain formation across the entire device. The validity of this approach is confirmed by directly comparing the magneto-PL sweep taken on the junction region with the TMR (Fig. 6.2-1a-b). The curves show general agreement, with similar domain behavior and saturating field. Figure 6.2-1d-g shows magneto-PL measurements taken at several places across the sample (indicated by the colored circles in the optical image, Fig. 6.2-1c). This course mapping shows that spots separated by several microns around the sample have similar domain behavior. Therefore, we conclude that the domains probed by the MTJ arise from

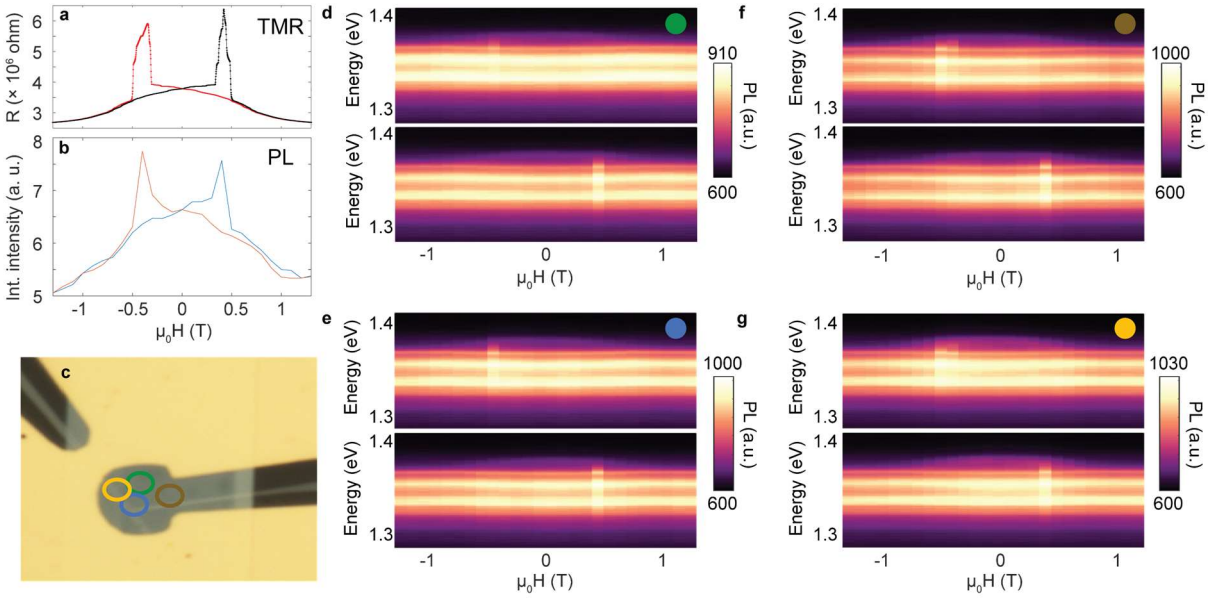

Figure 6.2-1 | Mapping magnetic domain formation in the CrSBr MTJ. **a-b**, Comparison of the magnetic field dependent tunneling magnetoresistance (**a**) and integrated intensity of the photoluminescence spectra (**b**) taken at the junction spot. The similarity between the two experiments indicates that both measurements probe the same magnetic domain structure. **c-g,** Optical image of the device (**c**) with markers indicating where the various magneto-PL measurements (**d-g**) are taken. Reproduced from Ref. [182]

vertical domains, and not lateral domains. The origin of such vertical magnetic domains that are uniform for microns across the sample suggests that domains form layer-wise instead of laterally at defect sites, for example.

We can further confirm that layer-wise vertical magnetic domains form during the strain-induced magnetic phase transition by studying the strain-dependent magnetoresistance of a CrSBr lateral transport device (Fig. 6.2-2a). Figure 6.2-2b shows the MRR as a function of piezo voltage and magnetic field, with the field applied along the intermediate *a* axis at a temperature of 105 K. The field direction is limited by the strain cell we designed for the PPMS. At 90 V, a sudden change in the MRR is observed, where the large negative MRR strongly decreases. This corresponds to the AFM to FM phase transition, which is accentuated by taking the numerical derivative of MRR, plotted in Figure 6.2-2c. It is worth recalling Chapter 3, where we established that multiple magnetoresistance mechanisms can exist, complicating deeper understanding of the shape of MRR curve in the FM state. However, the lack of clear domain formation during the phase transition supports the picture that domains mostly form vertically instead of laterally.

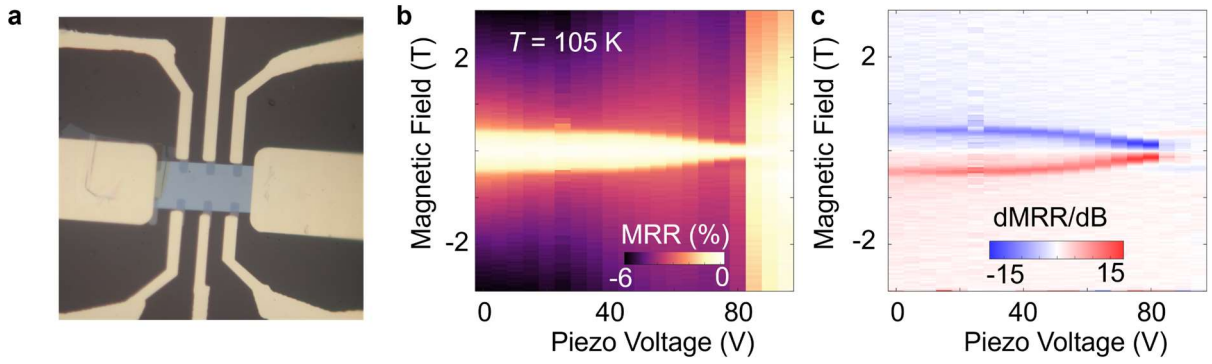

Figure 6.2-2 | Strain dependent lateral magnetotransport in thin bulk CrSBr. **a**, Optical image of the strain device. **b,** Piezo voltage dependent magnetoresistance sweeps taken at a temperature of 105 K. The field is swept along the *a* (intermediate) axis. **c,** Numerical derivative of **b**.

6.3 Understanding Field and Strain Induced Magnetic Phase Transitions

To gain insight into how the layer-dependent magnetic order evolves during AFM to FM phase transitions, we first consider the well-studied magnetic field induced AFM to FM phase transition in A-type MTJs. In A-type AFMs, the oppositely magnetized layers create an effective exchange bias on the adjacent layers[184]. Therefore, the critical field required to cause the spin-flip transition depends on the number of AFM interfaces. To illustrate this point, Figure 6.3-1 shows a seven-layer CrSBr flake. The top and bottom layers have a single AFM interface and are therefore distinct from the interior bulk layers which all have two AFM interfaces. Consequently, the surface layers will have a smaller critical field than the interior ones. When the magnetic field is increased, these layers will flip first, giving the mixed magnetic state shown in Figure 6.3-1. At this point, the rest of the flake is degenerate in energy and critical field since they all have the same number of AFM interfaces. When the field is further increased, all interior layers should flip at the same field into the FM state (Fig. 6.3-1 right). Therefore, we should expect that multi-layer A-type vdW MTJs will have three states regardless of thickness: the high resistance zero-field AFM state, the intermediate state with FM surface layers and AFM bulk, and the low resistance high-field totally FM state. This picture is supported by results from multi-layer CrI_3 tunnel junctions, where two

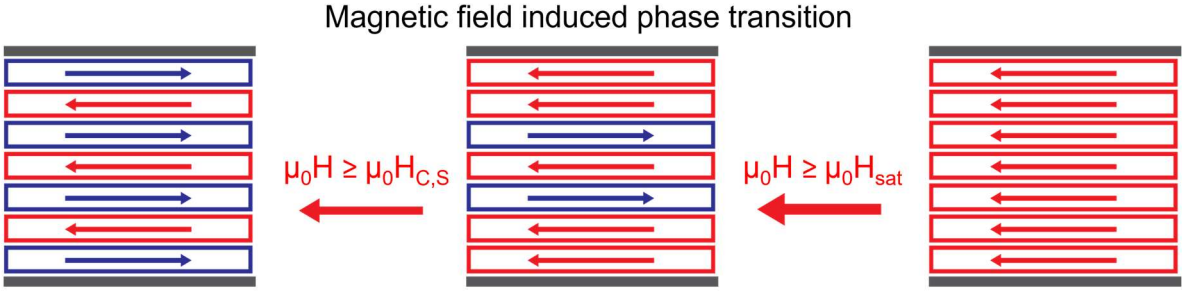

Figure 6.3-1 | Illustration of magnetic field induced AFM to FM transition. When the applied field exceeds the critical field of the surface layers ($\mu_0 H_{C,S}$), they align and create a mixed magnetic state. When the field is further increased and exceeds the critical field of the bulk layers ($\mu_0 H_{sat}$), the entire flake becomes ferromagnetic.

prominent jumps in TMR are observed regardless of the sample thickness[105]. It is worth noting, however, that additional jumps could arise from stacking faults, defects, or unintentional strains in the crystal lattice which can break the energy degeneracy of the intermediate layers. In addition, the application of a vertical electric field in gated atomically thin MTJs may serve a similar role[185]. However, the very nature of the magnetic phase transition seems to present a significant challenge for harnessing the large number of spin-filters present in multi-layer A-type vdW MTJs to realize a multitude of distinct, controllable magnetoresistance states.

Intuitively, we expect that the evolution of the magnetic structure during the strain-induced phase transition is very different from that of the magnetic field-induced phase transition. In this case, the phase transition occurs when the strain exceeds some critical value. In principle, if all the layers have exactly equal strain, we could expect that the layers should flip all at once in a sharp spin-flip transition, similar to the last stage of the field-induced transition. However, if there is any strain gradient vertically through the sample, it will break the energy degeneracy of the layers. We take the same seven-layer CrSBr as an example, but with greater strain on the top layers than the bottom ones (Fig. 6.3-2). As the strain is increased, the top layers will reach the critical strain threshold first and become FM, followed progressively by the rest of the flake. Therefore, the strain-induced magnetic phase transition can favor the formation of vertical, layer-dependent mixed magnetic states as we observed in the previous section, given that there is a vertical strain gradient present in the sample.

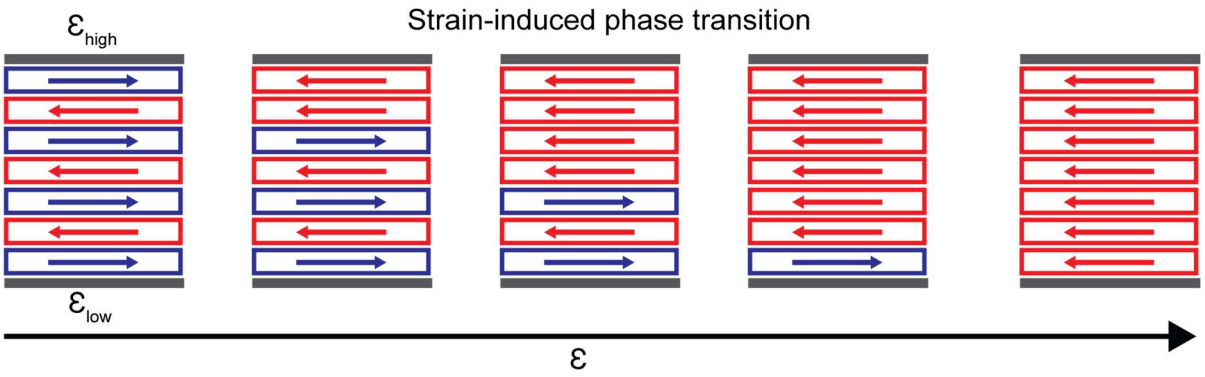

Figure 6.3-2 | Illustration of strain-induced AFM to FM transition. A vertical strain gradient breaks the energy degeneracy of the layers, leading to layer-by-layer flipping with increasing strain.

The presence of strain gradients seems to be at odds with the results presented in Chapter 4, where we established a robust strain transmission through multilayer CrSBr when the sample is directly deposited on polyimide. However, it is important to note that the clamping scheme used in these MTJ samples creates very different environments for the top and bottom layers of the CrSBr flake. For instance, the bottom surface is directly in contact with the polyimide except for the extremely narrow region on top of the graphite contact, while the top is clamped by gold. In this case, we speculate that the mismatched Poisson's ratio of gold may lead to a different strain on the top than on the bottom layers. More careful consideration of the origin of the vertical strain gradient and deliberate engineering of its magnitude and profile is an interesting direction for future work. The presence of the vertical strain gradient, regardless of its origin, seems to provide a powerful tool for breaking the energy degeneracy of the layers in the MTJ, enabling far greater control over the layer-dependent magnetic order than magnetic field.

An implication of the layer-wise strain-induced AFM to FM transitions is that devices with increasing thickness should have a greater number of magnetoresistive states that form during the phase transition. Figure 6.3-3 shows the derivative of TMR for MTJs with varying CrSBr thickness. With increasing thickness, we clearly observe a greater number of domains which occur

in the intermediate states between the AFM and FM orders. It is challenging to model what these domains exactly correspond to because the field is applied along either the intermediate (Fig. 6.3-3a,b) or hard axis (Fig. 6.3-3c) due to cryostat limitations. In addition, the strain gradient results in layer-dependent critical fields with possible exchange bias effects at the mixed AFM/FM interfaces. Consequently, the behavior of the magnetic structure under magnetic field, especially in the canted AFM states, could be extremely complex. Nevertheless, the trend of increasing domain complexity with increasing thickness agrees with the basic picture outlined above.

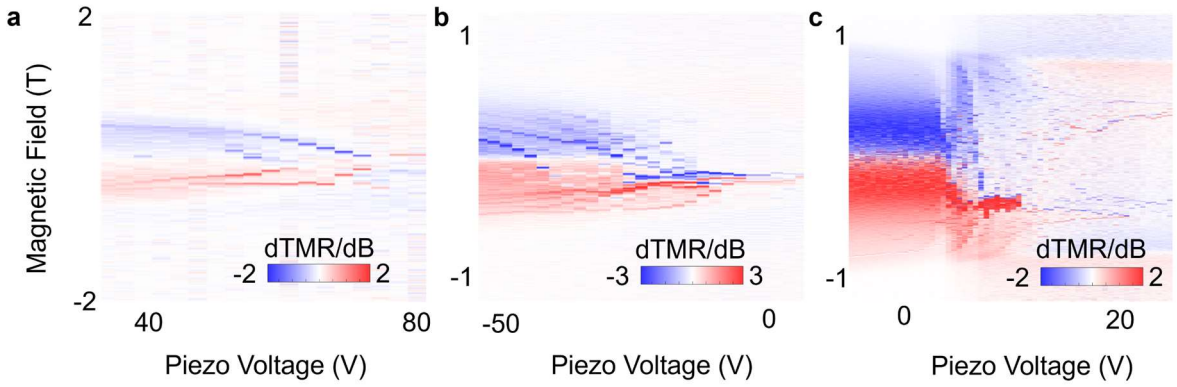

Figure 6.3-3 | Thickness dependence of the strain-induced magnetic phase transition probed by electron tunneling. **a-c,** Derivative of the tunneling magnetoresistance as a function of piezo voltage and magnetic field for 6-layer (**a**), intermediate thickness (estimated to be ~ 7 nm) (**b**), and 11 nm (~ 14 layers) (**c**) MTJ devices. The magnetic field is applied along the *a* axis for **a** and **b**, and along the *c* axis for **c**.

The distinct nature of the strain-induced AFM to FM transition should enable the creation of a plethora of magnetoresistive states which can be switched using strain. To explore this possibility, we first adjusted the static DC strain to be very close to the AFM to FM transition. Then, we applied a square-wave AC strain pulse to the sample (see Fig. 6.3-4 inset). Figure 6.3-4 shows the MTJ output as the magnitude of the strain pulse is increase from 5 mV to 250 mV. When the pulse amplitude reaches $\approx$ 24 mV, generating a strain of only $\approx$ 0.0008 % based on the Raman measurements, the tunneling current measured during the strain pulse jumps into a

distinctly stable state (left-most purple arrow in Fig. 6.3-4). This behavior corresponds to switching between two layered magnetic configurations, i.e., the strain pulse actively flips the magnetization direction of individual layers. Based on these measurements, we obtain a gauge factor $GF = \frac{\frac{\Delta R}{R}}{\Delta \varepsilon} \sim 3500$, among the largest values reported in any system to date[186,187]. Further increasing the magnitude of the strain pulse increases the number of layers which are flipped. These additional distinct jumps into stable magnetic configurations are observed with increasing pulse amplitude (purple arrows in Fig. 6.3-4). Interestingly, a sufficiently large strain pulse also seems to change the static state tunneling current, i.e. the current after the pulse ceases. Therefore, it seems that the strain pulse can write the steady-state magnetic configuration.

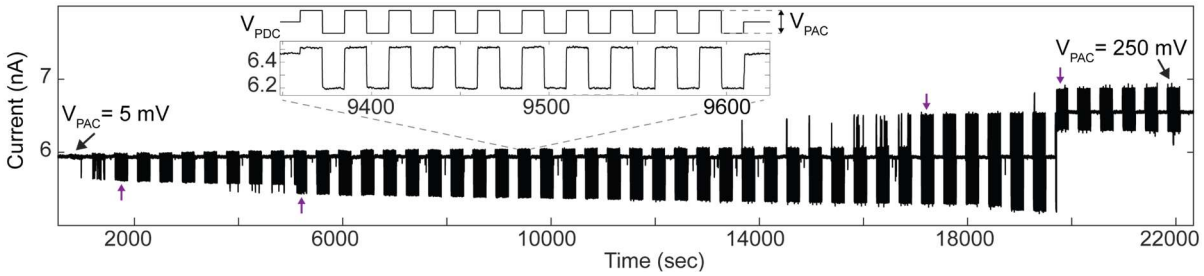

Figure 6.3-4 | Strain pulse control of multiple magnetoresistive states. In this experiment, the static strain (V_{PDC}) is adjusted to be near the phase transition, and then a square wave strain pulse (V_{PAC}) is applied on top of the DC voltage, as shown in the inset. The pulse amplitude is increased from the smallest value of 5 mV (left) to 250 mV (right). The purple arrows indicate pulse amplitudes where distinct stable states are realized. Adapted from Ref. [182]

The strain-pulse behavior observed near the AFM to FM transition is entirely different than in the purely FM or purely AFM states. In those states, increasing the magnitude of the strain pulse only results in small, continuous changes at a gauge factor three orders of magnitude smaller than during the phase transition, and with no change in the static current (AIII.2). Therefore, we conclude that the switching shown in Fig. 6.3-4 arises from manipulating vertical layer-dependent magnetization in the mixed magnetic states. These results highlight that the unique strain-induced

magnetic phase transition enables the control of multiple TMR states, which can be actively written using extremely small strain pulses.

6.4 CREATION OF METASTABLE STATES

When the energy difference between the AFM and FM configurations becomes very small, the layer magnetization can switch back and forth between parallel and anti-parallel. This stochastic switching in MTJs can serve as a probabilistic bit, or p-bit[144,145]. In contrast to binary bits which are either '0' or '1' and qubits which are superpositions of '0s' and '1's, the p-bit switches back and forth between '0' and '1' with some probability (Figure 6.4-1). Because stochastic MTJ p-bits utilize a physical stochastic process, they offer significant efficiency over CMOS-based circuits when it comes to executing probabilistic computing, e.g., solving certain models[144,188]. For instance, this concept has recently been utilized in pioneering works demonstrating efficient integer factorization using stochastic MTJs. Comparing the performance in integer factorization of the p-bits to conventional CMOS with digital random number generators (RNG), the work[144] found that the p-bits offer an energy advantage by a factor of 10, and an area advantage by a factor of 300.

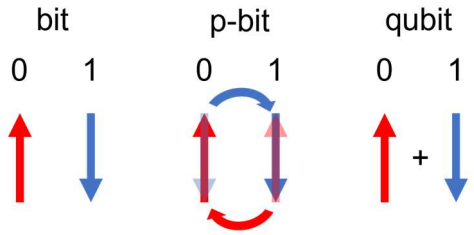

Figure 6.4-1 | Types of computing bits. Classical bits (left) consist of a 0 or 1, qubits (right) consist of superpositions of 0s and 1s, while p-bits (middle) fluctuate back and forth between 0 and 1.

A defining feature of the p-bit is the stochastic switching between two magnetization states, and the ability to bias the distribution towards either the zero or the one state. In contrast to the extremely stable MTJs used for magnetic memory, the stochastic ones are purposefully designed to be unstable. In terms of the free energy of the system, the energy difference between parallel and antiparallel, ΔE, is greater than 60 times and ~ 15 times the thermal energy for the

stable and stochastic MTJs, respectively. In conventional MTJ technologies used today, ΔE is fixed by the growth conditions. The continual tuning of interlayer exchange in strained CrSBr established in Chapter 5 therefore offers a new method for tuning the energetics and stochasticity of the MTJ in-situ.

Closer inspection of the strain-pulse measurement already reveals the signatures of metastable states when the pulse magnitude is nearly enough to switch the MTJ into a new stable state, as explored in the previous section (Fig. 6.3-4). During the trough of the square wave pulse, the device started to switch back and forth into the stable state, which is then completely stabilized when the pulse magnitude is further increased. By adjusting the static strain to near where the switching occurs, we can proceed to carefully study the switching characteristics under the tuning knobs of strain and bias voltage. Figure 6.4-2a shows the tunneling current as a function of time as the static piezo voltage is adjusted. Beginning with the stable magnetic domain structure, we increase the static strain, V_{PDC}, by 14 mV (red arrow). In this condition, the tunneling current begins to switch between two values. Decreasing the piezo voltage back to the original value (blue arrow), returns the tunneling current to the original stable value. This demonstrates that the stochastic switching can be reliably turned on and off. To our knowledge, this is the first realization of p-bit type operation using a vdW MTJ to our knowledge. Moreover, the ability to switch between stable and stochastic domains, i.e, between MRAM and p-bit type functionalities, is unique to this system due to the ability to finely and continuously tune the energy barrier between magnetic configurations (Fig.6.4-2b).

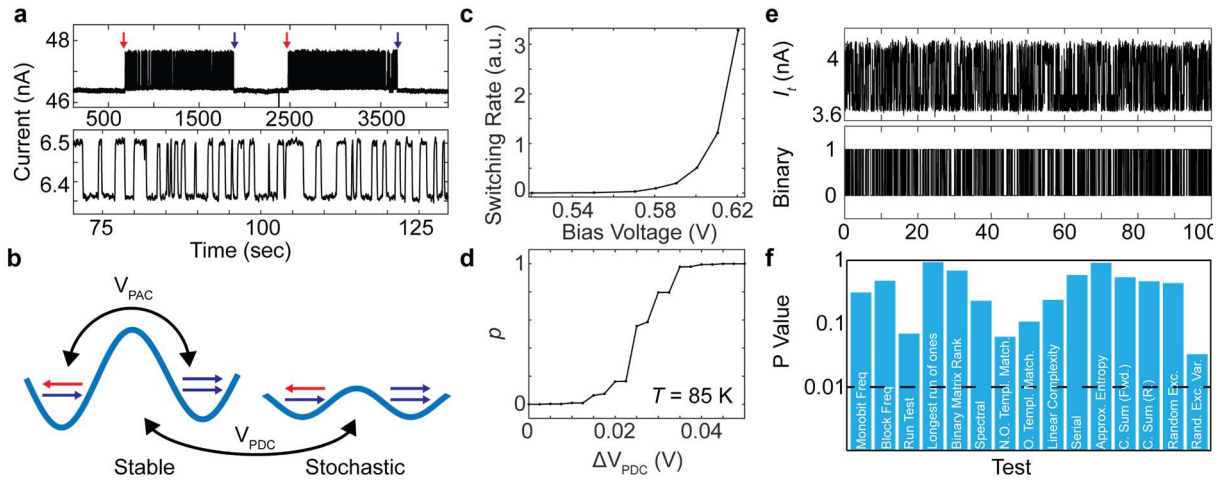

Figure 6.4-2 | Creating and controlling metastable states. **a,** Tunneling current measured over time as the static piezo voltage is increased (red arrow) and decreased (blue arrow) by 14 mV. Initially, the MTJ is in a stable magnetic state during the AFM to FM phase transition. Bottom: zoom in of switching events with finer time resolution. **b,** Functionalities of the strained MTJ. Applying strain pulses (V_{PAC}) causes dynamic layer flipping between stable states, while adjusting the static strain (V_{PDC}) to lower the energy barrier between AFM and FM configurations enables stochastic switching. **c,** Bias voltage dependence of the switching rate. **d,** Response function, ρ, as a function of the change in static piezo voltage. This value is calculated by converting the MTJ output to a binary sequence and taking the average over the entire time window. **e,** MTJ output (top) and converted binary output (bottom) taken near ρ = 0.5 (i.e., roughly equal number of 0s and 1s) as a function of time. **f,** Results of the NIST test suite applied to the MTJ output in **e** after sampling with a sampling time of .1760 seconds. The grey line indicates a p-value of .01, which is the standard cut-off for a test to be considered successful. Adapted from Ref. [182]

Defining the lower current state as a '0' and the higher current state as a '1', allows us to convert the MTJ output to a binary sequence and study the response of the domain switching to external control knobs, i.e., applied bias voltage and strain. Figure 6.4-2c shows that increasing the bias voltage applied to the MTJ results in a large increase of the switching rate. The origin of this bias voltage dependence is likely spin transfer torque effects from a mixed magnetic domain structure (see next section). Keeping the bias voltage fixed, we explore how changing the static strain affects the stochasticity of the device. A simple indicator of the stochasticity is given by the response function, ρ, which is calculated by taking the average of the binary sequence over the entire time window. This is essentially the probability of finding the MTJ in either the '0' or

'1' state at any given time. Therefore, $\rho = 0$ or 1 indicates a stable magnetic configuration, and a value of 0.5 corresponds to equal fluctuations between the two stable states. Figure 6.4-2d shows the response function as the static strain is finely increased. A sigmoidal dependence on the applied strain is observed. The nonlinear sigmoidal response function is reminiscent of p-bits, and stochastic binary neurons[189].

In principle, the ability to tune the response function should enable random number generation at $\rho = 0.5$, and a biased Bernoulli sequence when tuned to either higher or lower values. In addition to strain, the applied bias voltage can also be used to tune ρ by changing the switching rate, possibly providing finer control. This can also allow interactions between multiple p-bits. The two independent control parameters of strain and bias voltage could allow independent tuning of the p-bit's effective temperature and energy landscape, thereby enabling direct stochastic annealing of the system. Such a scheme should reduce the circuit complexity required for large-scale analog p-bit annealing, though further study is needed to explore the full mapping between the two-dimensional (i.e., strain and bias) voltage landscape and the behavior of the p-bit dynamics.

To test the stochasticity of the device, we can further analyze the switching data taken when $\rho \approx 0.5$, which is a binary sequence with near equal 1s and 0s, as shown in Fig. 6.4-2e. Since the lock-in detection scheme measures the tunneling current much faster than the domain switching rate, we must down-sample the data. Using data collected over 200 seconds, we used 15 tests from the NIST test suite[190] to assess the stochasticity. The Maurer's Universal Test was excluded because the sequence was not sufficiently large enough. Fig. 6.4-2f shows the results of all 15 tests using a sampling time of 0.1760 seconds, which was found to be slower than the switching speed (see below). The grey line corresponds to a p-value of 0.01, which is a standard

threshold for which the test is considered successful. These results suggest that the generated binary sequence has a high degree of randomness, but the relatively small sequence size calls for additional analysis.

The full sampling time dependence on the number of passed tests is plotted in Fig. 6.4-3, using the standard pass-fail threshold p-value of .01. The grey line indicates the point at which the sequence passed all 15 considered tests. The sequence is sufficiently random only when the sampling time exceeds the average domain switching time (red line in Fig. 6.4-3) which is calculated by dividing the total number of switches the total time window (i.e. 200 seconds).

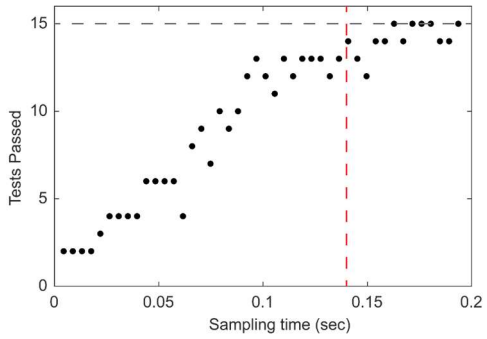

Figure 6.4-3 | Sampling time dependence of NIST test suite results. Grey line indicates the passing of all tests, and the red is the sample switching rate. Adapted from Ref. [182]

We further analyzed the stochasticity by comparing the extracted dwell times, i.e. the time between switches, of the 0 and 1 states. The dwell times for the 0 and 1 states are plotted as a histogram, and follow an exponential envelope as expected for a Poisson process (Fig. 6.4-4).

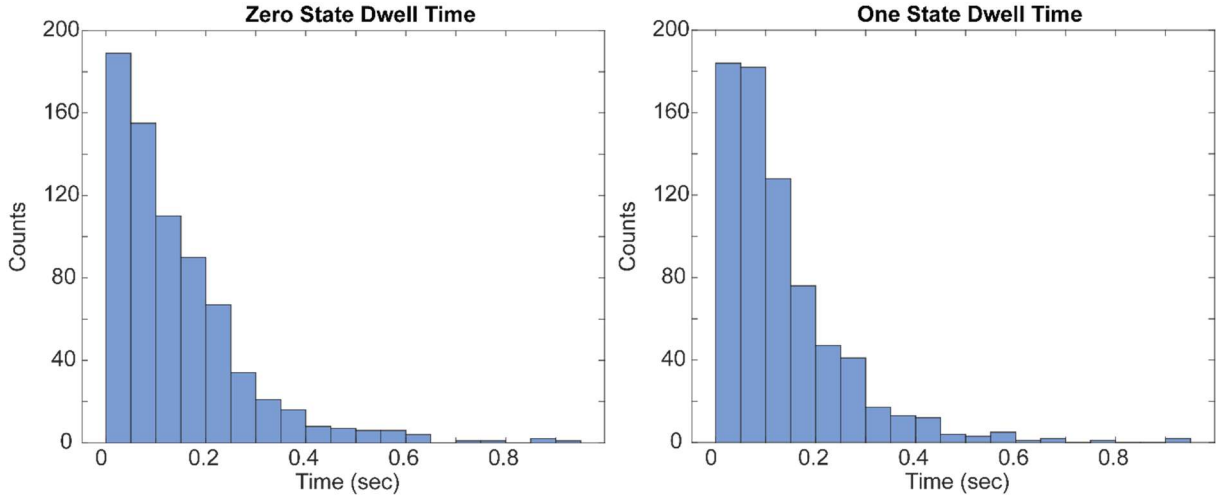

Figure 6.4-4 | Dwell time histograms for the zero state (left) and one state (Right). Adapted from Ref. [182]

We can find the characteristic lifetime, τ, by plotting the logarithm of the histogram bin counts versus the dwell time:

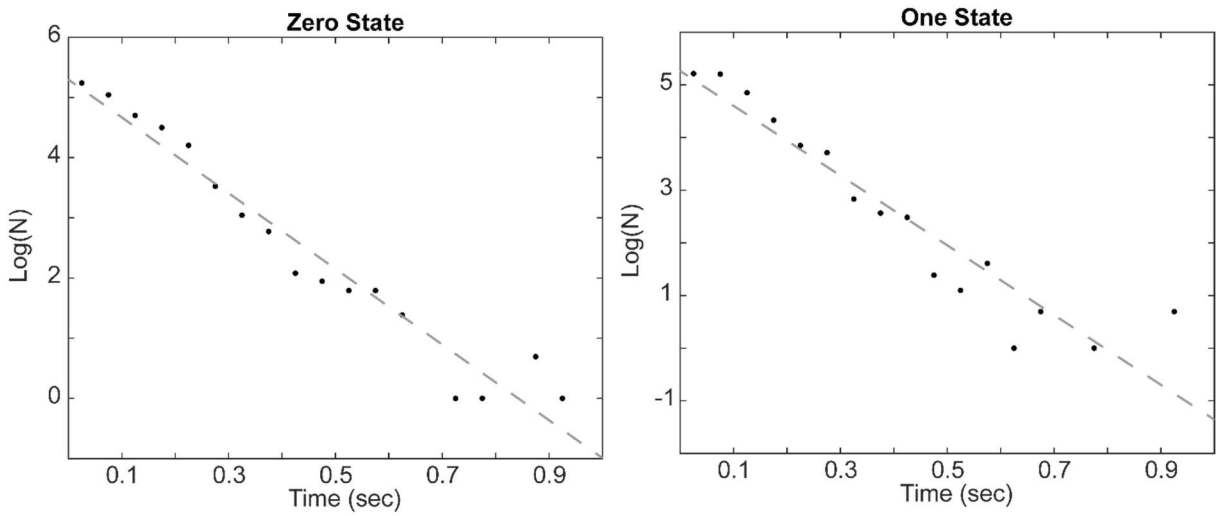

Figure 6.4-5 | Extracting lifetimes of the zero (left) and one state (right). The line is a linear fit of the bin counts as a function of time. Adapted from Ref. [182]

Based on the linear fits, we find the characteristic lifetimes of the 0 and 1 states to be $\tau_0 = 159 \pm 9$ ms and $\tau_1 = 151 \pm 9$ ms, respectively, where the uncertainty is obtained by the standard deviation of the linear fit. Importantly, these values indicate that the time spent in the 0 and 1 states are equal within the uncertainty of the analysis. Combined with the results of the NIST statistical tests, and the physical origin of the switching events, we conclude that our stochastic MTJ can generate binary sequences with a high degree of randomness.

6.5 FUTURE DIRECTIONS

Having established stochastic functionality for the first time in a vdW MTJ, the next natural step is to explore architectures for scaling device fabrication for potential neuromorphic and probabilistic computing applications. In this regard, the vdW nature can serve as both a blessing and a curse. On the one hand, 2D materials fabrication, which requires careful exfoliation, searching, and stacking, is not yet at a stage suitable for commercial use. On the

other hand, many tools have been developed to pattern and control these materials on the nanoscale. For instance, patterning[191,192] the graphite contacts into strips could enable the realization of a "cross-bar geometry" (Fig. 6.5.1), which is a common architecture used in cutting-edge MTJ devices[193]. This fabrication procedure could enable the creation of an array of 2D stochastic MTJs, provided that the strain of each MTJ is similar. Therefore, engineering homogeneous strain on each p-bit will be imperative. Careful measurement scheme and choice of CrSBr tunnel barrier to optimize switching rate and desired resistances values will be important considerations as well. If this can be achieved, then the stochasticity of each p-bit can be controlled by the applied bias voltage, as seen in the previous subsection. Then, the probabilistic computer can be realized by allowing the output of the MTJs in the cross-bar to change the applied bias voltage to the other ones, i.e., letting p-bit 1 and p-bit 2 in Fig. 6.5-1 "talk" to each other.

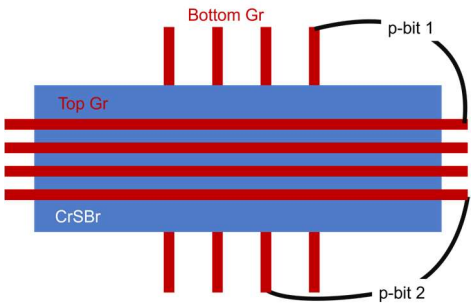

Figure 6.5-1 | CrSBr MTJ array using the crossbar geometry.

In addition to new geometries, another pressing issue is the fabrication of truly atomically thin p-bit MTJs. In Figure 6.5-2 we show the results obtained from a 6 layer straintronic MTJ. The device clearly shows the strain-induced magnetic phase transition (Fig. 6.5-2a-c) and stochastic metastable states (Fig. 6.5-2d-e). However, the TMR ratio is significantly smaller than in the device which used an 11 nm CrSBr tunnel barrier. One possibility is that the sample partially degraded during the device fabrication as it was exposed directly to air and solvents. Previous studies on CrSBr have shown that the monolayer is extremely air sensitive, while thicker samples are apparently not, but solvent and heating exposure have not been established yet. One way we could test and solve this problem is to use an hBN capping layer which will

protect the flake from air and solvents, as we did for CrI_3. However, we note that the doubly encapsulated bilayer sample studied in Chapter 3 was entirely fabricated in the glovebox, also showed much smaller TMR than the thin bulk sample, indicating that the TMR of such few atomic layer devices may ultimately be limited. Therefore, the choice of CrSBr tunnel barrier thickness may vary depending on the specific application.

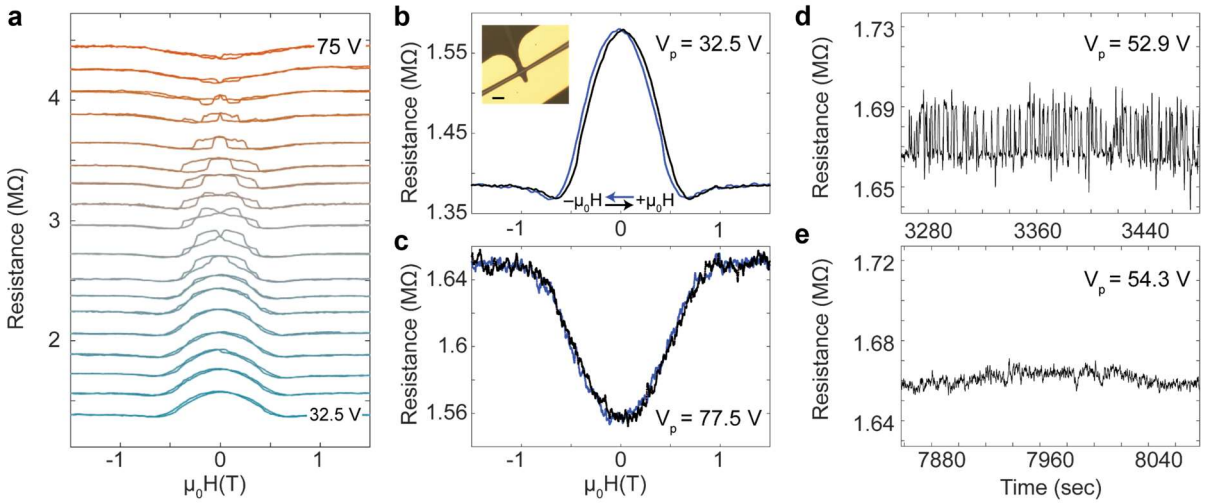

Figure 6.5-2 | Six layer strain-actuated CrSBr magnetic tunnel junction. **a,** Magnetoresistance sweeps of a MTJ with a six-layer CrSBr tunnel barrier as the piezo voltage is ramped from 32.5 V (blue) to 75 V (red). The magnetic field is swept along the *a* axis at a nominal sample temperature of 20 K, and the curves are offset for clarity. **b-c,** TMR sweeps in the low strain AFM (**b**) and high strain FM (**c**) states, demonstrating switching from negative to positive MR. An optical image of the device is inset in **b,** scale bar: 5 μm. **d-e,** Resistance measured over time at select piezo voltages. Metastable domain switching (**d**) that is stabilized by slightly increasing strain (**e**) is observed, similar to the thicker flake. Reproduced from Ref. [182]

An important observation in the metastable states of both the six layer and 11 nm CrSBr MTJs is that the switching behavior depends on the polarity of the bias voltage. Figure 6.5-3a,b shows the MTJ output over time of a metastable state with currents of similar magnitude flowing in different directions. When negative bias voltage is applied, we observe no switching. This curious observation implies that heating is not the origin of the increased switching rate with bias voltage. Instead, the data suggests an asymmetric vertical magnetic domain structure rate (Fig. 6.5-3c), which is consistent with the previous results in this chapter. When electrons tunnel through the

sample, a difference in spin polarization and thus spin transfer torque arises when the tunneling current flows in opposite directions. A fascinating direction is to explore whether the mixed domain structure in Figure 6.5-2c can give rise to other spintronic effects which can happen at AFM/FM interfaces. These effects include exchange bias[194], magnetic ratchet effects[195], full magnetization flipping through spin transfer torque, etc.

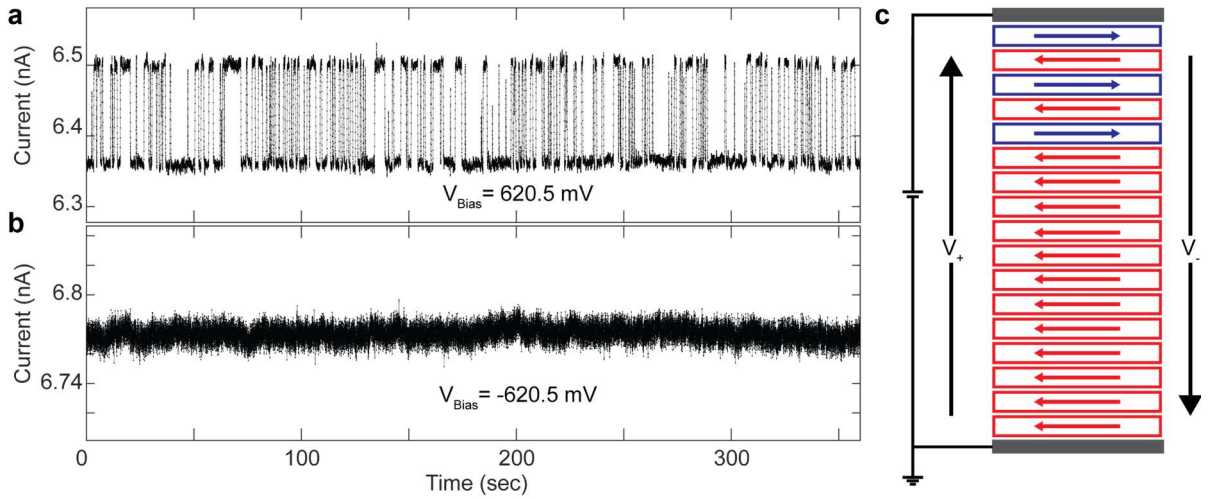

Figure 6.5-3 | Bias polarity dependent switching and asymmetric vertical magnetic domain structure. **a-b,** Tunneling current of a metastable state measured over time with a positive (**a**) and negative (**b**) bias applied to the 11nm CrSBr MTJ. A stable current of similar magnitude is measured under negative bias, ruling out heating effects. Instead, the behavior indicates an asymmetric vertical magnetic domain structure illustrated in (**c**). Adapted from Ref. [182]

Another exciting opportunity is to leverage the strain-induced magnetic phase transition in other types of quantum devices. A remarkable advantage of these devices is that the all-vdW heterostructure offers atomically sharp interfaces without lattice matching considerations which limit the types of samples which can be grown using traditional techniques. For instance, we can easily replace the metallic graphite contacts for superconducting contacts to form magnetic Josephson Junctions (JJs)[196-201]. The strain-programmability of the CrSBr tunnel barrier could then enable field-free control of the phase of the JJ, and potentially superconducting diode effects. Moreover, the ability to control the vertical magnetic domain structure opens new

opportunities to vary the thickness of the FM and AFM tunnel barriers in-situ without much change to the overall thickness of the insulating CrSBr barrier layer. This unique capability may provide a new platform for studying exotic phenomena proposed to emerge in superconductor/ferromagnetic JJs with inhomogeneous magnetization, such as spin triplet correlations.

APPENDIX I: ADDITIONAL INFORMATION FOR CHAPTER 2

AI.1 Reflective Magnetic Circular Dichroism

When light is incident on a magnetic material, the amplitude between reflected right- and left-circularly polarized light can be different. This property is known as magnetic circular dichroism. When linearly polarized light, consisting of equal superposition of right and left circularly polarized components is incident on materials with this property, the reflected and transmitted light become elliptically polarized. In the backscattering geometry, this effect is known as reflective magnetic circular dichroism (RMCD), and it provides a highly sensitive probe of the out-of-plane magnetic moment[21].

The experimental setup our lab most commonly uses to measure RMCD is shown in Figure AI.1a. A laser beam is modulated twice: first by an optical chopper set at ~ 1 kHz, and then a photoelastic modulator (PEM) set to quarter wave modulation at 50 kHz. The incident light reflects off the sample and is then directed into a photodiode by the beamsplitter. The photodiode is connected to two lock-in detectors which read the intensity at the chopper frequency and PEM frequencies, providing a value of the reflected light intensity and the circular dichroism, respectively. To convert the lock-in readings to RMCD, we use[21]:

$$\frac{I_2}{I_1} = AJ_1(\delta_0)\frac{\Delta R}{R}$$

In our setup, we found that A ~ 1, so the RMCD ($\frac{\Delta R}{R}$) is obtained by dividing the PEM reading by the chopper one and the Bessel function of the first kind evaluated at $\frac{\pi}{2}$ (the total retardance). This technique was first used[23] in our lab to study atomically thin CrI_3 flakes (see Fig. AI.1b for a measurement of monolayer CrI_3), and it has become a vital tool in a variety of subsequent discoveries in that system[17,45,64,105,131,179] and many others.

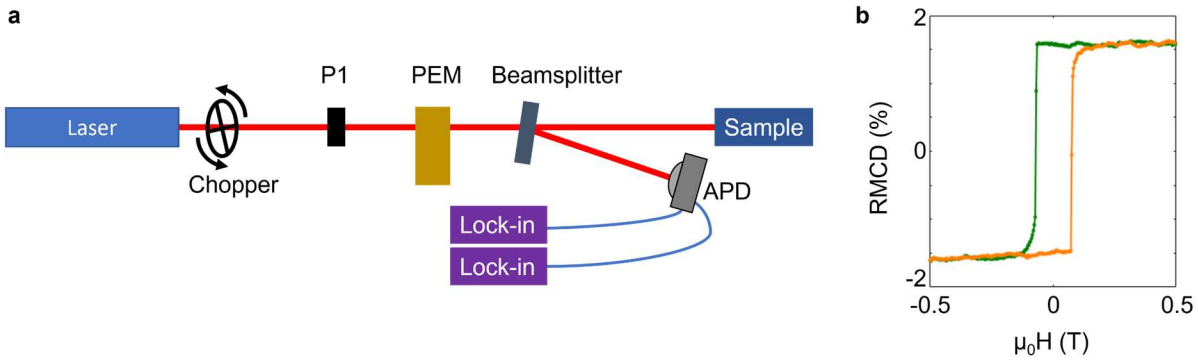

Figure AI.1 | Reflective magnetic circular dichroism measurements. **a,** Diagram of the optics setup for the RMCD measurement. P1 represents a linear polarizer set to 45° with respect to the optical axis of the PEM. **b,** RMCD measurement of monolayer CrI_3. A sharp hysteresis loop, consistent with FM ordering, is observed.

AI.2 Modelling Magnon Dynamics with Landau-Lifshitz-Gilbert Equation

The energy, brightness, and magnetic field dependence of magnons in CrSBr can be understood using the standard Landau-Lifshitz-Gilbert (LLG) treatment. We start with the Hamiltonian of CrSBr which is treated as:

$$H = J_2 \boldsymbol{S_1} \cdot \boldsymbol{S_2} - g\mu_B \boldsymbol{H} \cdot \sum_{i=1,2} \boldsymbol{S}_i - K_b(\boldsymbol{S}_i \cdot \hat{b})^2 + K_a(\boldsymbol{S}_i \cdot \hat{a})^2 + K_c(\boldsymbol{S}_i \cdot \hat{c})^2$$

Where J_2 is the interlayer exchange coupling, the magnitudes of magnetization of adjacent layers are set as $S_1 = S_2 = \frac{3}{2}$, μ_B is the Bohr magneton, g = 2 is the Landé factor, and $\hat{b}$, $\hat{a}$, $\hat{c}$ are the easy, intermediate, and hard axes, respectively. The first term is responsible for the interlayer exchange coupling, the second is the Zeeman energy from an external magnetic field, and the others come from the triaxial magnetic anisotropy. Since shifting the energy of all three anisotropies by a constant value does not affect the spin dynamics, we can choose to set $K_a = 0$, and $K_{b,c} > 0$.

The magnon mode frequencies and dynamics can then be obtained by the LLG equation:

$$\dot{\boldsymbol{s}}_{\boldsymbol{i}} = -\boldsymbol{S}_{\boldsymbol{i}} \times \boldsymbol{H}_{\boldsymbol{i}}$$

where $\boldsymbol{H_i}$ is the effective magnetic field felt by the *i*th spin obtained by taking the derivative of the above Hamiltonian with respect to each macrospin component, i.e. $\boldsymbol{H_i} = \boldsymbol{\nabla_{S_i} H}$. Using linear spin wave theory, we can express $\boldsymbol{S_i} = \boldsymbol{S_i^0} + \boldsymbol{\partial S_i}$ where $\boldsymbol{S_i^0}$ is the equilibrium spin configuration. To ensure a constant magnitude of spin up to second order, we also set $\boldsymbol{S_i^0} \cdot \boldsymbol{\partial S_i} = 0$. First, we will consider what happens when a field is applied directly along the *a* axis. In this case, the spins will cant at an angle θ from the *b* axis which is determined by minimizing the energy of the Hamiltonian. The equilibrium spin states along the (*b*, *a*, and *c*) axes are then $\boldsymbol{S_1^0} = S(\cos(\theta), \sin(\theta), 0)$ and $\boldsymbol{S_2^0} = S(-\cos(\theta), \sin(\theta), 0)$, respectively. Given the restraint that $\boldsymbol{S_i^0} \cdot \boldsymbol{\partial S_i} = 0$, we can set $\boldsymbol{\partial S_1} = \left(-\partial S_1^{||} \cos(\theta), \partial S_1^{||} \sin(\theta), \partial S_1^c\right)$.

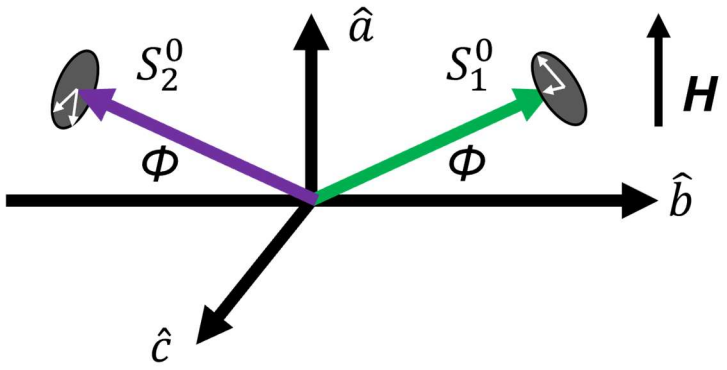

Figure AI.2 | Diagram of magnons in the canted AFM state, when the field is applied directly along the *a* axis.

The LLG then becomes:

$$\frac{d}{dt}\begin{pmatrix} \delta S_1^{||} \\ \delta S_2^{||} \\ \delta S_1^c \\ \delta S_2^c \end{pmatrix} = S\begin{pmatrix} 0 & 0 & J_2 + 2(K_b + K_C) & J_2 \\ 0 & 0 & J_2 & J_2 + 2(K_b + K_C) \\ -(2K_b\, cos^2(\phi) + J_2) & J_2\, cos(2\phi) & 0 & 0 \\ J_2\, cos(2\phi) & -(2K_b\, cos^2(\phi) + J_2) & 0 & 0 \end{pmatrix}\begin{pmatrix} \delta S_1^{||} \\ \delta S_2^{||} \\ \delta S_1^c \\ \delta S_2^c \end{pmatrix}$$

CrSBr has a two-fold rotational symmetry (i.e., C_2) along the *a* axis, which is maintained when the magnetic field is applied along the *a* axis. Consequently, we can decouple the LLG into two sets of equations, which are even and odd under parity operations. This is achieved by applying the unitary transformation:

$$\begin{pmatrix} D^{||} \\ D^{C} \\ B^{||} \\ B^{C} \end{pmatrix} = \frac{1}{\sqrt{2}} \begin{pmatrix} 1 & 1 & 0 & 0 \\ 0 & 0 & 1 & 1 \\ 1 & -1 & 0 & 0 \\ 0 & 0 & 1 & -1 \end{pmatrix} \begin{pmatrix} \delta S_1^{||} \\ \delta S_2^{||} \\ \delta S_1^{c} \\ \delta S_2^{c} \end{pmatrix}$$

Where $D^{||}$ and D^{C} denote even bases and $B^{||}$ and B^{C} are odd under the C_2 rotational symmetry. We learned earlier in Chapter 2 that the odd-parity mode can coherently couple to excitons due to the changing angle between spins through the precession period, while the even mode is optically dark. In these new bases, the LLG equation is expressed as:

$$\frac{d}{dt} \begin{pmatrix} D^{||} \\ D^{C} \\ B^{||} \\ B^{C} \end{pmatrix} = 2S \begin{pmatrix} 0 & (J_2 + K_b + K_C) & 0 & 0 \\ -(K_b\, cos^2(\phi) + J_2\, sin^2(\phi)) & 0 & 0 & 0 \\ 0 & 0 & 0 & (K_b + K_C) \\ 0 & 0 & -(K_b + J_2)\, cos^2(\phi)) & 0 \end{pmatrix} \begin{pmatrix} D^{||} \\ D^{C} \\ B^{||} \\ B^{C} \end{pmatrix}$$

which gives a frequency of $E_D = 2S\sqrt{(J_2 + K_b + K_C) - (K_b\, cos^2(\phi) + J_2\, sin^2(\phi))}$ and $E_B = 2S\sqrt{(K_b + K_C)(K_b + J_2)\, cos^2(\phi))}$ for the dark and bright modes, respectively. In the case of $K_b = J_2$, the dark mode does not depend on ϕ, which corresponds to the dispersionless mode observed in the strained CrSBr sample.

When the in-plane field is applied at a tilted angle, i.e., not along the *a* or *b* axes, the two-fold rotational symmetry of the system is broken. This leads to a mixing of the dark and bright modes. To capture this behavior, we consider what happens when the field has a small component, H_b, along the *b* axis with $H_b << H_a$. Because of this condition, we neglect the influence of H_b on the spin canting. Projecting the torques generated by H_b onto the directions orthogonal to S_1^0 or S_2^0 turns the LLG into:

$$\frac{d}{dt} \begin{pmatrix} D^{||} \\ D^{C} \\ B^{||} \\ B^{C} \end{pmatrix} = 2S \begin{pmatrix} 0 & (J_2 + K_b + K_C) & 0 & f \\ -(K_b\, cos^2(\phi) + J_2\, sin^2(\phi)) & 0 & -f & 0 \\ 0 & f & 0 & (K_b + K_C) \\ -f & 0 & -(K_b + J_2)\, cos^2(\phi)) & 0 \end{pmatrix} \begin{pmatrix} D^{||} \\ D^{C} \\ B^{||} \\ B^{C} \end{pmatrix}$$

where $f = \frac{g\mu_B H_b \cos\phi}{2S}$, giving rise to the coupling between the dark and bright modes.

The LLG equation can then be solved numerically for arbitrary field direction, with the brightness of the modes determined by calculating the change of $S_1(t) \cdot S_2(t)$ over a single period for fixed spin wave amplitudes[48].

AI.3 Magnon Raman scattering in bulk CrI_3

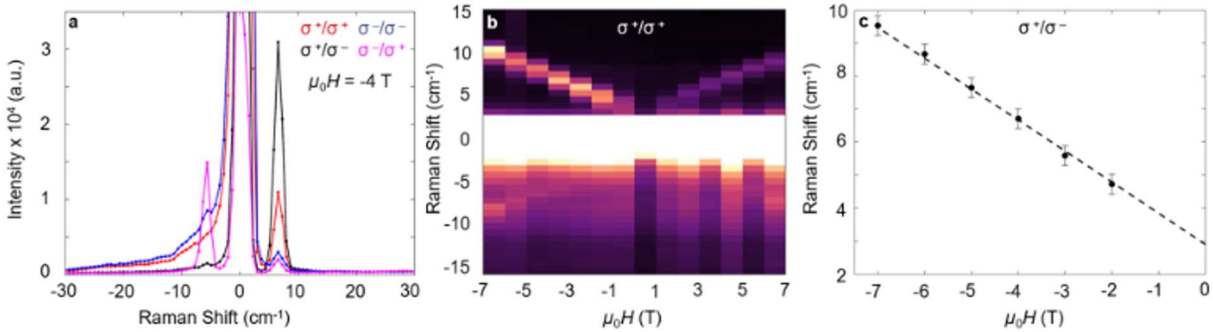

Figure AI.3 | Raman scattering from acoustic magnons in unexfoliated bulk single crystal CrI_3. **a,** Low energy Raman scattering in all circurlarly polarized channels. The signal is still strongest in the cross-circularly polarized channel (black), but a large component appears in the co-circular (σ+/σ+, red) one as well. The relaxation of selection rules in comparison with the atomically thin flakes likely comes from defects and stacking faults in the bulk crystal. **b,** Field-dependent Raman measurements. The linear shift in field confirms the feature is a magnon peak and rules out origins such as acoustic phonons. **c,** The energy of the acoustic magnon as a function of field. The dashed line indicates the expected Zeeman energy shift of a magnon, i.e. a magnetic moment of 2 μ_B, with a zero-field intercept of ~ 2.8 cm^{-1}. Reproduced from Ref. [64]

APPENDIX II: STRAIN CELL AND DEVICE FABRICATION

The basic operating principle of the strain cell was covered in Chapter 4. Here, I will discuss additional important considerations for strain experiments. Three piezoelectric stacks are glued using Stycast 2850FT epoxy to a titanium backing plate (> 2 mm thick) and a flexure element (Figure 4.1-1a). When gluing the strain cell together, it is important to ensure that all piezo stacks are parallel to each other, and perpendicular to the titanium backing plate to ensure proper tensile strain application. The thermal contraction of the symmetrically glued piezostacks negates much of the thermal strain on the sample[149]. However, different contraction coefficients between the titanium plate and the sample can still result in a thermal strain. Often time we will short the wires of the piezostacks together to simplify operation. To ensure proper application of strain, the positive leads of the outer piezo stacks are connected to the black lead of the inner piezo stack. Similarly, the negative leads of the outer piezo stacks are shorted to the positive lead of the inner one. Thus, applying a piezo voltage causes the outer (inner) stacks to expand (contract), as desired.

The piezo stacks have an asymmetric, temperature dependent voltage range. For example, at room temperature, the piezo stacks can be varied from -20 V to 120 V at 300 K, but -200 V to 200 V at -2 K. The full temperature dependence is shown in Figure AII.1. In the shorted configuration, a positive voltage applied to the strain cell corresponds to a negative voltage applied to the inner stack. Therefore, the benefit of simplicity in the shorted configuration comes with the downside of limited functionality at elevated temperatures, with the maximum magnitude of voltage being the negative

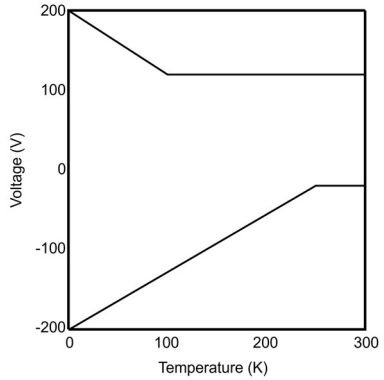

Figure AII.1 | Temperature dependence of operational piezo voltage range

voltage in Fig. AII1. By disconnecting the inner piezo stacks from the outer ones, we can access a larger strain range. In this case, +120 V and -20 V can be applied to the outer stacks and inner stacks, respectively, at room temperature. At low temperature, however, the limit for either wiring configuration is ± 200 V.

The strain cell design was first used to apply strain to bulk crystals, as discussed in the main text. However, the atomically thin nature of 2D materials poses substantial difficulties in strain application. Unlike the bulk samples which are fastened by the same Stycast Epoxy, 2D samples are attached using van der Waals forces. To apply strain to these samples, we developed techniques based on both suspended samples and flexible substrates. The suspended samples were made in the following way: a piece of thin silicon is first glued across the gap of the strain cell or flexure sample plate, and then fractured using a diamond scribe (Figure AII.2a). The resulting gap is on the order of ~ 5 μm, and nearly height uniform, which can be checked by confirming both sides are in focus when viewed under a 100x microscope objective. This is crucial for successful deposition of the sample across the gap. Another vital factor is the transfer method. We found that the easiest way is by exfoliating on polydimethylsiloxane, and then simply dropping the flake across the gap using standard transfer techniques, i.e., a motorized arm is used to raise and lower a stamp with the PDMS block, while an optical microscope is used for alignment (Figure AII.2b). Polypropylene carbonate (PPC) and polycarbonate (PC) stamps can also be used. A drop-off temperature of ~ 90° is used for PPC stamps, and a melt-down temperature of ~ 180° C is used for PC. When removing the left-over PC polymer, we found it was useful to dip the sample in hexane before drying as the high surface tension of chloroform and isopropanol can be disruptive to the suspended flake.

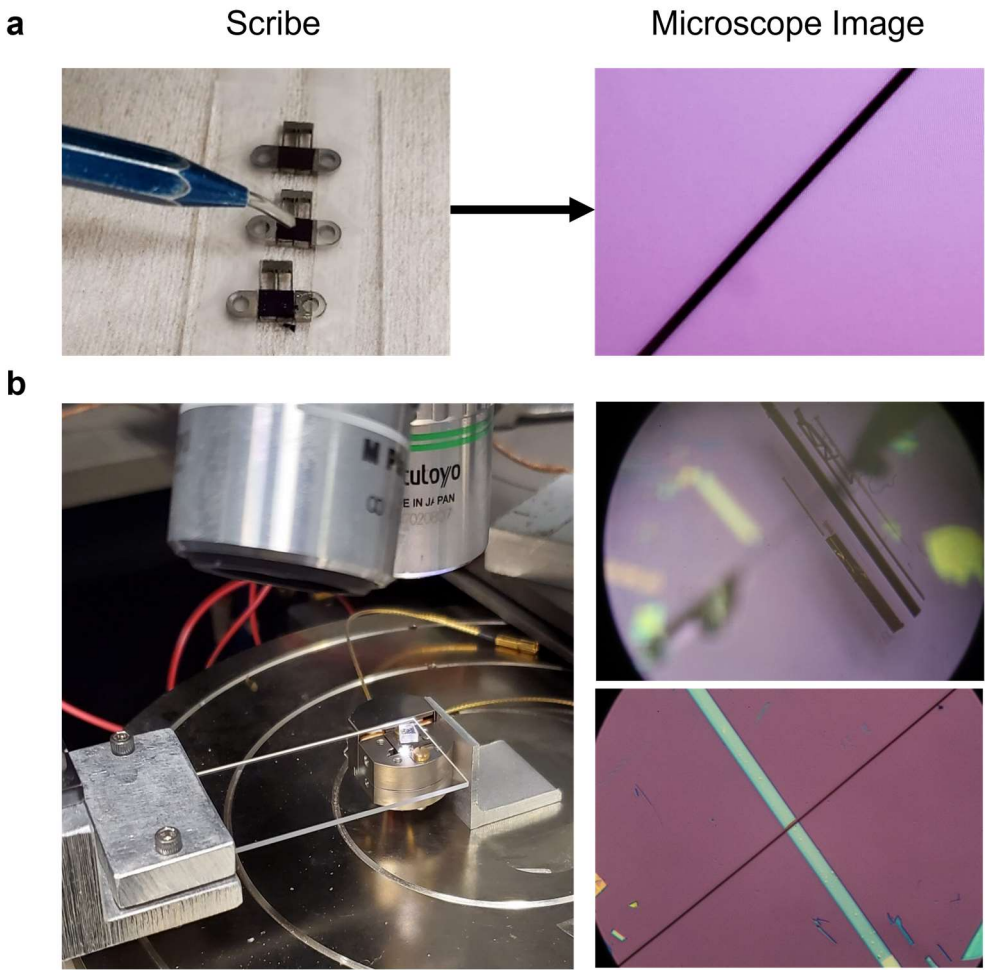

Figure AII2 | Fabrication procedure for creating small gaps in Si substrates (**a**) and suspending sample across it (**b**).

In contrast to the suspended samples which require very careful fabrication procedures, the polyimide-based samples are far more compatible with more conventional 2D fabrication techniques. The notable differences between polyimide and silicon include needing to use spin-coated conductive layers to do electron beam lithography on the insulating polyimide substrate, and shorter PC wash off times (typically ~ 3-5 minutes) to limit the substrate swelling due to the solvent exposure.

APPENDIX III: ADDITIONAL DATA FOR CHAPTER 6

AIII.1 Tunneling magnetoresistance sweeps at select strain voltages

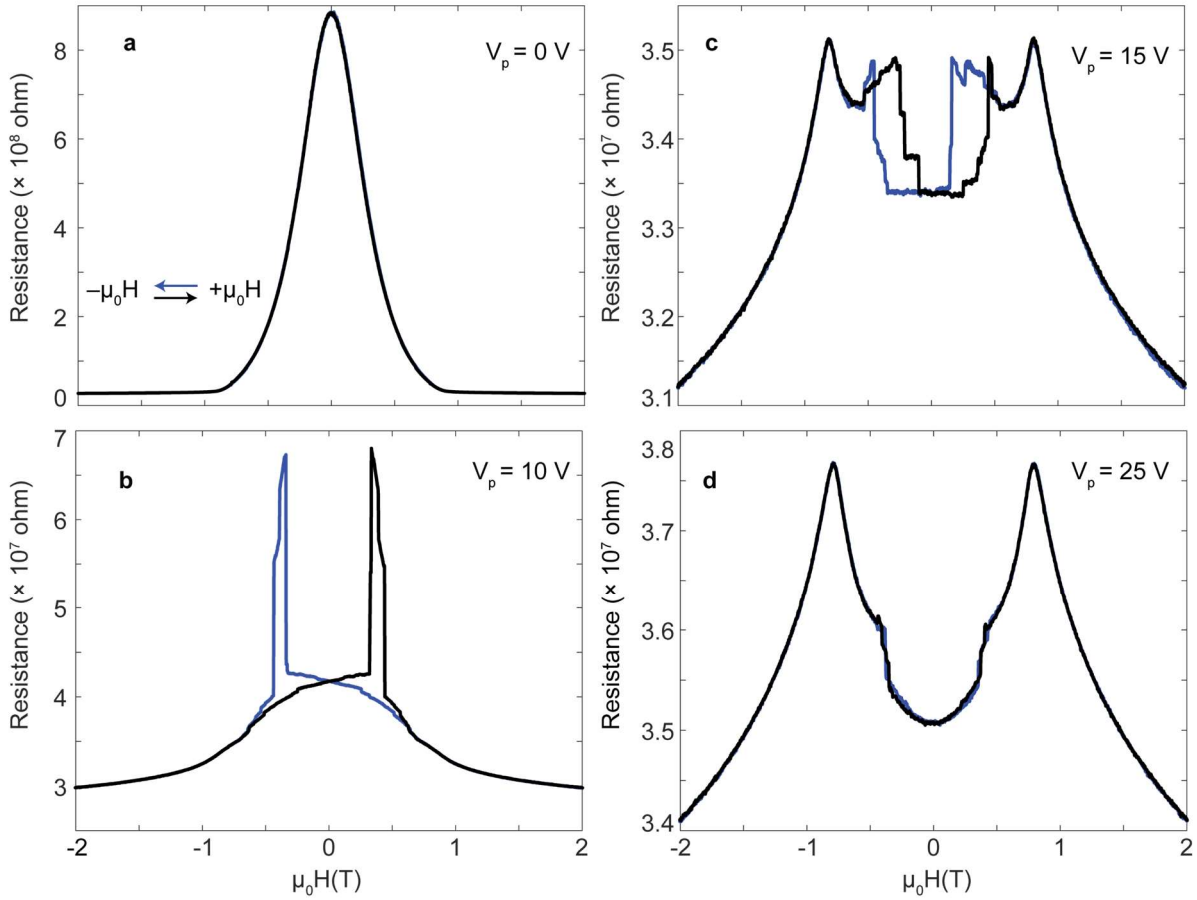

Figure AIII.1 | Complicated domain behavior during the strain-induced magnetic phase transition**. a-d,** TMR sweeps with the field swept down (blue) and up (black) at select strains. At low piezo voltage and strain (**a**), a large negative TMR is observed, consistent with the A-type AFM order, while small positive TMR is observed in the high strain FM state (**d**). In between, complicated, hysteretic magnetic domain behavior is observed. Adapted from Ref. 182

AIII.2 Strain pulse measurements in the totally AFM and FM states

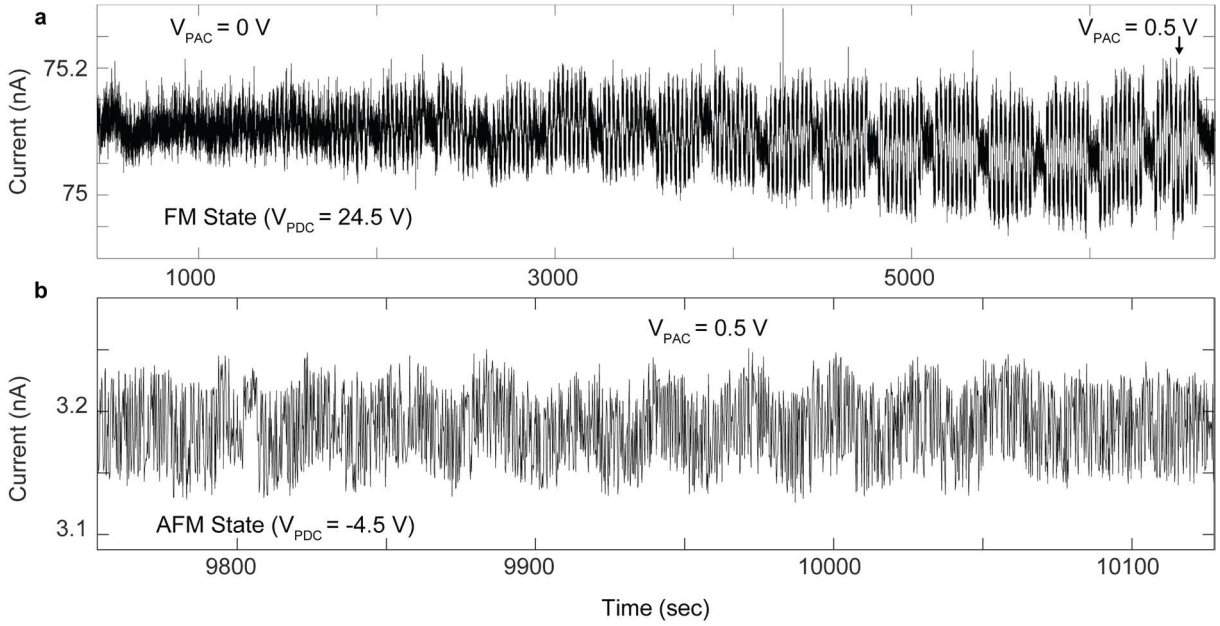

Figure AIII.2 | Strain pulse measurements in the purely FM and AFM states. **a,** Strain pulse amplitude dependence from 0 to 0.5 V in the high-strain FM state. A continuous change with a gauge factor of ~ 5 is measured. **b,** A single pulse with amplitude of 0.5 V applied in the low-strain AFM phase. Because of the low current, this is the smallest pulse amplitude that resulted in measurable changes. No distinct jumps into stable levels or changes to the static tunneling current are observed in either FM or AFM states. Adapted from Ref. [182]

BIBLIOGRAPHY

1 Novoselov, K. S. *et al.* Electric field effect in atomically thin carbon films. *Science* **306**, 666-669 (2004). https://doi.org/10.1126/science.1102896

2 Geim, A. K. & Grigorieva, I. V. Van der Waals heterostructures. *Nature* **499**, 419-425 (2013). https://doi.org/10.1038/nature12385

3 Novoselov, K. S., Mishchenko, A., Carvalho, A. & Castro Neto, A. H. 2D materials and van der Waals heterostructures. *Science* **353**, aac9439 (2016). https://doi.org/10.1126/science.aac9439

4 Peng, Z., Chen, X., Fan, Y., Srolovitz, D. J. & Lei, D. Strain engineering of 2D semiconductors and graphene: from strain fields to band-structure tuning and photonic applications. *Light: Science & Applications* **9** (2020). https://doi.org/10.1038/s41377-020-00421-5

5 Yang, S., Chen, Y. & Jiang, C. Strain engineering of two‐dimensional materials: Methods, properties, and applications. *InfoMat* **3**, 397-420 (2021). https://doi.org/10.1002/inf2.12177

6 Qi, Y. *et al.* Recent Progress in Strain Engineering on Van der Waals 2D Materials: Tunable Electrical, Electrochemical, Magnetic, and Optical Properties. *Advanced Materials* **35**, 2205714 (2023). https://doi.org/10.1002/adma.202205714

7 Pei, S., Wang, Z. & Xia, J. High pressure studies of 2D materials and heterostructures: A review. *Materials & Design* **213** (2022).

8 Zhang, L. *et al.* 2D Materials and Heterostructures at Extreme Pressure. *Advanced Science* **7**, 2002697 (2020). https://doi.org/10.1002/advs.202002697

9 Martins, L. G. P. *et al.* High-pressure studies of atomically thin van der Waals materials. *Applied Physics Reviews* **10** (2023).

10 Wu, Y., Li, D., Wu, C.-L., Hwang, H. Y. & Cui, Y. Electrostatic gating and intercalation in 2D materials. *Nature Reviews Materials* **8**, 41-53 (2022). https://doi.org/10.1038/s41578-022-00473-6

11 Nguyen, P. V. *et al.* Visualizing electrostatic gating effects in two-dimensional heterostructures. *Nature* **572**, 220-223 (2019). https://doi.org/10.1038/s41586-019-1402-1

12 Zhang, Y., Tan, Y.-W., Stormer, H. L. & Kim, P. Experimental observation of the quantum Hall effect and Berry's phase in graphene. *Nature* **438**, 201-204 (2005). https://doi.org/10.1038/nature04235

13 Huang, B. *et al.* Emergent phenomena and proximity effects in two-dimensional magnets and heterostructures. *Nature Materials* **19**, 1276-1289 (2020). https://doi.org/10.1038/s41563-020-0791-8

14 Zhong, D. *et al.* Layer-resolved magnetic proximity effect in van der Waals heterostructures. *Nature Nanotechnology* **15**, 187-191 (2020). https://doi.org/10.1038/s41565-019-0629-1

15 Zhao, W. *et al.* Magnetic proximity and nonreciprocal current switching in a monolayer WTe_2 helical edge. *Nature Materials* **19**, 503-507 (2020). https://doi.org/10.1038/s41563-020-0620-0

16 Andrei, E. Y. *et al.* The marvels of moiré materials. *Nature Reviews Materials* **6**, 201-206 (2021). https://doi.org/10.1038/s41578-021-00284-1

17 Song, T. *et al.* Direct visualization of magnetic domains and moiré magnetism in twisted 2D magnets. *Science* **374**, 1140-1144 (2021). https://doi.org/doi:10.1126/science.abj7478

18 Wang, P. *et al.* One-dimensional Luttinger liquids in a two-dimensional moiré lattice. *Nature* **605**, 57-62 (2022). https://doi.org/10.1038/s41586-022-04514-6

19 Xu, Y. *et al.* Correlated insulating states at fractional fillings of moiré superlattices. *Nature* **587**, 214-218 (2020). https://doi.org/10.1038/s41586-020-2868-6

20 Cao, Y. *et al.* Unconventional superconductivity in magic-angle graphene superlattices. *Nature* **556**, 43-50 (2018). https://doi.org/10.1038/nature26160

21 Sato, K. Measurement of Magneto-Optical Kerr Effect Using Piezo-Birefringent Modulator. *Japanese Journal of Applied Physics* **20**, 2403-2409 (1981). https://doi.org/10.1143/jjap.20.2403

22 Gong, C. *et al.* Discovery of intrinsic ferromagnetism in two-dimensional van der Waals crystals. *Nature* **546**, 265-269 (2017). https://doi.org/10.1038/nature22060

23 Huang, B. *et al.* Layer-dependent ferromagnetism in a van der Waals crystal down to the monolayer limit. *Nature* **546**, 270-273 (2017). https://doi.org/10.1038/nature22391

24 Shcherbakov, D. *et al.* Raman Spectroscopy, Photocatalytic Degradation, and Stabilization of Atomically Thin Chromium Tri-iodide. *Nano Letters* **18**, 4214-4219 (2018). https://doi.org/10.1021/acs.nanolett.8b01131

25 Xi, X. *et al.* Ising pairing in superconducting $NbSe_2$ atomic layers. *Nature Physics* **12**, 139-143 (2016). https://doi.org/10.1038/nphys3538

26 Gibertini, M., Koperski, M., Morpurgo, A. F. & Novoselov, K. S. Magnetic 2D materials and heterostructures. *Nature Nanotechnology* **14**, 408-419 (2019). https://doi.org/10.1038/s41565-019-0438-6

27 Gong, C. & Zhang, X. Two-dimensional magnetic crystals and emergent heterostructure devices. *Science* **363** (2019). https://doi.org/10.1126/science.aav4450

28 Burch, K. S., Mandrus, D. & Park, J.-G. Magnetism in two-dimensional van der Waals materials. *Nature* **563**, 47-52 (2018). https://doi.org/10.1038/s41586-018-0631-z

29 Mutch, J. *et al.* Evidence for a strain-tuned topological phase transition in $ZrTe_5$. *Science Advances* **5**, eaav9771 (2019). https://doi.org/10.1126/sciadv.aav9771

30 Lin, C. *et al.* Visualization of the strain-induced topological phase transition in a quasi-one-dimensional superconductor $TaSe_3$. *Nature Materials* **20**, 1093-1099 (2021). https://doi.org/10.1038/s41563-021-01004-4

31 Malinowski, P. *et al.* Suppression of superconductivity by anisotropic strain near a nematic quantum critical point. *Nature Physics* **16**, 1189-1193 (2020). https://doi.org/10.1038/s41567-020-0983-9

32 Hicks, C. W. *et al.* Strong Increase of T_c of Sr_2RuO_4 Under Both Tensile and Compressive Strain. *Science* **344**, 283-285 (2014). https://doi.org/10.1126/science.1248292

33 Zhang, H. *et al.* Comprehensive Electrical Control of Metamagnetic Transition of a Quasi‐2D Antiferromagnet by In Situ Anisotropic Strain. *Advanced Materials* **32**, 2002451 (2020). https://doi.org/10.1002/adma.202002451

34 Ceballos, A. *et al.* Effect of strain and thickness on the transition temperature of epitaxial FeRh thin-films. *Applied Physics Letters* **111**, 172401 (2017). https://doi.org/10.1063/1.4997901

35 Fontana, J. & Palffy-Muhoray, P. St. Petersburg Paradox and Failure Probability. *Physical Review Letters* **124** (2020). https://doi.org/10.1103/physrevlett.124.245501

36 Lee, C., Wei, X., Kysar, J. W. & Hone, J. Measurement of the Elastic Properties and Intrinsic Strength of Monolayer Graphene. *Science* **321**, 385-388 (2008). https://doi.org/10.1126/science.1157996

37 Bertolazzi, S., Brivio, J. & Kis, A. Stretching and Breaking of Ultrathin MoS_2. *ACS Nano* **5**, 9703-9709 (2011). https://doi.org/10.1021/nn203879f

38 Wang, L. *et al.* In Situ Strain Tuning in hBN-Encapsulated Graphene Electronic Devices. *Nano Letters* **19**, 4097-4102 (2019). https://doi.org/10.1021/acs.nanolett.9b01491

39 Huang, M. *et al.* Phonon softening and crystallographic orientation of strained graphene studied by Raman spectroscopy. *Proceedings of the National Academy of Sciences* **106**, 7304-7308 (2009). https://doi.org/10.1073/pnas.0811754106

40 Wang, Y. *et al.* Strain‐Sensitive Magnetization Reversal of a van der Waals Magnet. *Advanced Materials* **32**, 2004533 (2020). https://doi.org/10.1002/adma.202004533

41 Gong, L. *et al.* Optimizing the Reinforcement of Polymer-Based Nanocomposites by Graphene. *ACS Nano* **6**, 2086-2095 (2012). https://doi.org/10.1021/nn203917d

42 Androulidakis, C. *et al.* Strained hexagonal boron nitride: Phonon shift and Grüneisen parameter. *Physical Review B* **97** (2018). https://doi.org/10.1103/physrevb.97.241414

43 Edelberg, D., Kumar, H., Shenoy, V., Ochoa, H. & Pasupathy, A. N. Tunable strain soliton networks confine electrons in van der Waals materials. *Nature Physics* **16**, 1097-1102 (2020). https://doi.org/10.1038/s41567-020-0953-2

44 Kumar, H., Dong, L. & Shenoy, V. B. Limits of Coherency and Strain Transfer in Flexible 2D van der Waals Heterostructures: Formation of Strain Solitons and Interlayer Debonding. *Scientific Reports* **6**, 21516 (2016). https://doi.org/10.1038/srep21516

45 Huang, B. *et al.* Tuning inelastic light scattering via symmetry control in the two-dimensional magnet CrI_3. *Nature Nanotechnology* **15**, 212-216 (2020). https://doi.org/10.1038/s41565-019-0598-4

46 Lee, J.-U. *et al.* Ising-Type Magnetic Ordering in Atomically Thin $FePS_3$. *Nano Letters* **16**, 7433-7438 (2016). https://doi.org/10.1021/acs.nanolett.6b03052

47 Bae, Y. J. *et al.* Exciton-coupled coherent magnons in a 2D semiconductor. *Nature* **609**, 282-286 (2022). https://doi.org/10.1038/s41586-022-05024-1

48 Diederich, G. M. *et al.* Tunable interaction between excitons and hybridized magnons in a layered semiconductor. *Nature Nanotechnology* **18**, 23-28 (2023). https://doi.org/10.1038/s41565-022-01259-1

49 Žutić, I., Fabian, J. & Das Sarma, S. Spintronics: Fundamentals and applications. *Reviews of Modern Physics* **76**, 323-410 (2004). https://doi.org/10.1103/revmodphys.76.323

50 Dietl, T. & Ohno, H. Dilute ferromagnetic semiconductors: Physics and spintronic structures. *Reviews of Modern Physics* **86**, 187-251 (2014). https://doi.org/10.1103/revmodphys.86.187

51 Prinz, G. A. Magnetoelectronics. *Science* **282**, 1660-1663 (1998). https://doi.org/10.1126/science.282.5394.1660

52 Ohno, H. Making Nonmagnetic Semiconductors Ferromagnetic. *Science* **281**, 951-956 (1998). https://doi.org/10.1126/science.281.5379.951

53 Datta, S. & Das, B. Electronic analog of the electro‐optic modulator *Appl. Phys. Lett.* **56**, 665-667 (1990).

54 Ohno, Y. *et al.* Electrical spin injection in a ferromagnetic semiconductor heterostructure. *Nature* **402**, 790-792 (1999). https://doi.org/10.1038/45509

55 Bhattacharya, M. H. a. P. Spin-polarized light-emitting diodes and lasers. *Journal of Physics D: Applied Physics* **40**, R179 (2007). https://doi.org/10.1088/0022-3727/40/11/R01

56 Pulizzi, F. Is it really intrinsic ferromagnetism? *Nature Materials* **9**, 956-957 (2010). https://doi.org/10.1038/nmat2905

57 Chhowalla, M., Jena, D. & Zhang, H. Two-dimensional semiconductors for transistors. *Nature Reviews Materials* **1**, 16052 (2016). https://doi.org/10.1038/natrevmats.2016.52

58 Xiao, J., Zhao, M., Wang, Y. & Zhang, X. Excitons in atomically thin 2D semiconductors and their applications. *Nanophotonics* **6**, 1309-1328 (2017). https://doi.org/10.1515/nanoph-2016-0160

59 Wilson, N. P., Yao, W., Shan, J. & Xu, X. Excitons and emergent quantum phenomena in stacked 2D semiconductors. *Nature* **599**, 383-392 (2021). https://doi.org/10.1038/s41586-021-03979-1

60 Telford, E. J. *et al.* Layered Antiferromagnetism Induces Large Negative Magnetoresistance in the van der Waals Semiconductor CrSBr. *Advanced Materials* **32**, 2003240 (2020). https://doi.org/10.1002/adma.202003240

61 Lee, K. *et al.* Magnetic Order and Symmetry in the 2D Semiconductor CrSBr. *Nano Lett.* **21**, 3511-3517 (2021).

62 Telford, E. J. *et al.* Coupling between magnetic order and charge transport in a two-dimensional magnetic semiconductor. *Nature Materials* **21**, 754-760 (2022). https://doi.org/10.1038/s41563-022-01245-x

63 Wilson, N. P., Lee, K., Cenker, J. *et al.* Interlayer Electronic Coupling on Demand in a 2D Magnetic Semiconductor. *Nat. Mater.* **20**, 1657-1662 (2021).

64 Cenker, J., B. Huang, *et al.* Direct observation of two-dimensional magnons in atomically thin CrI_3. *Nature Physics* **17**, 20-25 (2021). https://doi.org/10.1038/s41567-020-0999-1

65 Göser, O., Paul, W. & Kahle, H. G. Magnetic properties of CrSBr. *Journalism of Magnetism and Magnetic Materials* **92**, 129-136 (1990).

66 Deng, Y. *et al.* Quantum anomalous Hall effect in intrinsic magnetic topological insulator $MnBi_2Te_4$. *Science* **367**, 895-900 (2020). https://doi.org/doi:10.1126/science.aax8156

67 Ovchinnikov, D. *et al.* Intertwined Topological and Magnetic Orders in Atomically Thin Chern Insulator $MnBi_2Te_4$. *Nano Letters* **21**, 2544-2550 (2021). https://doi.org/10.1021/acs.nanolett.0c05117

68 Son, J. *et al.* Air-Stable and Layer-Dependent Ferromagnetism in Atomically Thin van der Waals $CrPS_4$. *ACS Nano* **15**, 16904-16912 (2021). https://doi.org/10.1021/acsnano.1c07860

69 Yang, K., Wang, G., Liu, L., Lu, D. & Wu, H. Triaxial magnetic anisotropy in the two-dimensional ferromagnetic semiconductor CrSBr. *Physical Review B* **104** (2021). https://doi.org/10.1103/physrevb.104.144416

70 Wang, H., Qi, J. & Qian, X. Electrically tunable high Curie temperature two-dimensional ferromagnetism in van der Waals layered crystals. *Applied Physics Letters* **117**, 083102 (2020). https://doi.org/10.1063/5.0014865

71 Junjiro, K. Superexchange interaction and symmetry properties of electron orbitals. *Journal of Physics and Chemistry of Solids* **10**, 87-98 (1959). https://doi.org/https://doi.org/10.1016/0022-3697(59)90061-7

72 John B. Goodenough. Magnetism and the Chemical Bond. New York, London. (Interscience Publishers, 1963).

73 Anderson, P. W. New Approach to the Theory of Superexchange Interactions. *Physical Review* **115**, 2-13 (1959). https://doi.org/10.1103/physrev.115.2

74 Cenker, J. *et al.* Reversible strain-induced magnetic phase transition in a van der Waals magnet. *Nature Nanotechnology* **17**, 256-261 (2022). https://doi.org/10.1038/s41565-021-01052-6

75 Selbmann, P.E., Gulia, M., Rossie, F., Molinari, E., Lugli, P. (1996). Dynamics of Exciton Formation and Relaxation in Semiconductors. *In: Hess, K., Leburton, JP., Ravaioli, U. (eds) Hot Carriers in Semiconductors*. Springer, Boston, MA. https://doi.org/10.1007/978-1-4613-0401-2_5

76 Wang, G. *et al.* Colloquium: Excitons in atomically thin transition metal dichalcogenides. *Reviews of Modern Physics* **90** (2018). https://doi.org/10.1103/revmodphys.90.021001

77 Tang, Y. *et al.* Simulation of Hubbard model physics in WSe_2/WS_2 moiré superlattices. *Nature* **579**, 353-358 (2020). https://doi.org/10.1038/s41586-020-2085-3

78 Huang, X. *et al.* Correlated insulating states at fractional fillings of the WS_2/WSe_2 moiré lattice. *Nature Physics* **17**, 715-719 (2021). https://doi.org/10.1038/s41567-021-01171-w

79 Wang, X. *et al.* Light-induced ferromagnetism in moiré superlattices. *Nature* **604**, 468-473 (2022). https://doi.org/10.1038/s41586-022-04472-z

80 Anderson, E. *et al.* Programming correlated magnetic states with gate-controlled moiré geometry. *Science* **381**, 325-330 (2023). https://doi.org/doi:10.1126/science.adg4268

81 Tang, Y. *et al.* Evidence of frustrated magnetic interactions in a Wigner–Mott insulator. *Nature Nanotechnology* **18**, 233-237 (2023). https://doi.org/10.1038/s41565-022-01309-8

82 Zeng, Y. *et al.* Thermodynamic evidence of fractional Chern insulator in moiré $MoTe_2$. *Nature* (2023). https://doi.org/10.1038/s41586-023-06452-3

83 Cai, J. *et al.* Signatures of Fractional Quantum Anomalous Hall States in Twisted $MoTe_2$. *Nature* (2023). https://doi.org/10.1038/s41586-023-06289-w

84 Michael, K. L. M. *et al*. Experimental measurement of the intrinsic excitonic wave function. *Science Advances* **7**, eabg0192 (2021). https://doi.org/10.1126/sciadv.abg0192.

85 Stier, A. V. *et al.* Magnetooptics of Exciton Rydberg States in a Monolayer Semiconductor. *Physical Review Letters* **120** (2018). https://doi.org/10.1103/physrevlett.120.057405

86 Seyler, K. L. *et al.* Ligand-field helical luminescence in a 2D ferromagnetic insulator. *Nature Physics* **14**, 277-281 (2018). https://doi.org/10.1038/s41567-017-0006-7

87 Sun, Z. *et al.* Giant nonreciprocal second-harmonic generation from antiferromagnetic bilayer CrI_3. *Nature* **572**, 497-501 (2019). https://doi.org/10.1038/s41586-019-1445-3

88 Messiah, A. *Quantum Mechanics*. (John Wiley & Sons, 1966).

89 Girvin, S. M. & Yang, K. *Modern Condensed Matter Physics*. (Cambridge University Press, 2019).

90 Simon, S. H. *The Oxford solid state basics*. (Oxford University Press, 2013).

91 Van Kranendonk, J. & Van Vleck, J. H. Spin Waves. *Reviews of Modern Physics* **30**, 1-23 (1958). https://doi.org/10.1103/revmodphys.30.1

92 Fleury, P. A. & Loudon, R. Scattering of Light by One- and Two-Magnon Excitations. *Physical Review* **166**, 514-530 (1968). https://doi.org/10.1103/physrev.166.514

93 Heisenberg, W. Zur Theorie des Ferromagnetismus. *Zeitschrift für Physik* **49**, 619-636 (1928). https://doi.org/10.1007/BF01328601

94 Chumak, A. V. in *Spintronics Handbook, Second Edition: Spin Transport and Magnetism*. Volume One: Metallic Spintronics (eds Evgeny Y. Tsymbal & Igor Žutić) (2019).

95 Chumak, A. V., Vasyuchka, I., V., Serga, A., A. & Hillebrands, B. Magnon spintronics. *Nature Physics* **11**, 453-461 (2015). https://doi.org/10.1038/nphys3347

96 Chumak, A. V., Serga, A. A. & Hillebrands, B. Magnon transistor for all-magnon data processing. *Nature Communications* **5**, 4700 (2014). https://doi.org/10.1038/ncomms5700

97 Neusser, S. & Grundler, D. Magnonics: Spin Waves on the Nanoscale. *Advanced Materials* **21**, 2927-2932 (2009). https://doi.org/10.1002/adma.200900809

98 Serga, A. A., Chumak, A. V., and Hillebrands, B. YIG magnonics. *Journal of Physics D: Applied Physics* **43**, 264002 (2010). https://doi.org/10.1088/0022-3727/43/26/264002

99 Wang, Q. H. *et al.* The Magnetic Genome of Two-Dimensional van der Waals Materials. *ACS Nano* **16**, 6960-7079 (2022). https://doi.org/10.1021/acsnano.1c09150

100 Klein, D. R. *et al.* Probing magnetism in 2D van der Waals crystalline insulators via electron tunneling. *Science* **360**, 1218-1222 (2018). https://doi.org/10.1126/science.aar3617

101 Chen, L. *et al.* Topological Spin Excitations in Honeycomb Ferromagnet CrI_3. *Physical Review X* **8** (2018). https://doi.org/10.1103/physrevx.8.041028

102 Scheie, A. *et al.* Spin Waves and Magnetic Exchange Hamiltonian in CrSBr. *Advanced Science* **9**, 2202467 (2022). https://doi.org/10.1002/advs.202202467

103 Cham, T. M. J. *et al.* Anisotropic Gigahertz Antiferromagnetic Resonances of the Easy-Axis van der Waals Antiferromagnet CrSBr. *Nano Letters* **22**, 6716-6723 (2022). https://doi.org/10.1021/acs.nanolett.2c02124

104 Macneill, D. *et al.* Gigahertz Frequency Antiferromagnetic Resonance and Strong Magnon-Magnon Coupling in the Layered Crystal $CrCl_3$. *Physical Review Letters* **123** (2019). https://doi.org/10.1103/physrevlett.123.047204

105 Wang, Z. *et al.* Very large tunneling magnetoresistance in layered magnetic semiconductor CrI_3. *Nature Communications* **9** (2018). https://doi.org/10.1038/s41467-018-04953-8

106 Song, T. *et al.* Giant tunneling magnetoresistance in spin-filter van der Waals heterostructures. *Science* **360**, 1214-1218 (2018). https://doi.org/10.1126/science.aar4851

107 Wang, Z. *et al.* Determining the phase diagram of atomically thin layered antiferromagnet $CrCl_3$. *Nature Nanotechnology* **14**, 1116-1122 (2019). https://doi.org/10.1038/s41565-019-0565-0

108 Cottam, M. G. & Lockwood, D. J. *Light scattering in magnetic solids*. (Wiley, 1986).

109 Mccreary, A. *et al.* Quasi-two-dimensional magnon identification in antiferromagnetic $FePS_3$. *Physical Review B* **101** (2020). https://doi.org/10.1103/physrevb.101.064416

110 Fernández-Rossier, J. L. L. a. J. On the origin of magnetic anisotropy in two dimensional CrI_3. *2D Materials* **4**, 035002 (2017). https://doi.org/10.1088/2053-1583/aa75ed

111 Lee, I. *et al.* Fundamental Spin Interactions Underlying the Magnetic Anisotropy in the Kitaev Ferromagnet CrI_3. *Physical Review Letters* **124** (2020). https://doi.org/10.1103/physrevlett.124.017201

112 Hisatomi, R. *et al.* Helicity-Changing Brillouin Light Scattering by Magnons in a Ferromagnetic Crystal. *Physical Review Letters* **123** (2019). https://doi.org/10.1103/physrevlett.123.207401

113 Higuchi, T., Kanda, N., Tamaru, H. & Kuwata-Gonokami, M. Selection Rules for Light-Induced Magnetization of a Crystal with Threefold Symmetry: The Case of Antiferromagnetic NiO. *Physical Review Letters* **106** (2011). https://doi.org/10.1103/physrevlett.106.047401

114 Keffer, F. & Kittel, C. Theory of Antiferromagnetic Resonance. *Physical Review* **85**, 329-337 (1952). https://doi.org/10.1103/physrev.85.329

115 Prinz, G. A. Spin - Polarized Transport. *Physics Today* **48**, 58-63 (1995). https://doi.org/10.1063/1.881459

116 Jedema, F. J., Filip, A. T. & Van Wees, B. J. Electrical spin injection and accumulation at room temperature in an all-metal mesoscopic spin valve. *Nature* **410**, 345-348 (2001). https://doi.org/10.1038/35066533

117 Gould, C. *et al.* Tunneling Anisotropic Magnetoresistance: A Spin-Valve-Like Tunnel Magnetoresistance Using a Single Magnetic Layer. *Physical Review Letters* **93** (2004). https://doi.org/10.1103/physrevlett.93.117203

118 Baibich, M. N. *et al.* Giant Magnetoresistance of (001)Fe/(001)Cr Magnetic Superlattices. *Physical Review Letters* **61**, 2472-2475 (1988). https://doi.org/10.1103/physrevlett.61.2472

119 Parkin, S. S. P. *et al.* Giant tunnelling magnetoresistance at room temperature with MgO (100) tunnel barriers. *Nature Materials* **3**, 862-867 (2004). https://doi.org/10.1038/nmat1256

120 Julliere, M. Tunneling between ferromagnetic films. *Physics Letters A.* **54**, 225 (1975).

121 Behin-Aein, B., Datta, D., Salahuddin, S. & Datta, S. Proposal for an all-spin logic device with built-in memory. *Nature Nanotechnology* **5**, 266-270 (2010). https://doi.org/10.1038/nnano.2010.31

122 Dieny, B. *et al.* Chapter Two- Spintronic Devices for Memory and Logic Applications. Vol. 19 (ed K. H. J. Buschow) 107-127 (Elsevier, 2011).

123 Kim, H. H. *et al.* One Million Percent Tunnel Magnetoresistance in a Magnetic van der Waals Heterostructure. *Nano Letters* **18**, 4885-4890 (2018). https://doi.org/10.1021/acs.nanolett.8b01552

124 Cai, X. *et al.* Atomically Thin $CrCl_3$: An In-Plane Layered Antiferromagnetic Insulator. *Nano Letters* **19**, 3993-3998 (2019). https://doi.org/10.1021/acs.nanolett.9b01317

125 Allain, A., Kang, J., Banerjee, K. & Kis, A. Electrical contacts to two-dimensional semiconductors. *Nature Materials* **14**, 1195-1205 (2015). https://doi.org/10.1038/nmat4452

126 Shen, P.-C. *et al.* Ultralow contact resistance between semimetal and monolayer semiconductors. *Nature* **593**, 211-217 (2021). https://doi.org/10.1038/s41586-021-03472-9

127 Yue Zheng and Jing Gao and Cheng Han and Wei, C. Ohmic Contact Engineering for Two-Dimensional Materials. *Cell Reports Physical Science* **2**, 100298 (2021). https://doi.org/https://doi.org/10.1016/j.xcrp.2020.100298

128 López-Paz, S. A. *et al.* Dynamic magnetic crossover at the origin of the hidden-order in van der Waals antiferromagnet CrSBr. *Nature Communications* **13** (2022). https://doi.org/10.1038/s41467-022-32290-4

129 Shklovskii, B. I. & Efros, A. L. *Electronic Properties of Doped Semiconductors*. (Springer, 1984).

130 Efros, A. L., Shklovskii, B. I. Coulomb gap and low temperature conductivity of disordered systems. *Journal of Physics C: Solid State Physics* **8**, L49 (1975). https://doi.org/10.1088/0022-3719/8/4/003

131 Huang, B. *et al.* Electrical control of 2D magnetism in bilayer CrI_3. *Nature Nanotechnology* **13**, 544-548 (2018). https://doi.org/10.1038/s41565-018-0121-3

132 Jiang, S., Li, L., Wang, Z., Mak, K. F. & Shan, J. Controlling magnetism in 2D CrI_3 by electrostatic doping. *Nature Nanotechnology* **13**, 549-553 (2018). https://doi.org/10.1038/s41565-018-0135-x

133 Mukherjee, D., Dhakal, T., Srikanth, H., Mukherjee, P. & Witanachchi, S. Evidence for carrier-mediated magnetism in Mn-doped ZnO thin films. *Physical Review B* **81** (2010). https://doi.org/10.1103/physrevb.81.205202

134 Coey, J. M. D., Venkatesan, M. & Fitzgerald, C. B. Donor impurity band exchange in dilute ferromagnetic oxides. *Nature Materials* **4**, 173-179 (2005). https://doi.org/10.1038/nmat1310

135 Kittilstved, K. R., Liu, W. K. & Gamelin, D. R. Electronic structure origins of polarity-dependent high-T_C ferromagnetism in oxide-diluted magnetic semiconductors. *Nature Materials* **5**, 291-297 (2006). https://doi.org/10.1038/nmat1616

136 Liu, L. & Liu, J. T. C. Theory of the bound magnetic polaron in antiferromagnetic semiconductors. *Physical Review B* **33**, 1797-1803 (1986). https://doi.org/10.1103/physrevb.33.1797

137 Mauger, A. Magnetic polaron: Theory and experiment. *Physical Review B* **27**, 2308-2324 (1983). https://doi.org/10.1103/physrevb.27.2308

138 Jansson, F. *et al.* Large positive magnetoresistance effects in the dilute magnetic semiconductor (Zn,Mn)Se in the regime of electron hopping. *Journal of Applied Physics* **116**, 083710 (2014). https://doi.org/10.1063/1.4894236

139 Qingyu Xu, *et al.* Room temperature ferromagnetism in Nd- and Mn-codoped ZnO films. *Journal of Physics D: Applied Physics* **41**, 105012 (2008). https://doi.org/10.1088/0022-3727/41/10/105012

140 Wang, J. *et al.* Giant magnetoresistance in transition-metal-doped ZnO films. *Applied Physics Letters* **88** (2006). https://doi.org/10.1063/1.2210974

141 Xing, G. Z., Yi, J. B., Yan, F., Wu, T. & Li, S. Positive magnetoresistance in ferromagnetic Nd-doped In_2O_3 thin films grown by pulse laser deposition. *Applied Physics Letters* **104** (2014). https://doi.org/10.1063/1.4879463

142 Yang, Z. *et al.* Electron carrier concentration dependent magnetization and transport properties in ZnO:Co diluted magnetic semiconductor thin films. *Journal of Applied Physics* **104** (2008). https://doi.org/10.1063/1.3033402

143 Grünberg, P. A. Nobel Lecture: From spin waves to giant magnetoresistance and beyond. *Reviews of Modern Physics* **80**, 1531-1540 (2008). https://doi.org/10.1103/revmodphys.80.1531

144 Borders, W. A. *et al.* Integer factorization using stochastic magnetic tunnel junctions. *Nature* **573**, 390-393 (2019). https://doi.org/10.1038/s41586-019-1557-9

145 Camsari, K. Y., Sutton, B. M. & Datta, S. p-bits for probabilistic spin logic. *Applied Physics Reviews* **6**, 011305 (2019). https://doi.org/10.1063/1.5055860

146 Moodera, J. S., Kinder, L. R., Wong, T. M. & Meservey, R. Large Magnetoresistance at Room Temperature in Ferromagnetic Thin Film Tunnel Junctions. *Physical Review Letters* **74**, 3273-3276 (1995). https://doi.org/10.1103/physrevlett.74.3273

147 Binasch, G., Grünberg, P., Saurenbach, F. & Zinn, W. Enhanced magnetoresistance in layered magnetic structures with antiferromagnetic interlayer exchange. *Physical Review B* **39**, 4828-4830 (1989). https://doi.org/10.1103/physrevb.39.4828

148 Dieny, B. *et al.* Giant magnetoresistive in soft ferromagnetic multilayers. *Physical Review B* **43**, 1297-1300 (1991). https://doi.org/10.1103/physrevb.43.1297

149 Hicks, C. W., Barber, M. E., Edkins, S. D., Brodsky, D. O. & Mackenzie, A. P. Piezoelectric-based apparatus for strain tuning. *Review of Scientific Instruments* **85**, 065003 (2014). https://doi.org/10.1063/1.4881611

150 Chu, J.-H. *et al.* In-Plane Resistivity Anisotropy in an Underdoped Iron Arsenide Superconductor. *Science* **329**, 824-826 (2010). https://doi.org/doi:10.1126/science.1190482

151 Chu, J.-H., Kuo, H.-H., Analytis, J. G. & Fisher, I. R. Divergent Nematic Susceptibility in an Iron Arsenide Superconductor. *Science* **337**, 710-712 (2012). https://doi.org/doi:10.1126/science.1221713

152 Tschegg, E., Humer, K., Weber, H.W. Mechanical properties and fracture behaviour of polyimide (SINTIMID) at cryogenic temperatures. *Cryogenics* **31**, 878-883 (1991). https://doi.org/https://doi.org/10.1016/0011-2275(91)90021-N

153 Mohiuddin, T. M. G. *et al.* Uniaxial strain in graphene by Raman spectroscopy: G peak splitting, Grüneisen parameters, and sample orientation. *Physical Review B* **79** (2009). https://doi.org/10.1103/physrevb.79.205433

154 Rafael Roldán and Andrés Castellanos-Gomez and Emmanuele Cappelluti and Francisco, G. Strain engineering in semiconducting two-dimensional crystals. *Journal of Physics: Condensed Matter* **27**, 313201 (2015). https://doi.org/10.1088/0953-8984/27/31/313201

155 Song, C. *et al.* Largely Tunable Band Structures of Few-Layer InSe by Uniaxial Strain. *ACS Applied Materials & Interfaces* **10**, 3994-4000 (2018). https://doi.org/10.1021/acsami.7b17247

156 Li, Z. *et al.* Efficient strain modulation of 2D materials via polymer encapsulation. *Nature Communications* **11** (2020). https://doi.org/10.1038/s41467-020-15023-3

157 Niehues, I. *et al.* Strain Control of Exciton–Phonon Coupling in Atomically Thin Semiconductors. *Nano Letters* **18**, 1751-1757 (2018). https://doi.org/10.1021/acs.nanolett.7b04868

158 Conley, H. J. *et al.* Bandgap Engineering of Strained Monolayer and Bilayer MoS_2. *Nano Letters* **13**, 3626-3630 (2013). https://doi.org/10.1021/nl4014748

159 He, K., Poole, C., Mak, K. F. & Shan, J. Experimental Demonstration of Continuous Electronic Structure Tuning via Strain in Atomically Thin MoS_2. *Nano Letters* **13**, 2931-2936 (2013). https://doi.org/10.1021/nl4013166

160 Hopcroft, M. A., Nix, W. D. & Kenny, T. W. What is the Young's Modulus of Silicon? *Journal of Microelectromechanical Systems* **19**, 229-238 (2010). https://doi.org/10.1109/jmems.2009.2039697

161 Mohr, M., Papagelis, K., Maultzsch, J. & Thomsen, C. Two-dimensional electronic and vibrational band structure of uniaxially strained graphene from ab-initio calculations. *Physical Review B* **80** (2009). https://doi.org/10.1103/physrevb.80.205410

162 Ureña, F., Olsen, S. H. & Raskin, J.-P. Raman measurements of uniaxial strain in silicon nanostructures. *Journal of Applied Physics* **114**, 144507 (2013). https://doi.org/10.1063/1.4824291

163 Holler, B. A., Crowley, K., Berger, M. H. & Gao, X. P. A. 2D Semiconductor Transistors with Van der Waals Oxide MoO_3 as Integrated High - κ Gate Dielectric. *Advanced Electronic Materials* **6**, 2000635 (2020). https://doi.org/10.1002/aelm.202000635

164 Zhang, C. *et al.* Single-crystalline van der Waals layered dielectric with high dielectric constant. *Nature Materials* **22**, 832-837 (2023). https://doi.org/10.1038/s41563-023-01502-7

165 Dean, C. R. *et al.* Boron nitride substrates for high-quality graphene electronics. *Nature Nanotechnology* **5**, 722-726 (2010). https://doi.org/10.1038/nnano.2010.172

166 Rosenberger, M. R. *et al.* Nano-"Squeegee" for the Creation of Clean 2D Material Interfaces. *ACS Applied Materials & Interfaces* **10**, 10379-10387 (2018). https://doi.org/10.1021/acsami.8b01224

167 Paur, M. *et al.* Electroluminescence from multi-particle exciton complexes in transition metal dichalcogenide semiconductors. *Nature Communications* **10** (2019). https://doi.org/10.1038/s41467-019-09781-y

168 Cadiz, F. *et al.* Excitonic Linewidth Approaching the Homogeneous Limit in MoS_2. *Physical Review X* **7** (2017). https://doi.org/10.1103/physrevx.7.021026

169 Hwangbo, K. *et al.* Strain Tuning Three-state Potts Nematicity in a Correlated Antiferromagnet. (2023). *arXiv:2308.08734*

170 Zhu, C. R. *et al.* Strain tuning of optical emission energy and polarization in monolayer and bilayer MoS_2. *Physical Review B* **88** (2013). https://doi.org/10.1103/physrevb.88.121301

171 An, Z. *et al.* Strain control of exciton and trion spin-valley dynamics in monolayer transition metal dichalcogenides. *Physical Review B* **108** (2023). https://doi.org/10.1103/physrevb.108.l041404

172 Xi, X. *et al.* Strongly enhanced charge-density-wave order in monolayer $NbSe_2$. *Nature Nanotechnology* **10**, 765-769 (2015). https://doi.org/10.1038/nnano.2015.143

173 Guinea, F., Katsnelson, M. I. & Geim, A. K. Energy gaps and a zero-field quantum Hall effect in graphene by strain engineering. *Nature Physics* **6**, 30-33 (2010). https://doi.org/10.1038/nphys1420

174 Levy, N. *et al.* Strain-Induced Pseudo-Magnetic Fields Greater Than 300 Tesla in Graphene Nanobubbles. *Science* **329**, 544-547 (2010). https://doi.org/10.1126/science.1191700

175 Moon, H. *et al.* Dynamic Exciton Funneling by Local Strain Control in a Monolayer Semiconductor. *Nano Letters* **20**, 6791-6797 (2020). https://doi.org/10.1021/acs.nanolett.0c02757

176 Cenker, J. *et al.* Probing and controlling magnetism in 2D magnetic semiconductor CrSBr. *Proc. SPIE, Spintronics XV* **12205** (2022).

177 Rivera, P. *et al.* Intrinsic donor-bound excitons in ultraclean monolayer semiconductors. *Nature Communications* **12** (2021). https://doi.org/10.1038/s41467-021-21158-8

178 Li, Z., Wang, T., Miao, S., Lian, Z. & Shi, S.-F. Fine structures of valley-polarized excitonic states in monolayer transitional metal dichalcogenides. *Nanophotonics* **9**, 1811-1829 (2020). https://doi.org/10.1515/nanoph-2020-0054

179 Song, T. *et al.* Switching 2D magnetic states via pressure tuning of layer stacking. *Nature Materials* **18**, 1298-1302 (2019). https://doi.org/10.1038/s41563-019-0505-2

180 Li, T. *et al.* Pressure-controlled interlayer magnetism in atomically thin CrI_3. *Nature Materials* **18**, 1303-1308 (2019). https://doi.org/10.1038/s41563-019-0506-1

181 Bhatti, S. *et al.* Spintronics based random access memory: a review. *Materials Today* **20**, 530-548 (2017). https://doi.org/https://doi.org/10.1016/j.mattod.2017.07.007

182 Cenker, J. *et al.* Strain-programmable van der Waals magnetic tunnel junctions. (2023). *arxiv:2301.03759*

183 Wang, Z. *et al.* Magnetization dependent tunneling conductance of ferromagnetic barriers. *Nature Communications* **12** (2021). https://doi.org/10.1038/s41467-021-26973-7

184 Jiang, S., Shan, J. & Mak, K. F. Electric-field switching of two-dimensional van der Waals magnets. *Nature Materials* **17**, 406-410 (2018). https://doi.org/10.1038/s41563-018-0040-6

185 Song, T. *et al.* Voltage Control of a van der Waals Spin-Filter Magnetic Tunnel Junction. *Nano Letters* **19**, 915-920 (2019). https://doi.org/10.1021/acs.nanolett.8b04160

186 Wu, J. M. *et al.* Ultrahigh Sensitive Piezotronic Strain Sensors Based on a $ZnSnO_3$ Nanowire/Microwire. *ACS Nano* **6**, 4369-4374 (2012). https://doi.org/10.1021/nn3010558

187 Yan, W. *et al.* Giant gauge factor of Van der Waals material based strain sensors. *Nature Communications* **12** (2021). https://doi.org/10.1038/s41467-021-22316-8

188 Safranski, C. *et al.* Demonstration of Nanosecond Operation in Stochastic Magnetic Tunnel Junctions. *Nano Letters* **21**, 2040-2045 (2021). https://doi.org/10.1021/acs.nanolett.0c04652

189 Pervaiz, A. Z., Datta, S. & Camsari, K. Y. in *2019 IEEE BiCMOS and Compound semiconductor Integrated Circuits and Technology Symposium (BCICTS).* (IEEE).

190 Ang, S. & Chuchill, S. *NIST Test Suite*, <https://github.com/stevenang/randomness_testsuite> (2017).

191 Ponomarenko, L. A. *et al.* Chaotic Dirac Billiard in Graphene Quantum Dots. *Science* **320**, 356-358 (2008). https://doi.org/doi:10.1126/science.1154663

192 Giesbers, A. J. M. *et al.* Nanolithography and manipulation of graphene using an atomic force microscope. *Solid State Communications* **147**, 366-369 (2008). https://doi.org/10.1016/j.ssc.2008.06.027

193 Mondal, A. & Srivastava, A. In Situ Stochastic Training of MTJ Crossbars With Machine Learning Algorithms. *ACM Journal on Emerging Technologies in Computing Systems* **15**, 1-29 (2019). https://doi.org/10.1145/3309880

194 Nogués, J., Schuller, I. K. Exchange bias. *Journal of Magnetism and Magnetic Materials* **192**, 203-232 (1999). https://doi.org/https://doi.org/10.1016/S0304-8853(98)00266-2

195 Lavrijsen, R. *et al.* Magnetic ratchet for three-dimensional spintronic memory and logic. *Nature* **493**, 647-650 (2013). https://doi.org/10.1038/nature11733

196 Gingrich, E. C. *et al.* Controllable 0–π Josephson junctions containing a ferromagnetic spin valve. *Nature Physics* **12**, 564-567 (2016). https://doi.org/10.1038/nphys3681

197 Ai, L. *et al.* Van der Waals ferromagnetic Josephson junctions. *Nature Communications* **12** (2021). https://doi.org/10.1038/s41467-021-26946-w

198 Idzuchi, H. *et al.* Unconventional supercurrent phase in Ising superconductor Josephson junction with atomically thin magnetic insulator. *Nature Communications* **12** (2021). https://doi.org/10.1038/s41467-021-25608-1

199 Kang, K. *et al.* van der Waals π Josephson Junctions. *Nano Letters* (2022). https://doi.org/10.1021/acs.nanolett.2c01640

200 Narita, H. *et al.* Field-free superconducting diode effect in noncentrosymmetric superconductor/ferromagnet multilayers. *Nature Nanotechnology* (2022). https://doi.org/10.1038/s41565-022-01159-4

201 Ando, F. *et al.* Observation of superconducting diode effect. *Nature* **584**, 373-376 (2020). https://doi.org/10.1038/s41586-020-2590-4